POLITECNICO
MILANO 1863

SCUOLA DI INGEGNERIA INDUSTRIALE
E DELL'INFORMAZIONE

Helicopter sensorized inceptors for pilot workload evaluation

Tesi di Laurea Magistrale in
Aeronautical Engineering - Ingegneria Aeronautica

Author: **Davide Pio Loco Zanet**

Student ID: 990087
Advisor: Prof. Andrea Zanoni
Co-advisors: Davide Marchesoli, Pietro Ballarin
Academic Year: 2022-23

Acknowledgements

Vorrei innanzitutto ringraziare il mio supervisore, prof. Andrea Zanoni, per avermi dato l'opportunità di lavorare su questo progetto di tesi sperimentale.
Ringrazio molto Davide Marchesoli e Pietro Ballarin per la loro disponibilità e il loro prezioso supporto durante tutte le fasi dello sviluppo di questa tesi.

Vorrei ringraziare i miei genitori, Catia e Sergio, per avermi sempre incoraggiato e reso possibile intraprendere e completare il mio percorso di studi senza dovermi preoccupare di altro.
Un ringraziamento speciale a mia sorella Elisa, che tra poco diventerà mamma, per il suo amore incondizionato che ha sempre avuto per me.
Desidero ringraziare i nonni Maria, Massimo, Marisa e Gino per la loro costante presenza e per la stima che mostrano sempre nei miei confronti.
Grazie anche agli zii Sandra, Gianni, Daniela, Sergio e ai cugini Anna e Federico, che fanno sempre il tifo per me.

Infine, un ringraziamento a tutti gli amici, dell'università e non, che mi hanno supportato e aiutato a trovare il giusto equilibrio tra studio e svago.

Grazie.

Abstract

Enabling the assessment of pilot workload during flight could have very important consequences in enhancing flight safety, especially in rotorcraft, providing the tools for preventive actions against loss of situational awareness and indicating the possible insurgence of adverse coupling interactions between the pilot and the vehicle. The realization of purposely-designed helicopter control inceptors is presented in this thesis work. They are equipped with optical sensors which permit to have an objective measurement of the loads introduced by the pilot in the control inceptors and of the pressure applied by the hand. As opposed to classical subjective pilot workload assessment methods, the sensors presented allow to have a measure independent from the pilot subjective feedback. Since the measurement devices included in the inceptors do not modify the ergonomics of the input devices, they could be used in a real flight environment. To make the sensors on the cyclic stick usable in the motion platform available at Politecnico di Milano Department of Aerospace Science and Technology (DAER), a calibration procedure is carried out. The sensor of the collective grip is tested on the motion platform during missions of different difficulty, obtaining the corresponding level of the pilot workload.

Keywords: Rotorcraft-Pilot Coupling, Helicopter controls, Optical Sensors, Workload

Abstract in lingua italiana

Permettere la valutazione del carico di lavoro del pilota durante il volo potrebbe avere conseguenze molto importanti nel migliorare la sicurezza del volo, in particolare negli elicotteri, fornendo gli strumenti per mettere in atto azioni preventive contro la perdita della *situational awareness* e indicando la possibile insorgenza di un accoppiamento avverso tra pilota e velivolo. In questo lavoro di tesi viene presentata la realizzazione di comandi di elicottero appositamente progettati. Essi sono dotati di sensori ottici che permettono di avere una misurazione oggettiva dei carichi introdotti dal pilota nei comandi e della pressione esercitata dalla mano. In opposizione ai metodi classici soggettivi per la valutazione del carico di lavoro del pilota, i sensori presentati permettono di avere una misura indipendente dal giudizio soggettivo del pilota. Dato che i dispositivi di misurazione contenuti nei comandi non modificano l'ergonomia degli stessi, essi potrebbero essere utilizzati in un contesto di volo reale. Una procedura di calibrazione è svolta per rendere i sensori della leva del ciclico utilizzabili nella piattaforma mobile disponibile al Dipartimento di Scienze e Tecnologie Aerospaziali del Politecnico di Milano (DAER). Il sensore nell'impugnatura del collettivo è testato nella piattaforma durante missioni di diversa difficoltà, ottenendo il corrispondente livello del carico di lavoro del pilota.

Parole chiave: Interazione Pilota-Elicottero, Controlli dell'elicottero, Sensori ottici, Carico di lavoro

Contents

1 | Introduction

Present-day aircraft and rotorcraft are the result of the ever increasing needs of operator requirements. Compared to their forerunners, they are faster and more capable but, as a consequence, they are more complex. The rise in complexity can contribute, among the others, to increase *pilot workload*. In particular, helicopters are inherently more complex to operate compared to fixed-wing aircraft due to their unique flight characteristics and operational requirements. The complexity of helicopters can lead to a higher workload for pilots, especially during demanding flight conditions or when operating advanced helicopter systems. Some factors related to helicopter complexity that can affect pilot workload are:

- flight controls: helicopters have a complex set of flight controls, including collective inceptor, cyclic inceptor, and anti-torque pedals. Manipulating these controls simultaneously requires skill and coordination from the pilot, which needs to constantly adjust and maintain control inputs throughout the flight, particularly during maneuvers such as hovering, autorotation, or low-speed flight; moreover, rotorcraft control inputs are transmitted through the swashplate to the blade pitch, resulting in flap response with nearly 90° phase delay (1/4 of the rotor revolution period);
- control couplings: rotorcraft are characterized by many control couplings. For example, by pulling the collective command the pilot generates an increase of both thrust and the torque, so it is necessary to compensate using the pedals;
- intrinsic instability: in key flight conditions, rotorcraft are inherently dynamically unstable;
- systems management: helicopters have various systems that require monitoring and management, such as engine controls, fuel systems, hydraulic systems, and rotor systems;
- navigation and situational awareness: helicopters often operate in diverse and challenging environments, such as urban areas, mountainous terrain, or adverse weather conditions. Navigating through these environments while maintaining situational

awareness demands constant attention and mental processing. Pilots must interpret navigation aids, track obstacles, assess weather conditions, and make real-time decisions;

- avionics and automation: modern helicopters are equipped with advanced avionics systems and automation features designed to assist pilots in flight operations. While these technologies can reduce workload in certain situations, they also require pilots to understand and effectively use the systems;
- emergency procedures: helicopters are capable of performing emergency procedures, such as autorotation landings or engine failure recoveries. These procedures require pilots to quickly assess the situation, execute appropriate actions, and maintain control of the aircraft;
- vibrations: rotorcraft generate vibrations in all major axes; vibrations are mainly due to rotating mechanical components, such as the main and tail rotors, as well as the drive trains and the mechanical transmissions.

Pilot workload can be a contributing factor in helicopter accidents: when a pilot is overwhelmed with excessive workload, the ability to effectively manage the aircraft and respond to changing conditions may be compromised. This can increase the risk of errors, loss of situational awareness, and ultimately lead to accidents. Last year's EASA Annual Safety Review (Ref. [1]) indeed shows that Human factors (HF) or Human performance (HP) issues can be identified in over a quarter of accidents and serious incident reports involving helicopters, as can be seen in Figure 1.1. It reports the figures for years 2019 to 2021 about the human factors and human performance accidents and serious incidents involving all helicopter operations. Excluding 2021, for which data were not available at the time (since they are the result of detailed investigations) the figures confirm the above.

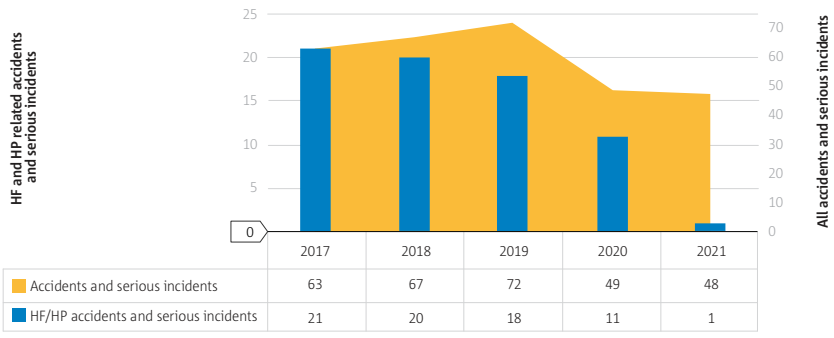

Figure 1.1: Human factors and human performance accidents and serious incidents involving all helicopter operations (Ref. [1])

It is commonly agreed that the degree of pilot workload can also potentially contribute to the occurrence of Rotorcraft-Pilot-Coupling (RPC). Generally, RPCs are adverse, unwanted phenomena originating from anomalous and undesirable couplings between the pilot and the rotorcraft (Ref. [2]). These unwanted couplings could cause either oscillatory or non-oscillatory instabilities that may be associated, among the others, to a degradation of the vehicle *handling qualities* and, in turn, of the occupants' comfort. Prior to 1995, RPC events were better known in the aircraft and rotorcraft community as Pilot-Induced Oscillations (PIO) and Pilot-Assisted Oscillations (PAO):

- PIO occur when the pilot intentionally moves the controls causing divergent vehicle oscillations, although the latter are not intentionally induced; since the active involvement of the pilot in the control loop is pre-requisite, the oscillations will cease when the pilot releases the controls, stops providing control inputs or changes the control strategy;
- PAO are the result of involuntary control inputs by the pilot in the loop that may destabilise the aircraft due to the pilot's biodynamic response to vibrations.

Emphasis ("blame") was erroneously placed on pilot's role, whereas the root cause is a limitation of - or deficiency in - the design of system/task. Today it is generally recognized that a specific unfavorable incident is not always nor fully the fault of the pilot, but it is frequently ultimately linked to some characteristics of the aircraft or of its control system (Ref. [2]).

As reported in Ref. [3], basing on past flight experiences, it is possible to classify the different types of RPC into two categories: Rigid Body RPC and Aeroelastic RPC. As can be seen in Table 1.1, the distinction is carried out on the basis of the frequency range characterizing the phenomena, respectively below $1Hz$ and between $2Hz$ and $8Hz$. Rigid Body RPC phenomena are dominated by the helicopter low frequency dynamics, i.e., the field of flight mechanics, by the flight control system and by an "active" pilot concentrating on performing his mission task by actively manipulating the helicopter controls. Aeroelastic RPC phenomena are instead characterized by higher helicopter frequency dynamics, i.e., the inclusion of elastic airframe and main rotor blade modes, by a "passive" pilot subjected to vibrations which are too high in frequency to adequately be reacted by human beings and by the cockpit controls layout affecting the pilots inertial response on the helicopter control elements.

	Rigid Body RPC	Aeroelastic RPC
Frequency Range	$f \leq 1Hz$	$2Hz \leq f \leq 8Hz$
Pilot Behaviour	Active	Passive
Helicopter Dynamics	Flight mechanics	Structural dynamics
Critical Components	Flight control system	Airframe modes

Table 1.1: RPC types classification

In all the cases, prediction of RPC phenomena is challenging, since they result from an interaction of three main actors, that are, the *pilot*, the *vehicle* and a *trigger* (i.e., some unpredictable condition that gives rise to adverse coupling).
In this frame, the study of human-rotorcraft interaction has placed a strong emphasis on the development of pilots' *workload* assessment tools and procedures. As a matter of fact, in many accidents and incidents occurring during flight, workload plays a very important role as a triggering factor (i.e., as one of the three elements that generate an RPC) for subsequent loss of situational awareness (Ref. [4]), that arises from the extreme conditions of workload levels being *too low* or *too high*. Considering that a change in workload entails a change in the pilot control techniques and the associated neuromuscular activity, it is well recognized that a correlation exists between the task difficulty (and hence the pilot workload) and the insurgence of unfavorable RPCs (Ref. [5], Ref. [6]). The change of the pilot neuromuscular activity due to the a change in workload directly reflects on a change of the pilot control actions on the inceptors, which can result in an adverse RPC phenomenon.

1.1. Helicopter inceptors typical layout

At this point, it is worth explaining the typical layout of helicopter flight controls, reported in Figure 1.2, that is made by three inceptor systems:

1. the *collective inceptor*, located on the left side of the pilot's seat and operated with the left hand, is able to rotate about an axis oriented right-to-left: if rotated upward (downward) there is an equal and simultaneous increase (decrease) in pitch angle of all main rotor blades, i.e., in the main rotor thrust magnitude;

2. the *cyclic inceptor*, usually projected upward from the cockpit floor between the pilot's legs and operated with the right hand, is able to rotate about the longitudinal and the lateral axes: a forward (lateral) rotation of the cyclic stick generates a cyclic

pitch variation able to incline the direction of the main rotor thrust, inclining it forward (laterally). This allows the pilot to fly the helicopter in any direction of travel: forward, rearward, left and right.

3. the *pedals*, located on the cabin floor by the pilot's feet, are able to jointly rotate about a common vertical axis: a leftward rotation of the pedals, created by pushing away from the pilot the pedal on the left (the pedal on the right will correspondingly be moved toward the pilot) generates a variation of the tail rotor thrust as to induce a yaw acceleration of the aircraft in the direction of moving the nose to the left.

Globally, it is possible to control the main rotor thrust magnitude and direction and the tail rotor thrust magnitude.

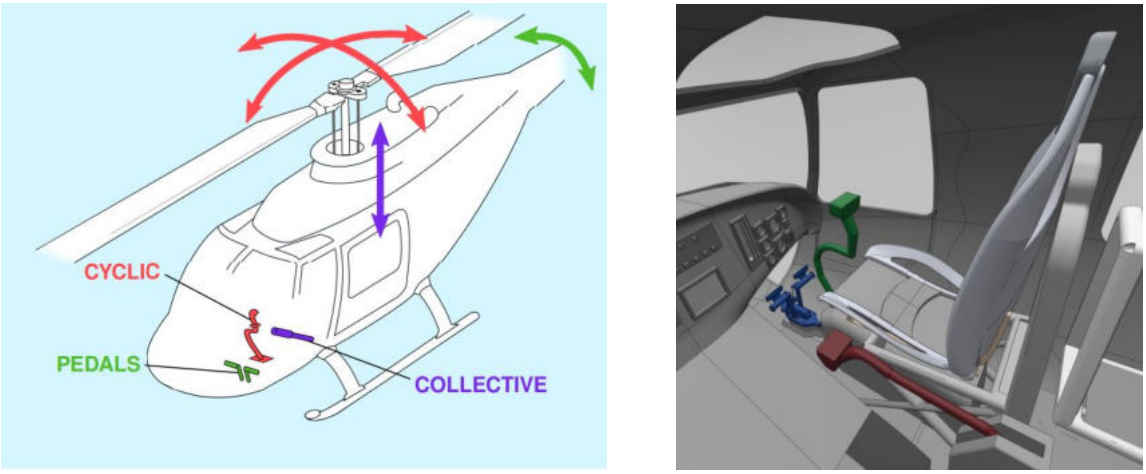

Figure 1.2: Typical helicopter inceptors layout (Ref. [7])

Collective and cyclic inceptors are made of two parts (Figure 1.3):

1. the *grip*, that is the upper part, hold by the pilot hand and containing all the keys, buttons and switches through which the pilot controls the helicopter;

2. the *stick*, that is the linkage between the grip and the hinge (usually referred to as *elbow*) which permits the rotation of the control.

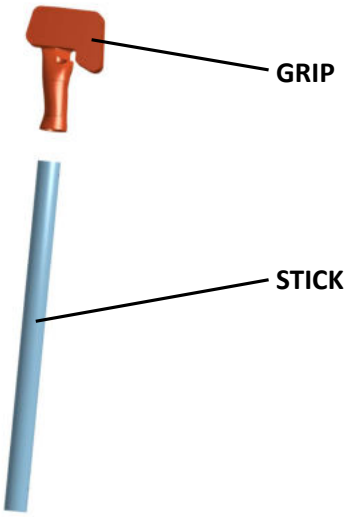

Figure 1.3: Inceptor structure: grip and stick

The present work is focused on the design and instrumentation of an helicopter collective grip and cyclic stick.

Two typical inceptors RPC-related issues are the *collective bounce* and the *lateral stability* problem.

Collective bounce

A PAO phenomenon specific of helicopters is the so-called "collective bounce" (also known as "vertical bounce") , an RPC caused by vertical vibrations of the cockpit. It is the result of a control loop, along the vertical axis, closed by the pilot:

- the thrust of the rotor directly depends on the collective pitch, which is controlled through the collective inceptor;
- the motion of the hand, when moving the collective inceptor, is notionally vertical;
- an oscillatory perturbation of the thrust produces vertical vibrations of the airframe, including the cockpit, which excites the pilot through the seat and the floor;
- as a consequence of the cockpit and control inceptors layout, the vibrations induce a collective control input as a result of the biodynamics of the pilot's left arm, which holds the collective inceptor and the (involuntary) motion of the inceptor excites the thrust perturbation, closing the involuntary feedback loop (Ref. [8]).

Lateral stability

Although the collective bounce is the most important PAO, similar issues were also seen on the cyclic, particularly with reference to the lateral stability. As a case in point is the one of Ref. [9], in which real-time flight simulation experiments have been used to study a technique to predict the adverse aeroservoelastic rotorcraft–pilot couplings between a rotorcraft's roll motion and the resultant involuntary pilot lateral cyclic motion. The results show that the cause that triggered the PAO was an aeromechanical instability (similar to air resonance) created by the lightly damped main rotor regressive lead–lag mode at 2.28 Hz, coupled with the pilot biodynamics/lateral stick dynamics.
PIO instabilities are also present, especially due to time delays. They are introduced in the control system of actual aircraft by fly-by-wire systems, specifically by the digital acquisition and filtering of control device motion and by signal processing before feeding inputs to the actuators. Delays of the order of 80 ms are plausible, but higher values have been reported, especially in early experimental aircraft (Ref. [7]).

1.2. Outline

1.2.1. Thesis objective

In this work, it is presented the design, the realization and the testing of *light-instrumented* helicopter collective and cyclic inceptors for the gather of real-time information about the pilot action. The word *light* has to be intended in both its English acceptations, being the measurement systems:

- based on an optical principle, i.e., on the light properties;
- non-intrusive, i.e., they neither interfere with the piloting experience nor alter the ergonomics and the perceptible characteristics of the input devices.

The sensorization of the control inceptors concerns the collective inceptor grip, for which a layout re-engineering of an already developed optical sensor (Ref. [7], Ref. [10]) is performed, and the cyclic inceptor stick. In particular, the collective inceptor grip is instrumented with a sensor able to capture the pressure introduced by the pilot hand. Some parts of the grip, that is 3D printed, slide with respect to the rest of the grip itself so that, when pressure is applied, they are free to sink by a small amount—almost imperceptible to the pilot—but significant enough to result in a pressure measurement. This sensor could help in the monitoring of the pilot workload, since higher workload levels are likely associated to a higher pressure exerted on the grip (Ref. [11]). About the cyclic inceptor

stick, it is made of carbon fiber-reinforced composite material and is equipped with Fiber Bragg Grating (FBG) sensors able to measure the deformation induced by the pilot control actions. The sensors working principle relies on the measure of the frequency shift of the light passing through the optical fiber in which they are embedded as consequence of the external phenomena to which the latter is subjected. This is possible by inscribing an invisible permanent periodic refractive index change in the core of the optical fiber, which reflects a specific wavelength and let the others passing through. The measure of the loads applied to the stick has a paramount importance in the prevention and study of RPC phenomena, enabling the computation of one of the fundamental indices of the pilot-vehicle interaction, that is the Biodynamic Feedthrough (BDFT).

1.2.2. Thesis structure

The thesis work is organized as follows: in Chapter 2 a review of the pilot workload assessing methods and of the state of the art is reported. Chapter 3 is dedicated to the collective grip sensor design and realization, while Chapter 4 is about its experimental testing. Chapter 5 deals with the cyclic inceptor design and realization, while Chapter 6 deals with the stick sensors calibration process for the load identification, that is performed by doing experimental tests and by the use of a Finite Element (FE) model. In Chapter 7 are reported the conclusions of the present work and its future developments.

2 | Pilot workload

2.1. Definition

Flying an aircraft imposes a load on the pilot who has to expend an amount of physical and mental effort to accomplish the task. This ostensibly easy assertion conceals the difficulty of defining pilot workload and a review of the literature reveals the wide range of interpretation and the vagueness which exists (Ref. [12]). Although there is not a single definition that can be accepted, several authors have pointed to *effort* as the central idea in their conception of workload. In their handling qualities rating scale, Cooper and Harper (Ref. [13]) ask "Is adequate performance attainable with a tolerable pilot workload?" and they defined pilot workload as "the integrated physical and mental effort required to perform a specified piloting task". The idea of workload as *effort* is one with which also many pilots would agree, since it accounts for the individual ways in which pilots respond to the demands of the flight task by encompassing such variables as natural ability, training, experience, age and fitness (Ref. [12]). Nonetheless, there are other crucial elements of the flight task which can be deemed as fundamental in defining concepts of workload, providing a fertile soil for controversy. Despite this, it is generally acknowledged that:

- workload depends on the level of the "pilot compensation" needed;
- a key aspect is the time-limited capability of the human operator;
- there are two main areas for consideration, that are task-related and pilot-related aspects;
- it is possible to divide workload into physical and non-physical (or mental) components; on that, it is agreed that the increasing use of advanced autopilots and flight management computers has, especially in civil transport aircraft, caused a substantial decrease in the physical content of the total workload with a consequent relative increase in the cognitive or mental content;
- workload duration is a determining factor;

- stress plays an important role in determining pilot workload.

About the last point, even though stress is often vaguely defined, it refers to the physiological and psychological responses experienced by pilots when they perceive demands, pressures, or challenges that exceed their ability to cope effectively. It is a natural and often unavoidable reaction to various factors encountered during aviation operations, including, other than high workload, time pressure, critical decision-making, challenging weather conditions, complex aircraft systems, emergencies and other situational demands.

2.2. Techniques for workload assessment

Over the past fifty years, considerable research efforts have been devoted on finding accurate methods for monitoring pilot workload, particularly those that may be used during flight (Ref. [14]). Numerous experiments have examined different strategies; particularly, it appears that the increased accessibility of General Aviation Trainers (GAT) in research labs has significantly boosted the number of experiments involving pilot workload. Unfortunately, of the many different techniques that have been developed, most are suitable only for use in the carefully controlled conditions of the laboratory or flight simulator (Ref. [14]).

Numerous authors have put forth an array of criteria for workload assessment methodologies, which include sensitivity, diagnosticity, selectively, intrusiveness, concordance, reliability, operator acceptance, and convenience. Not to forget, when assessing workload in aircraft, the techniques must be compatible with flight safety. Whilst it could be fair to try to meet many of these requirements in laboratory investigations, it would be impossible to apply them too strictly in the real world. The different methods for assessing pilot workload can be broadly divided into three groups: *objective*, *subjective* and *physiological* (Ref. [14]). The bibliographic reference for Subsections 2.2.1, 2.2.2, 2.2.3, 2.2.4 is Ref. [14].

2.2.1. Objective Techniques

These can be further divided into *performance measures* and *analytic techniques*.

Performance Measures

It is unquestionable that a relationship between workload and performance exists, even though it may not be a simple one, but at the same time there is little doubt in saying that performance is not the only criterion: the expense of the pilot in terms of effort and

the likelihood of an overloaded pilot are of utmost relevance.

For instance, a pilot may exert more effort and increase his workload as the demands on him increase to maintain performance. Conversely, as appears to happen more and more often today, the demands on the pilot may be reduced and performance may suffer as the perceived workload becomes less due to complacency.

This precludes the use of performance alone as the only metric for workload assessment. Nonetheless, it is important, when assessing workload, to define performance criteria and then to monitor the result. Instrumented aircraft and external measuring devices, such as kinetheodolites sited on airfields to monitor approaches and landings, are ideal. This is rarely possible but the use of video cameras to record crew activity and cockpit instrumentation is an alternative way of monitoring performance.

Analytic Techniques

Many engineers and designers view workload in terms of the demands of the task. This is an interpretation of workload that encourages the use of analytic techniques based on some form of time and motion study. Timeline analysis carried out in mockups, in flight simulators or in real aircraft is used to build up a data store of physical activity associated with specific scenarios. These data can be used to build models, calculate workload indices and forecast the workload for a certain task or aircraft.

2.2.2. Subjective Techniques

Without a question, the most popular and likely most reliable method presently available for estimating workload in flight is subjective reporting, in some form, by experienced test pilots (Hart in Ref. [15] said "Workload is a subjective experience"). There are many methods for gathering subjective evaluations, from basic unstructured interviews and surveys for use after flight to complex rating scales for use during flight. Post-flight approaches usually have the upside of being simple and can provide valuable information on workload but they heavily rely on a pilot's ability to recall events and impressions that may have occurred some time in the past. Despite that, both organized and unstructured interviews and questionnaires can be employed effectively to supplement in-flight assessments.

2.2.3. Physiological Techniques

The technique of measuring physiological variables to assess workload has been used for many years in a variety of situations. Despite the fact that flying a modern airplane requires little physical effort and little control force during routine manoeuvres, a large amount of neuromuscular involvement occurs when a pilot is manually flying an aircraft where precise and frequent control inputs may be needed, such as on landing or in the positioning of slung loads. Changes in a physiological variable like heart rate can be used to detect this involvement.

2.2.4. Combined Techniques

There is currently compelling evidence that the best accurate method for determining workload in flight is a mix of many strategies. It appears that a subjective technique backed by a physiological measurement is a popular combination. A good correlation between heart rate and respiratory frequency, subjective ratings, overall performance, control activity, and model results has been reported by van de Graaff (Ref. [16]).

2.3. State of the art assessing methods

Currently, the primary method of workload evaluation is through a *subjective* assessment that the pilot performs as close as possible to the conclusion of a mission. The assessment is very often supported by purposely-developed charts, e.g., the Bedford rating scale or the more specialized DIPES scale, that are reported respectively in Figure 2.1 and in Figure 2.2. In the first case, the assessment is based on the use of a uni-dimensional rating scale designed to identify operator's spare mental capacity while completing a task non-directly related to piloting. The operator is guided through a ten-point rating scale with a descriptor of the corresponding level of workload in a hierarchical decision tree (nominal tasks should have ratings of 3 or less and off-nominal tasks of 6 or less) (Ref. [17]). The DIPES scale consists instead on the evaluation of the compensation effort required by the pilot. A rating in the range 1-3 is assigned to tasks that present little difficulty. More difficult tasks that reduced the pilot's spare capacity to perform ancillary tasks are awarded increasingly higher ratings. At conditions for which the pilot is not able to apply sufficient effort and has to abandon the task, a rating of 10 is awarded (Ref. [18]).

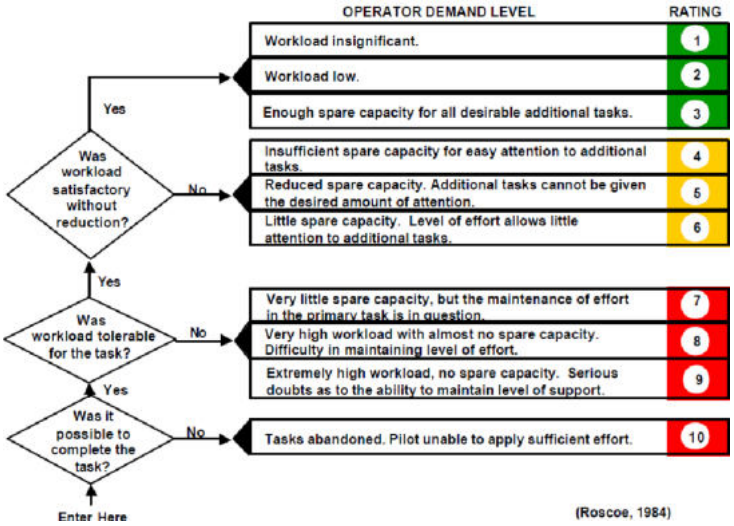

Figure 2.1: Bedford rating scale (Ref. [17])

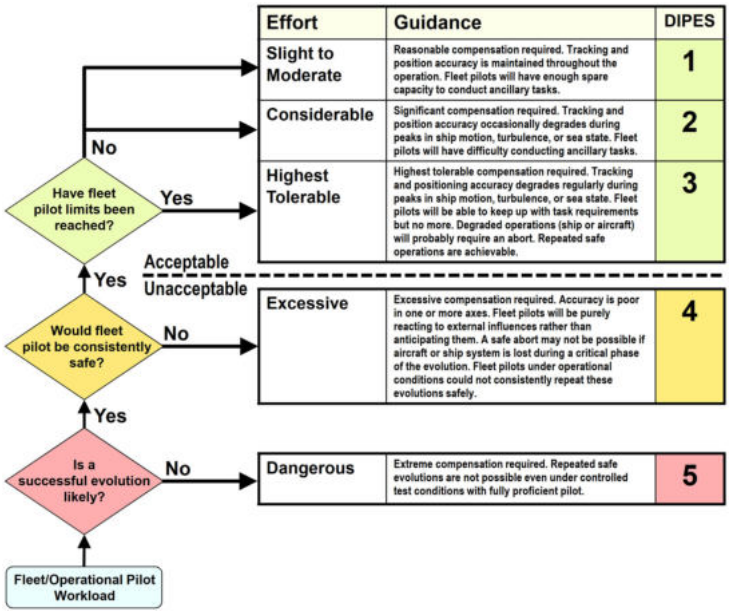

Figure 2.2: DIPES rating scale (Ref. [18])

To the two rating scales aforementioned, it is worth adding a third one, that is the NASA Task Load Index (NASA-TLX), of which a paper-and-pencil version is reported in Figure 2.3. It is a procedure for collecting *subjective* workload ratings that was developed by the Human Performance Group at NASA's Ames Research Center. In particular, it is a multi-dimensional rating procedure that provides an overall workload score based on a weighted average of ratings on six subscales (Ref. [19]):

1. Mental Demands: how mentally demanding was the task? How much mental effort

was required?

2. Physical Demands: how physically demanding was the task? How much physical effort was required?
3. Temporal Demands: how much time pressure did you feel during the task? How much work had to be done in a limited amount of time?
4. Own Performance: how successful do you think you were in accomplishing the goals of the task?
5. Effort: how hard did you have to work to accomplish the task? How much effort did you exert?
6. Frustration: how irritated, stressed, and annoyed were you during the task? How much negative emotion did you experience?

It has been used in a variety of domains, including aviation, healthcare and other complex socio-technical domains. There is a description for each of these subscales that the subject should read before rating. They are rated for each task within a 100-points range with 5-point steps. These ratings are then combined to the task load index. Providing descriptions for each measurement can be found to help participants answer accurately.

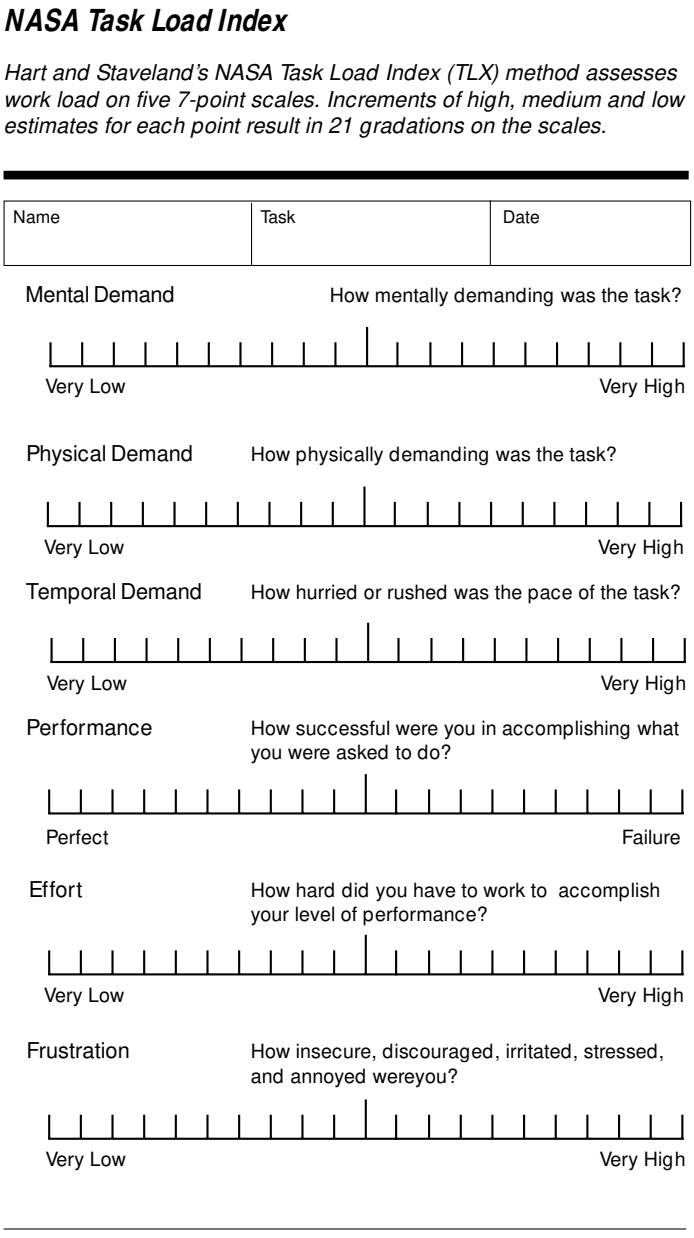

Figure 2.3: Paper-and-pencil version of the NASA-TLX rating scale (Ref. [19])

A second part of the NASA-TLX rating procedure is reported in Figure 2.4 and it includes an individual weighting of these subscales. It enables the subjects compare them pairwise based on their perceived importance. This requires the user to choose which measurement is more relevant to workload. The number of times each is chosen is the weighted score. This is multiplied by the scale score for each dimension and then divided by 15 to get a workload score from 0 to 100, the overall task load index.

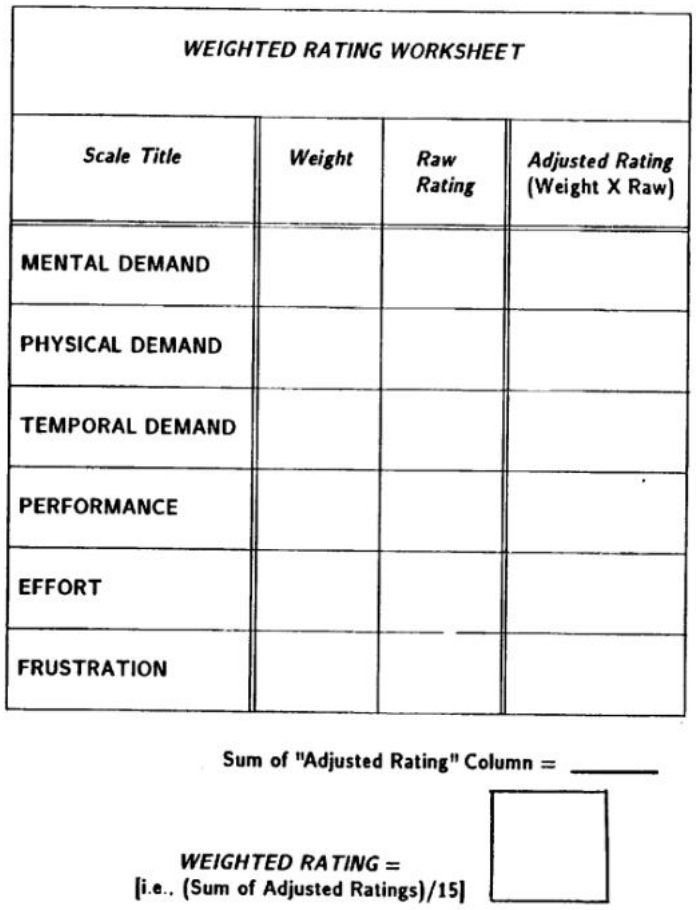

WEIGHTED RATING WORKSHEET

Scale Title	Weight	Raw Rating	Adjusted Rating (Weight X Raw)
MENTAL DEMAND			
PHYSICAL DEMAND			
TEMPORAL DEMAND			
PERFORMANCE			
EFFORT			
FRUSTRATION			

Sum of "Adjusted Rating" Column = _____

WEIGHTED RATING = [i.e., (Sum of Adjusted Ratings)/15]

Figure 2.4: NASA-TLX subscales weighting table (Ref. [19])

In virtually all the subjective methods, the pilot assessment should be related to a single Mission Task Element (MTE), in order for it to be related to a mission segment that will present a uniform level of requirements to the piloting task (Ref. [4]). The critic point of these evaluation methods is that they are subjective: they have all the limits related to the human activity and pilots must be trained to answer to the questionnaires because there are a lot of psychological implications: for example, if the MTE is long, then the pilot tends to remember only the bad aspects or the good ones or the most recent ones.

Two strategies are generally employed, instead, for *instantaneous* pilot workload assessment:

1. analysis of pilot activity, generally performed in the time domain, carried out on available data streams like control inputs. An example is the *phase aggression criterion* of M. Jones et al. (Ref. [20]), a method focused on considering the phase difference between pilot input displacement and vehicle rate;

2. analysis of psycho-physiological indicators, via the introduction of specialized mea-

surement devices (e.g., heart rate monitoring, surface electrical capacitance, etc.), as shown in Ref. [21]. An example of a subject with motion capture markers and Electromyography (EMG) electrodes can be seen in Figure 2.5.

Figure 2.5: Subject with specialized measurement devices (taken from Ref. [21])

Another example is the equipment set up by B. Johannes et al. (Ref [22]) (Figure 2.6), through which electrocardiogram, peripheral skin resistance, finger skin temperature, rate/depth of respiration and pulse transition time are continuously measured.

Figure 2.6: Pilot with the sensors equipment taken from Ref [22]

The findings of the study provided insights into the pilots' psychophysiological responses during challenging flight maneuvers. Significant increases in heart rate, blood pressure,

and subjective stress ratings were observed during both simulated and real flight tasks, indicating heightened stress levels. Additionally, cortisol levels, which are indicators of stress, were found to be elevated in response to the demanding flight maneuvers. The study emphasized the importance of considering psychophysiological responses as indicators of pilot workload and stress in aviation settings. Understanding these responses can contribute to the development of strategies and interventions to manage pilot stress and optimize performance.

In Ref. [23], Y. Sahar et al. investigate a stress-adaptive training approach based on the measurement of the grip force. The research work aimed to develop a training method that adapts to an individual's stress levels to enhance psychomotor skills. Based on the stress levels measured, the training system adapted the difficulty and complexity of the tasks to match the participants' stress responses. The results of the study indicated that the stress-adaptive training approach, which adjusted the difficulty of the tasks based on the grip force measurements, led to improved performance and learning outcomes compared to traditional fixed-difficulty training methods. The participants showed enhanced psychomotor skills and adaptability when they received training tailored to their stress levels.

2.4. About the tools presented in this work

The workload assessment methods based on the use of the tools proposed in this study fall under the category of combined methods, since the pressure applied by the pilot hand can be considered a physiological indicator of the pilot workload level and the measure of the stick's deformation provides an objective indication of forces applied by the pilot. The sensorized grip and stick presented in this work have a number of potential benefits, including:

- they do not alter the design of the control inceptors;
- they do not require complex equipment for the data acquisition;
- they are stand-alone, i.e., they do not depend on the presence of other systems;
- it is possible to choose whether to perform a real-time analysis of the data or to download them after the flight;
- the extreme low cost of the pressure sensor components allow it to be applied and adapted easily to a large quantity of different inceptors in a large variety of vehicles;
- the pilot is not required to do any special activity or provide ad hoc feedback,

answers to questionnaires or so.

Among the others, they can be used to:

- identify unwanted inputs in terms of force and pressure applied on the handle and their variation in time: the possibility to detect quick changes or spikes in the applied force could be used to detect RPC phenomena that are not visible just by looking at the stick motion;
- train pilots to deal with RPCs by inducing them and monitoring the pilot response, giving feedback about their behaviour and making them used to such phenomena;
- have a redundancy in the control law: the obtained input from the sensors on the grip and on the stick could be compared to the one coming from the stick motion to enhance the control law and reduce uncertainties; in case of fly-by-wire helicopter, this is particularly important in case of failure of the fly-by-wire system.

Furthermore, a review of the available literature reveals that the FBG sensors have never been embedded in a control stick. All of that is not to say that the tools proposed could entirely replace the assessing methods presented above, but rather they could play an important role for example in a *combined technique*, without leading to an increase of the complexity of the correlated activity, both from the piloting and the setup point of view.

3 | Collective inceptor grip

3.1. Sensor working principle

The measurement device included in the grip relies on an optical working principle, from which the name of OPTical INceptor (OPT-IN), commonly referred to as Frustrated Total Internal Reflection (FTIR) (Ref. [24]). It consists on the fact that, considering an interface between two media of sufficiently differing refraction indices:

- if encountered by an electromagnetic wave, the latter is reflected back into the first medium;
- if encountered by an evanescent wave, exponentially decaying in space, the latter is transmitted into the second medium.

The case of interest is the second one, in which the refracted wave can carry energy, that can be detected by an appropriate sensible element (e.g., a photoresistor). The amount of light refracted is proportional to the contact area between the two media. Preliminary studies already conducted (Ref. [25]), which demonstrate the viability of such an application, serve as the foundation for the first prototype's realization, which is presented in Ref. [26]. In Figure 3.1 is shown the core element of the sensor: a transparent cylinder (1), illuminated by two LEDs placed at the top and bottom facing to each other (2).

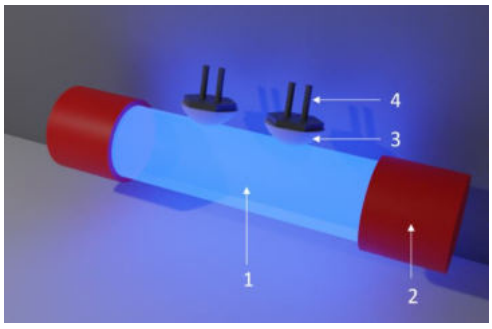

Figure 3.1: OPT-IN main components (Ref. [26])

The material of the cylinder is selected such that total reflection of the LEDs light is guaranteed and in the developed prototype plexiglass is used. As explained in Ref. [27], to achieve the total refraction in the cylinder, the LED light must hit the plexiglass base with a maximum angle, which value can be obtained exploiting the Snell's law:

$$\frac{\sin(\alpha_r)}{\sin(\alpha_i)} = \frac{n_1}{n_2} \tag{3.1}$$

where:

- α_r is the angle of the reflected beam of light, which is set to 90° to find the limit angle;
- α_i is the angle of incidence of the beam light that is needed to be found;
- n_2/n_1=1.5 is the refractive index of plexiglass with respect to air.

With these conditions, the obtained critical angle is:

$$\alpha_{i_{cr}} = 42° \tag{3.2}$$

thus, taking into account a margin, the maximum angle to be considered is equal to 40°. Regarding the LEDs color, in Ref. [27] it has been demonstrated that the blue light is the best choice for the functioning of the device in terms of minimum luminosity detectable and sensibility to luminosity changes.
The other elements of the sensor are the individual force transducers (3,4), that are constituted by a hemispherical-shaped component of transparent elastic material (3), placed in front of a photoresistor (4). The hemispherical components are manufactured using silicon in the developed prototype, but other materials can be used for the same scope. About their shape, there are no restrictions and they are selected to be hemispherical in order to obtain a variation of the area of contact with the pressure which is as close as possible to linearity (Ref. [27]).

The working principle of the sensor relies on the fact that when the hemispherical part is in contact with the cylinder, through the contact area the light reflected in the cylinder is frustrated, allowing it to be transmitted in the hemispheric probe. Since the contact area is proportional to the contact pressure, the sensor is able to produce a signal proportional to the pressure applied by the pilot hands on the control inceptor grip. The photoresistor varies its resistance in response to the quantity of light passing through, which in turn depends on contact area between the hemispheric cell and the cylinder. In particular, the photoresistor resistance decreases with the increasing amount of light received.

The electrical scheme explaining the usage of the photoresistor is reported in Figure 3.2.

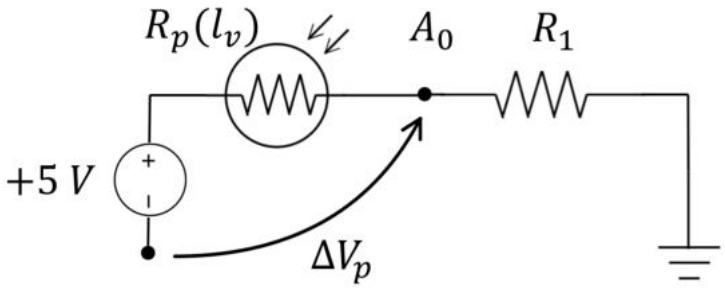

Figure 3.2: Electrical scheme with the photoresistor

The circuit consists, from left to right, on a constant voltage generator (which erogates $5V$), on the photoresistor itself and on a constant-resistance resistor. The latter is necessary, otherwise the voltage drop across the photoresistor would remain equal to 0 over time, independently from the amount of light. By exploiting the first Ohm's law:

$$\Delta V_p = R_p(l_v)i \tag{3.3}$$

where

- ΔV_p is the voltage drop across the photoresistor;
- $R_p(l_v)$ is the photoresistor resistance, that is function of the light intensity l_v;
- i is the current intensity crossing the photoresistor;

by measuring ΔV_p, since the current intensity i is known, it is possible to monitor the value of the resistance $R_p(l_v)$. After doing an opportune calibration process consisting in the application of known loads to the sensor and in the reading of the corresponding value of $R_p(l_v)$, it is possible to get a correlation between the load (pressure) applied and the light intensity, i.e., it is possible to get the relation $l_v = l_v(R_p)$ (see Section 3.4). From the practical point of view, the two ends of the circuit are the positive and the negative wires of Arduino. Since in the prototype realized there are four photoresistors, there are four analogue acquisition channels, to which are added two positive and negative cables.

3.2. Design overview

The load cell is integrated in the handle: some parts of the grip slide with respect to the rest of the grip itself so that, when pressure is applied, they are free to sink by a small amount—almost imperceptible to the pilot—but significant enough to result in a change

in contact area that can be measured. As can be seen in Figure 3.4, in the prototype designed there are two movable parts, each with two load cells. The choice of the location of the movable parts, other than being constrained by the limited space available, has been carried out on the basis of the way in which the pilot holds the collective grip, resulting in a movable part on the front and in one on the back. In order to produce a value that is averaged over the region of interest, the two photoresistors of each load cell are connected in series. Each load cell is connected through two wires to a voltage reader, which makes the values available for any device in a range between 0 and 5 V, without requiring any conditioning. In the following of this section are described the main modifications with respect to the existing design, i.e., the one of [7]. The first modification consists in the split of the grip into top part (Figure 3.3) and bottom part (Figure 3.4). This decision is made so that it is possible to mount different types of grip head, without the need of changing the lower part containing the OPT-IN cylinder. Moreover, this split makes it possible to quickly replace the LED of the cylinder in the event that it stops working. The two parts of the grip are held together by two screws. To avoid the contact between the screws and the 3D printed parts, threaded inserts are used in the holes of the grip bottom part.

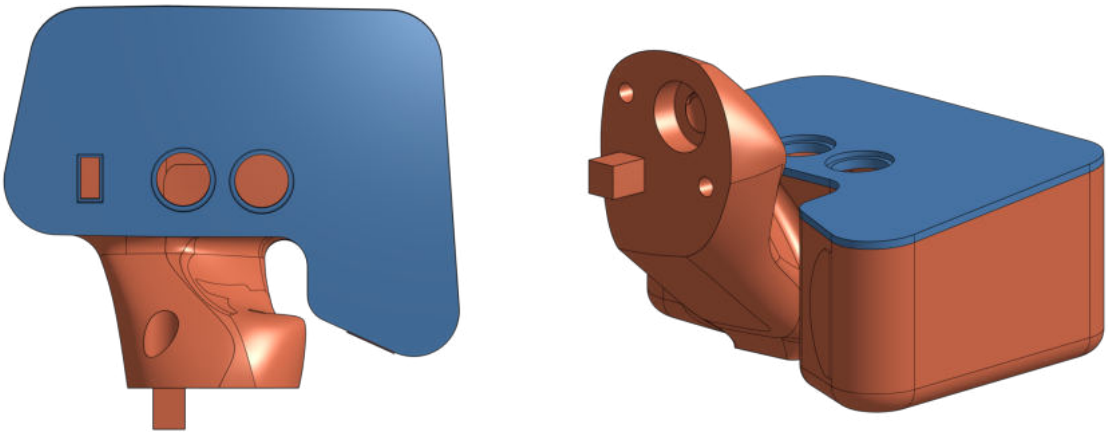

Figure 3.3: Grip top part

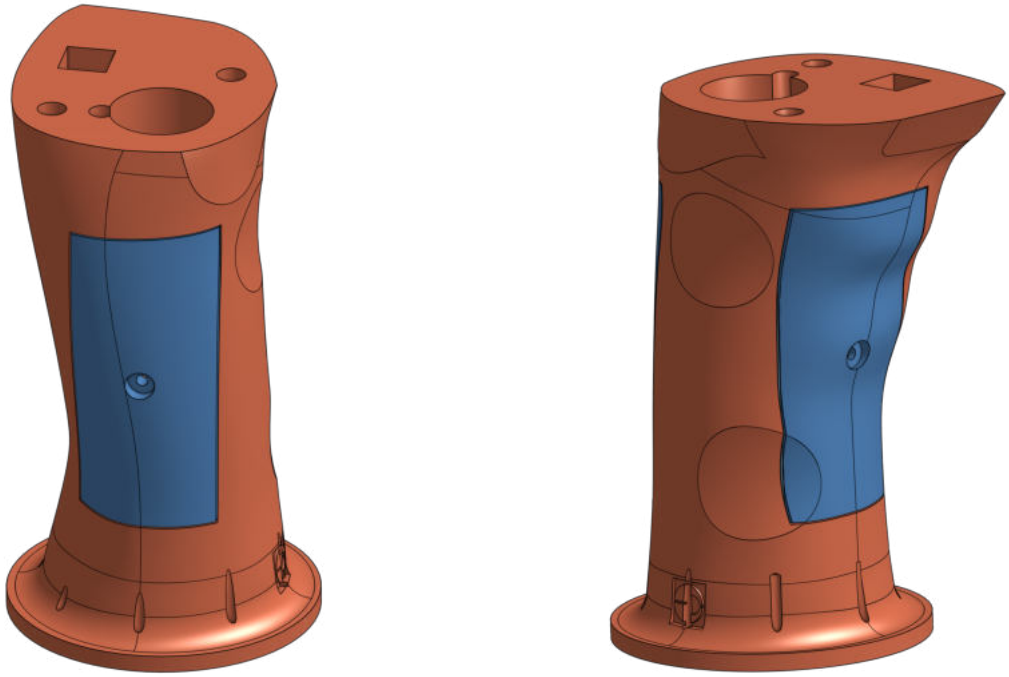

Figure 3.4: Grip bottom part (front view on the left, rear view on the right)

As can be seen in Figure 3.3, three button inserts have been predisposed. The next modification consists in the creation of an internal slot for the needed cables, so that they are not visible on the grip surface. This corresponds to the groove adjacent to the OPT-IN cylinder hole visible in Figure 3.4. Considering the general position of the collective inceptor with respect to the horizon, it was deemed appropriate to reinforce the connection between grip top and bottom part by creating a plug-like element on the grip head (and the corresponding slot in the grip bottom part), as can be seen in Figure 3.3.

It has been decided to change the optical load cells mounting: instead of fixing them through screws, a sock-like casing is used because:

1. to put a screw on the 3D printer resin is not a best practice, since the screw cannot be removed in a second moment (except by drilling the resin);
2. in this way OPT-IN is preloaded, enhancing the signal-to-noise ratio, since the null-pressure loading condition output is in this way shifted of a constant amount.

The internal part of the load cells (both the front and the rear one) is modified adding a support for the photoresistors, as can be seen in Figure 3.5 (left). The final connection between the sensing device and the cylinder can be seen in Figure 3.5 (right).

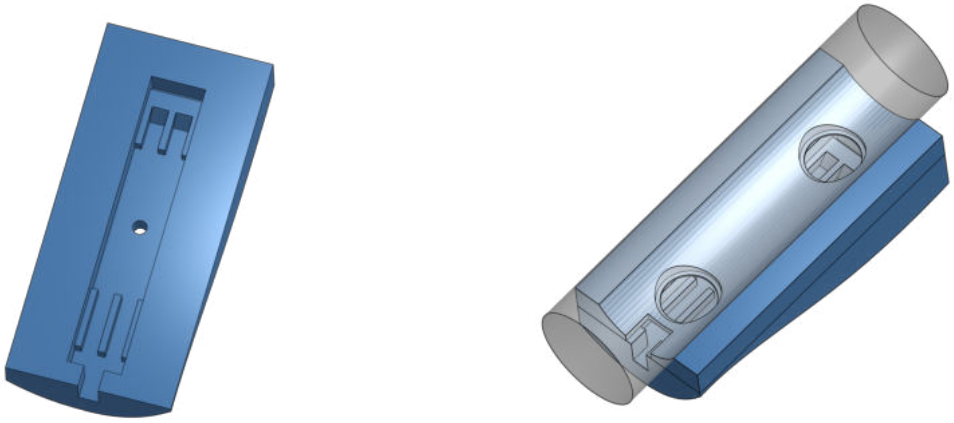

Figure 3.5: Load cells internal modifications (left) and connection with the OPT-IN cylinder (right)

Figure 3.6 shows an exploded view of the OPT-IN components: (1) is the cylinder, (2) the elastic component, (3) the photoresistor, (4) the inner portion of the sliding part, (5) the outer one (the one in contact with the pilot's hand), (6) the LED source and (7) the case containing the latter.

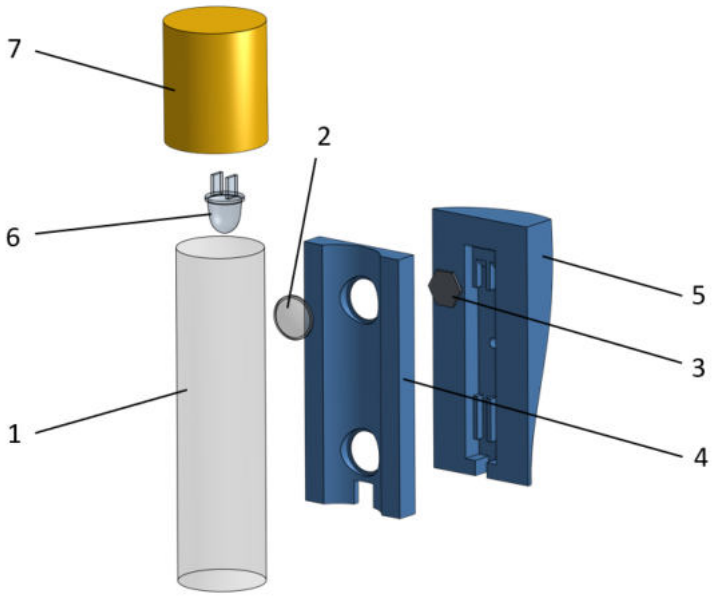

Figure 3.6: Exploded view of the OPT-IN components

The inner and outer parts of the sliding portions of the grip, as can be see in Figure 3.7, are connected through a nut-screw coupling.

Figure 3.7: Connection of the inner and outer parts of the sliding portions of the grip

The final prototype, including the joint element for the stick, is reported in Figure 3.8. This prototype has not been printed, as explained in Section 3.6.

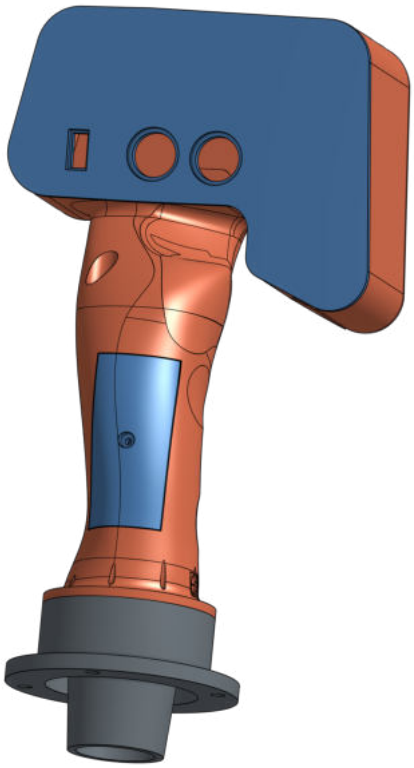

Figure 3.8: Grip final prototype

3.3. Wiring

The system's wiring must be capable of reading the voltage across each photoresistor and supplying the LED with the proper voltage and current. To do that, an Arduino UNO board is used, which provides the required voltage to the LED and reads the values of the photoresistors through the analog pins available. Data are transmitted via a USB cable connecting the Arduino board to the desired device to read the real-time data stream via serial communication.

In Figure 3.9 is reported a section view of the grip. For visualization purposes, different section planes are used for the grip lower and upper part. One can notice that in the grip top part, above the cylinder, there is a slot channel to allow the needed wiring cables to go from the grip head, where the Arduino board is placed, throughout the grip, eventually going out from the grip-stick joint element.

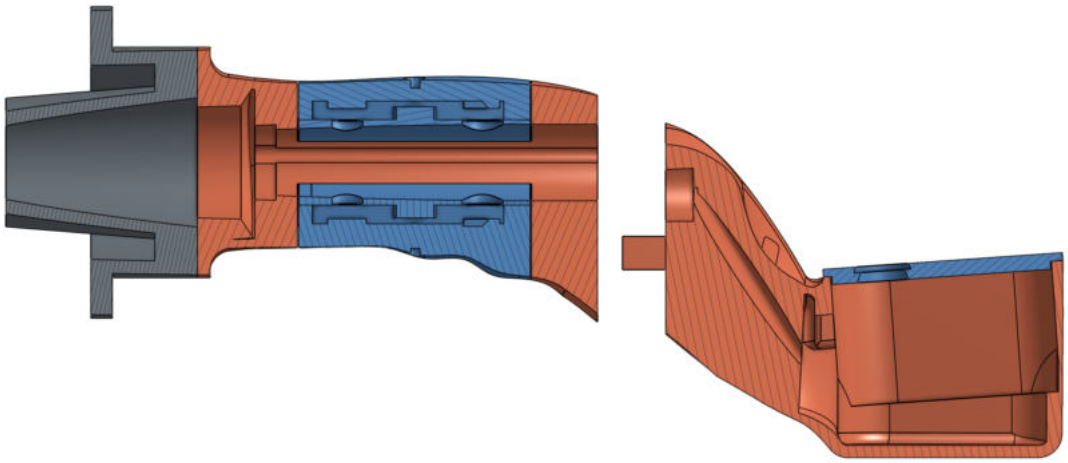

Figure 3.9: Section view of the grip

3.4. Data acquisition

As anticipated, a calibration process was conducted during previous studies (Ref. [27]). The resulting curve is reported in Figure 3.10.

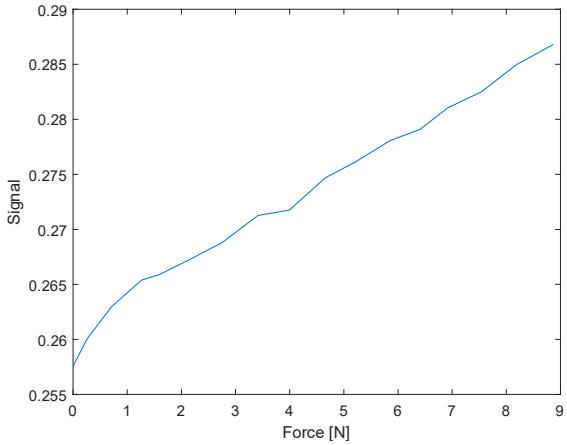

Figure 3.10: OPT-IN calibration curve

Despite the presence of sources of non-linearity, as:

- the fact that the photoresistor behavior is not perfectly linear;
- the fact that the contact area between the cylinder and the hemispherical elastic material is non-linear;

the relation shown in Figure 3.10 is globally linear, also considering that the range of interest for the cyclic stick is $0 \div 5kg$. In the y-axis is reported the digital value of the signal. The analog-to-digital conversion is performed by Arduino; the feature of interest of the converter are:

- resolution, which defines the minimum detectable pressure;
- sampling frequency.

The signal value is then normalized between 0 and 1, so that it is possible to use different acquisition boards. Since the indication of the pressure is qualitative (being, as said, a normalized value), to get a quantitative information it is necessary to perform a calibration procedure by the use of known loads. The load application must be repeated at different frequencies due to the deformation transient of the hemispherical probes. The acquisition frequency of the OPT-IN sensors is 40 Hz, which is the maximum capability of real time USB communication allowed by the selected microcontroller.

3.5. Algorithm overview

The data are acquired by the Arduino UNO and a value ranging from 0 to 1023 is read for each sensing element. The data coming from the sensing elements are combined according

to the following scheme:

$$\begin{bmatrix} K_{11} & K_{12} \\ K_{21} & K_{22} \end{bmatrix} \begin{Bmatrix} Av_f \\ Av_r \end{Bmatrix} = \begin{Bmatrix} C_1 \\ C_2 \end{Bmatrix} \tag{3.4}$$

where:

- Av_f, Av_r are respectively the value read from the front and rear sensing element;
- K_{ii} are values of the gain matrix that gives different importance to each sensing element in each direction;
- C_i is the resulting force in any given direction.

The data set coming from the sensing elements could also be used to integrate and improve the flight control system of the aircraft by adding information that is usually not available:

- a consistent increase in the mean average grip pressure could be related to an increase in the current MTE workload by the pilot and could be related to a higher risk of insurgent RPC phenomena;
- peaks in the applied force or rapid changes of it could be a sign of fatigue;
- oscillations at frequency 2.5-5 Hz could be a sign of unwanted RPC taking place.

3.6. Grip final prototype

During the development of the thesis work, there was the opportunity to design and realize a new collective grip, that can be seen in Figure 3.11, in which the OPT-IN arrangement is included.

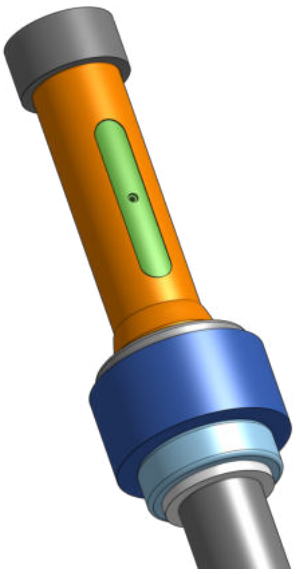

Figure 3.11: Collective grip in which the OPT-IN arrangement has been added

As can be seen, this grip does not aim to reproduce the external shape and ergonomics of the input device, but it is a solution focused on the integration of the pressure sensor and of a load cell, that in Figure 3.11 is represented by the blue element. One of the peculiarities of this grip is the fact that it has a metal core, which permit to overcome the problems related to the structural strength of the 3D printer resin. An exploded view of the grip, in which the metal core and the pressure sensors can be visualized, is reported in Figure 3.12

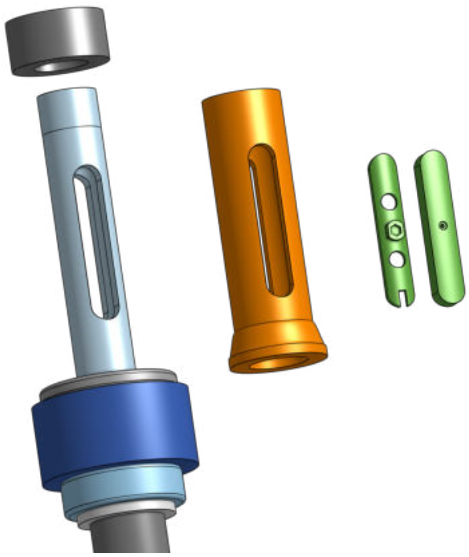

Figure 3.12: Exploded view of the grip final prototype

Figure 3.13 shows on the left the grip metal core with the illuminated cylinder inside and on the right the completely assembled grip, in which is possible to see the upper sensing element.

Figure 3.13: Final grip prototype pictures

4 | Collective grip sensor testing

4.1. Test setup

The experiment performed using OPT-IN aims to monitor the left-hand activity of the pilot on the collective stick of a helicopter during a flight containing different MTEs. The information about the translation of the collective inceptor are detected during the flight using MATLAB Simulink. The data of the two OPT-IN sensors are collected directly by the Arduino UNO microcontroller of Figure 4.1 and communicated via USB.

Figure 4.1: Arduino UNO microcontroller used for the OPT-IN sensors data acquisition

The experimental test-bed is the motion platform of the Department of Aerospace Science and Technology of Politecnico di Milano shown in Figure 4.2, which is composed of the following subsystems (Ref. [28]):

1. a 6-DOF Motion Platform System (MPS) Bosch eMotion 1500;
2. a reconfigurable cockpit mock-up;
3. a customized measurement system.

Figure 4.2: Motion Platform System (MPS) used as test-bed

The MPS is able to carry a maximum payload of 1500 kg and provides acceleration inputs of adequate intensity (in excess of $10m/s^2$) in the frequency band $[1, 7.5]$ Hz. The cockpit mock-up is composed of the pilot seat, collective and cyclic inceptors (Figure 4.3), pedals, and a glass cockpit made of two monitors. The cockpit structures are supported by stainless steel frame. The rotation of the inceptors is measured by 3 absolute encoders.

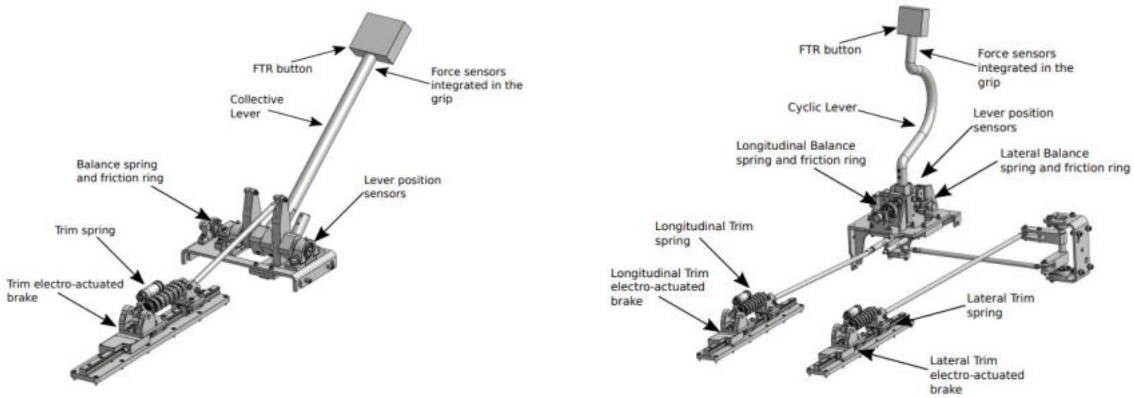

Figure 4.3: The RPC test-bed collective inceptor (left) and cyclic inceptor (right) control chain (Ref. [28])

The motion platform system is not a helicopter flight simulator, being its main purpose the study of the pilot-vehicle interaction due to an external input: the motion is predetermined and acts as a disturbance for the pilot during the MTEs execution. Tasks involve the chase of a target both with cyclic and collective inceptors. As a matter of fact, even though the cyclic inceptor is not of particular interest for the purpose of this work, it has been decided to make the tested subject using it in order to more faithfully reproduce the typical helicopter flight condition. The pilot shall execute the MTE by looking at the target shown on the screen: it is represented by two magenta stars that move on a plane following a determined path. A dot is controlled by the pilot and moves according to the motion of the cyclic stick (horizontal motion of the dot controlled by lateral input, vertical motion of the dot controlled by longitudinal input). Another dot moves according to collective inceptor, for which the path of the target is just vertical. An example of the MTE screen is shown Figure 4.4.

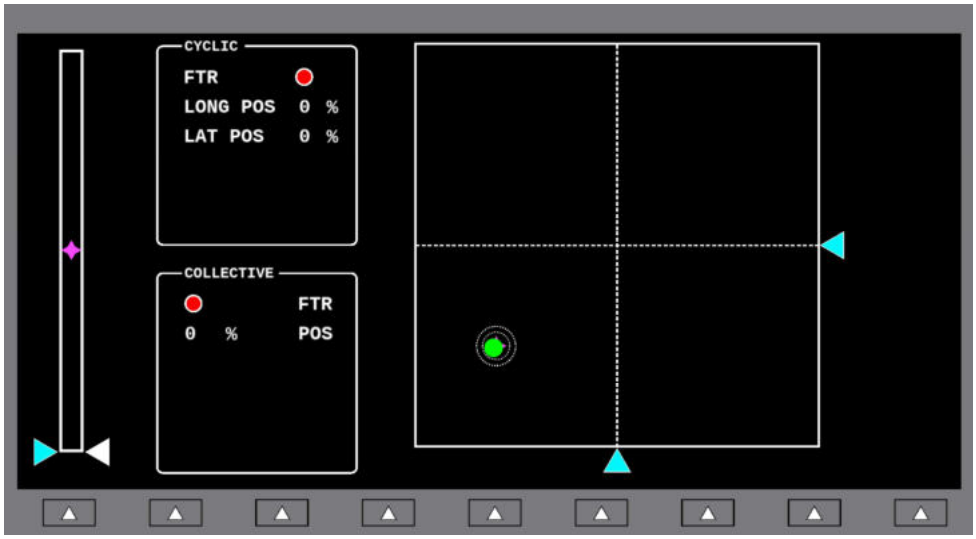

Figure 4.4: MTE screen of the MPS

The goal is to overlap the two dots with the magenta stars as much as possible throughout the entire duration of the MTE. The dot indicating the control inceptors position is green, yellow or red, depending on the accuracy of the overlapping with the targets (respectively, optimal performance, acceptable performance and unacceptable performance). It is possible to set the thresholds for the change of the dot color and for the test performed two sets of thresholds are used, which are reported in Table 4.1.

Threshold	Green limit [%]	Yellow limit [%]	Red limit [%]
Narrow	1	3	> 3
Wide	3	5	> 5

Table 4.1: Optimal performance (green), acceptable performance (yellow) and unacceptable performance (red) sets used in the tests

The threshold is intended as the percentage error between the target and the input position. The type of threshold is kept constant in each test and the tested subject is not informed about the type of threshold adopted. Two tests are performed without motion of the platform to serve as workload reference level, then the other tests are performed using a motion on the vertical direction with $RMS = 1\ m/s^2$ and $RMS = 1.5\ m/s^2$. Table 4.2 summarizes the tests performed with the relative characteristics.

Test	Motion RMS [m/s^2]	Thresholds type
1	-	Wide
2	-	Narrow
3	1.0	Narrow
4	1.5	Narrow
5	1.0	Wide
6	1.5	Wide

Table 4.2: Test summary table

4.2. Results

Even though it is necessary to carry out the tests on a larger statistical sample, which is left to future developments, hereinafter are reported the results obtained with one tested subject. In Figure 4.5 is reported, for each test, the grip average pressure exerted by the tested subject. The pressure is expressed in *levels*, which is not the usual unit of measure for a pressure measurement, but this is not critical for the present analysis, since the focus is on the relative variation of the grip pressure rather than its absolute value. Since the trend in time of the pressure exerted on the upper and on the lower sensing elements of the grip is similar, the average between the two sensing elements output is reported.

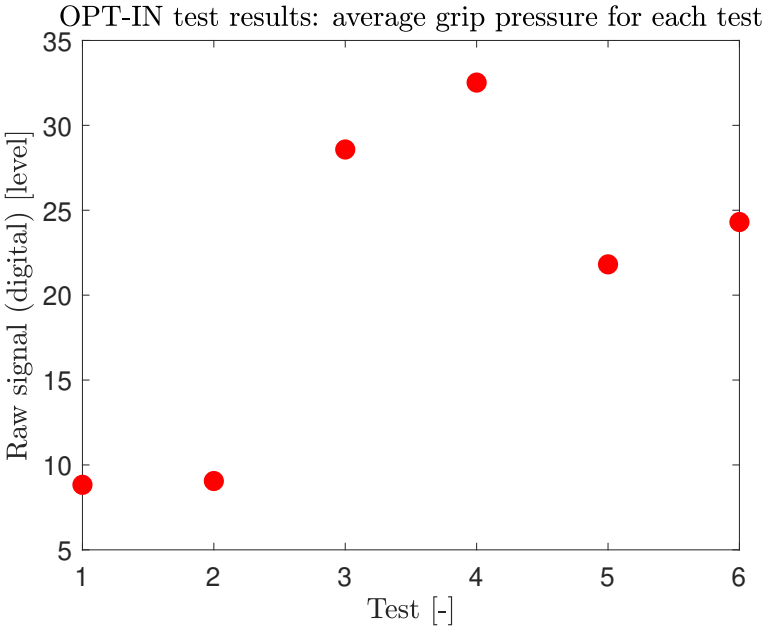

Figure 4.5: OPT-IN results: average grip pressure for each test

It is possible to see that the pressure applied on the grip for the first two tests (the ones without platform motion) is relatively low if compared with the results of the other tests. Moreover, there is not a relevant difference between the results of the first two tests, index of the fact that the pilot workload, with the platform at rest, does not significantly increase as the thresholds are tightened. The results of the tests 3 and 4 show that the pilot workload level is higher with respect to the one of the tests without motion. Moreover, it is possible to see that the grip average pressure for the test with higher motion RMS is higher than the one with lower RMS. Similar considerations apply to the results of the last two tests. The comparison between the results of tests 3 and 5, that are performed at the same platform motion RMS but with different sets of thresholds, shows that the average grip pressure of test 3 (the one with narrower thresholds) is higher than the one of test 5 (the one with larger thresholds). Analogous considerations apply to the comparison between tests 4 and 6. In particular, it is possible to see that, being the thresholds wider with respect to the ones of the previous two tests, the average grip pressure is lower with respect to the one of the tests 3, 4. To have an indication of the accuracy with which the tested subject followed the target, Figure 4.6 and Figure 4.7 show, for each test, the comparison between the time histories of the target, which has a sinusoidal trend over time, and the input.

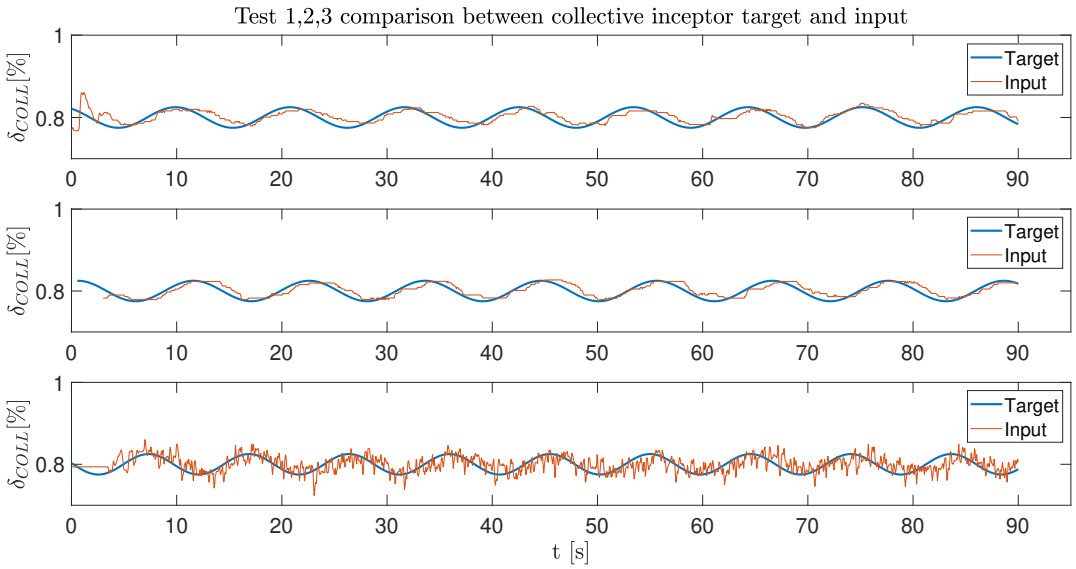

Figure 4.6: Comparison between the time histories of collective inceptor target and input for the test 1-2-3

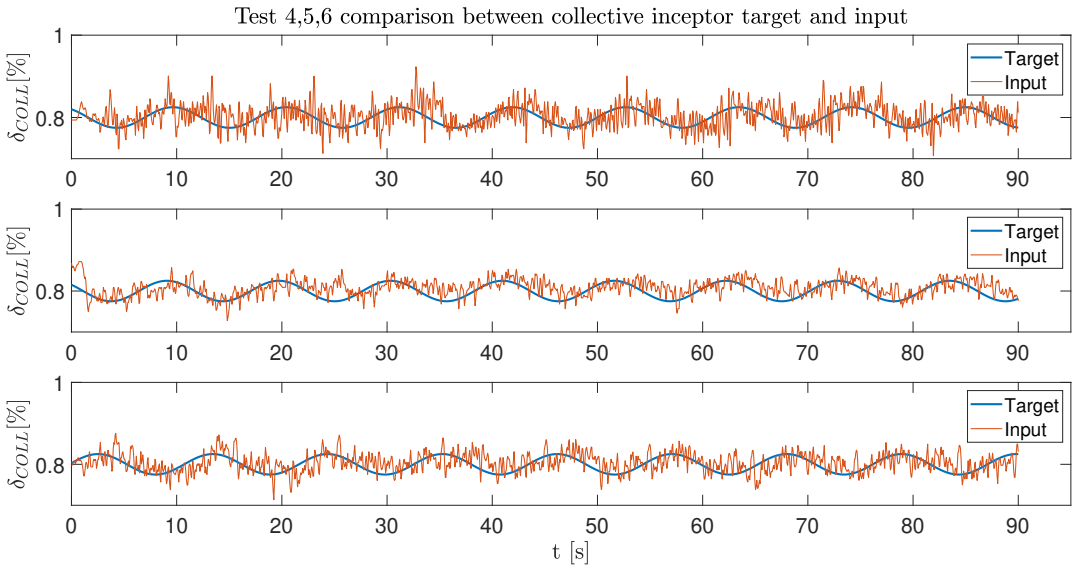

Figure 4.7: Comparison between the time histories of collective inceptor target and input for the test 4-5-6

As expected, in the first two tests, that are without platform motion, the input follows the target with relative small error. It is possible to appreciate a relative small shift (i.e., delay) between the target and the input, that is due to the human reaction time. The comparison between tests 3 and 4 shows that, fixed the threshold type, the oscillations of the input are larger in the case with larger motion RMS (test 4). The same applies

to the comparison between tests 5 and 6, that show oscillations with smaller amplitude if compared respectively to tests 3 and 4. This is due, other than the wider thresholds used for tests 5 and 6, to a "learning process" of the tested subject, which during test 4 declared that an improvement of the performance was obtainable by relaxing the arm muscles rather than stiffen them. In Figure 4.8 is reported the standard deviation of the control input for each test, computed as:

$$\sigma = \sqrt{\frac{\sum_{i=1}^{n}(\delta_i - \bar{\delta})}{N-1}} \tag{4.1}$$

where:

- δ_i is the $i-th$ sample of the control input;
- $\bar{\delta}$ is the average control input;
- N is the number of control input samples.

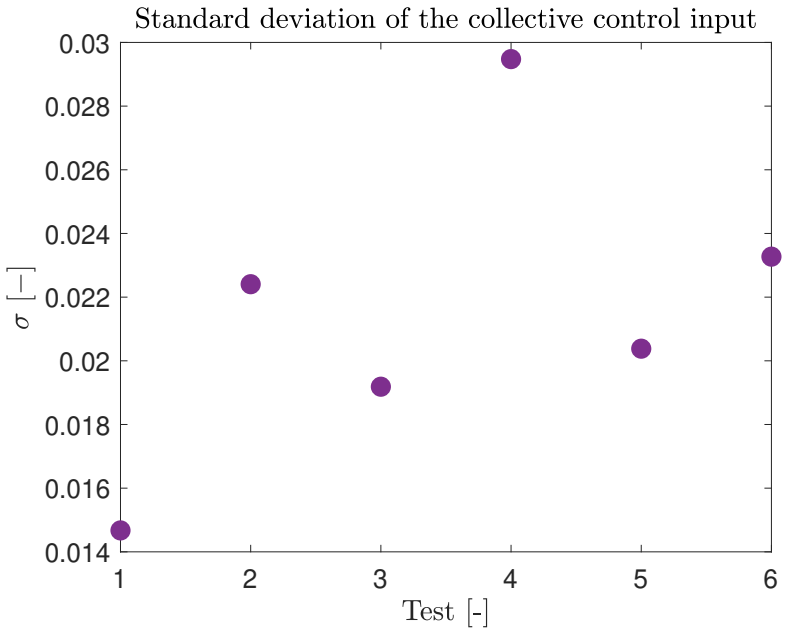

Figure 4.8: Standard deviation for the collective control input

It is possible to see that the global trend of the standard deviation is analogous to the one of the OPT-IN sensors, reported in Figure 4.5.

Figure 4.9 reports, for each test, the *aggression* parameter, a workload index defined as:

$$A(\delta) = \frac{1}{T}\int_{t}^{t+T} |\dot{\delta}| dt \tag{4.2}$$

where:

- T is the time interval used for the parameter calculation, considered equal to the whole acquisition time in the present analysis;
- $\dot{\delta}$ is the time derivative of the control input.

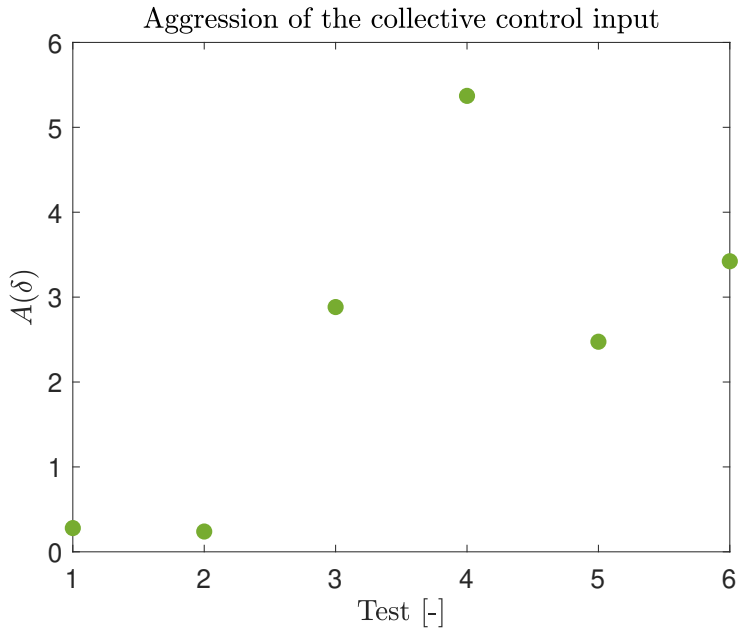

Figure 4.9: Aggression parameter for the collective control input

The overlap of the OPT-IN measurement with the aggression parameter (both normalized) reported in Figure 4.10 shows a strict correlation between the two, indicating that the OPT-IN outputs can be effectively considered related to the pilot workload level.

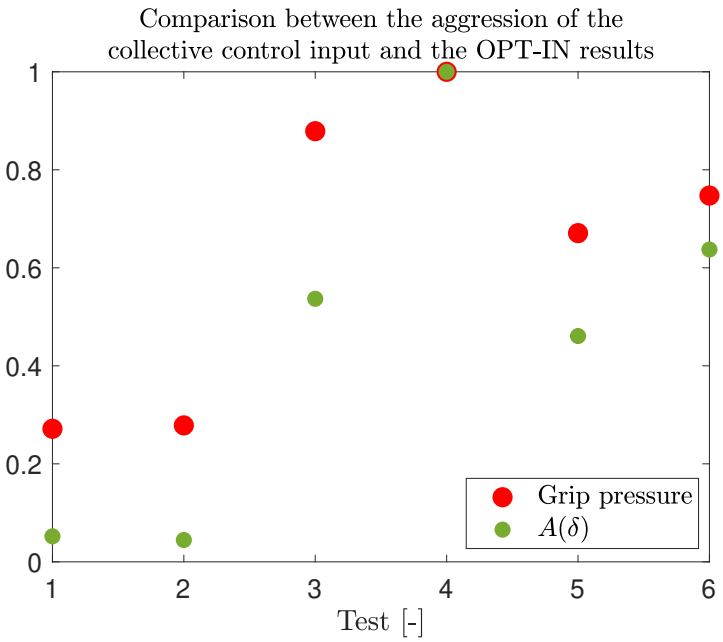

Figure 4.10: Overlap of the OPT-IN measurement with the aggression parameter (both normalized)

Another workload index is the moving median absolute deviation, defined as:

$$M_{AD}(\delta) = M_e(|\delta_i - M_e(\delta)|) \tag{4.3}$$

where:

- $M_e(x)$ is the median of x;
- δ_i is the $i-th$ sample of the control input.

This parameter is reported in Figure 4.11, overlapped with the OPT-IN results (both normalized), and also in this case the global trend is correlated with the ones of the indexes previously computed.

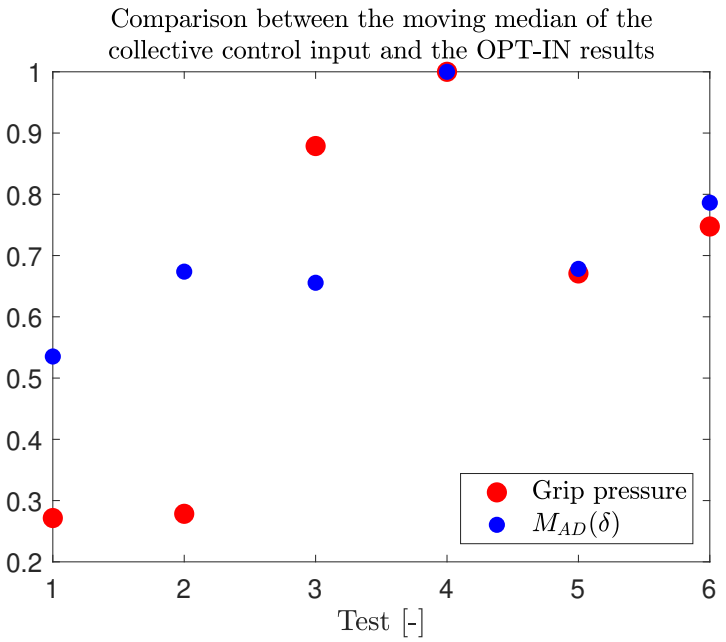

Figure 4.11: Moving median absolute deviation for the collective control input

A final analysis focuses on the NASA-TLX rating scale results. The rating scale questionnaires have been completed by the tested subject using the dedicated application installed on a tablet. The results are reported in Figure 4.12.

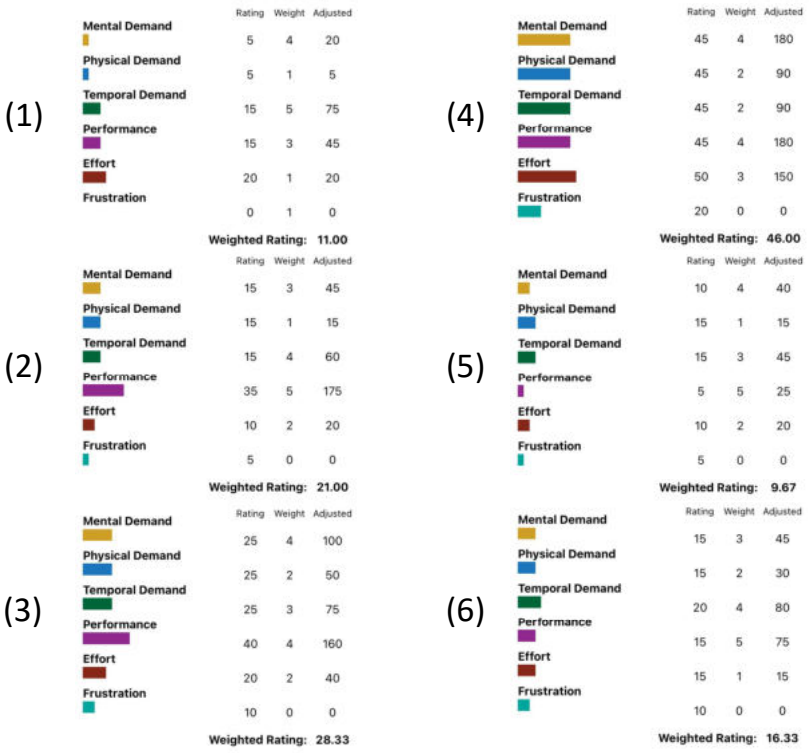

Figure 4.12: NASA-TLX rating scale results

It is possible to see that the global trend of the rating scale items follows the trend shown by the workload indexes previously computed. In particular, Figure 4.13 reports the weighted NASA-TLX rating for each test, which shows a trend clearly analogous to the ones of the workload indexes.

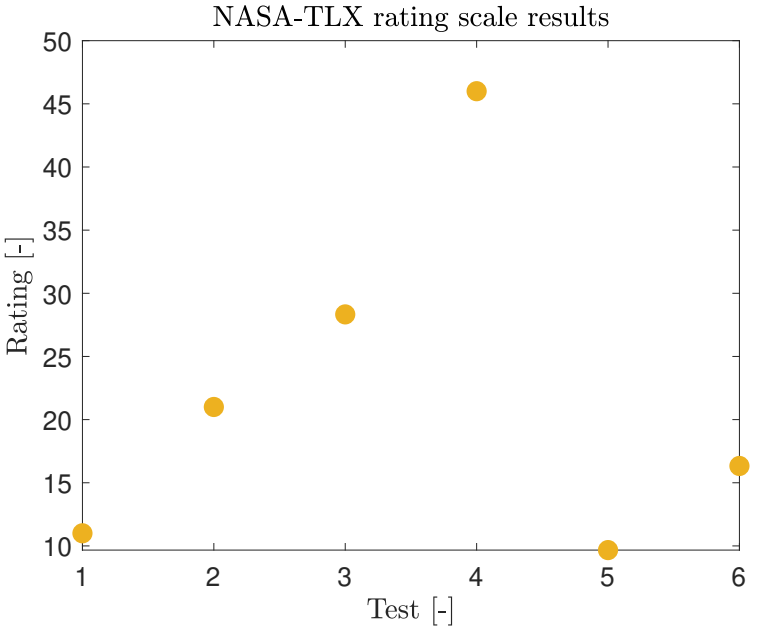

Figure 4.13: NASA-TLX weighted rating results

5 | Cyclic inceptor stick design and realization

The second part of the thesis consists on the design, realization and the consequent use during tests of the cyclic stick of a helicopter. It is made of carbon fiber-reinforced composite material in which optical fiber sensors are embedded in order to monitor the stick deformation and, in turn, the loads applied by the pilot. Since the stick will be used in a motion platform and not in a real flight environment, it is not subjected to the requirements to make it flyable.

5.1. Stick's current prototype vs new prototype

A preliminary prototype of a similar stick without the optical fiber sensor, reported in Figure 5.1, has already been realized at the Politecnico di Milano Department of Aerospace Science and Technology. The technique used for the production was the dry lay-up, i.e., purposely cut plies of pre-preg were placed over each other and stacked on purposely built polyurethane mould and counter mould, reported in Figure 5.2, to form the desired shape. One of the critical issues of this technique is the fact that the component is realized in two separate halves joined together by overlapping them and, as a consequence:

- the continuity of the carbon fiber is not guaranteed;
- the thickness control is poor.

Figure 5.1: Preliminary prototype of the stick, without the optical fiber sensor

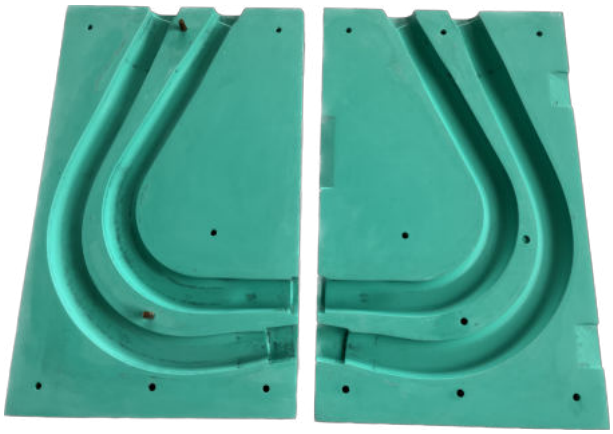

Figure 5.2: Mould and counter mould for the stick realization

The prototypes proposed in this thesis are instead realized, other than by the use of the mould-counter mould, by the employment of a soluble mandrel internal to the stick, ensuring a superior control over the thickness of the final product. As a matter of fact, in this technique the pre-preg plies are wrapped around the mandrel, minimizing the overlapping regions. Three sticks are realized:

- the first prototype is used as technological fine-tuning: given the not-trivial geometry of the stick, it has been decided to realize a prototype with the optical fiber without the sensors;
- the second prototype is used as technology demonstrator including the optical fiber sensors, the position of which is the result of the optimization process described in Section 6.6; in order to not be bound by the production waiting times of a unique optical fiber with the sensors positioned in the correct (optimized) position, this

prototype is realized using two optical fiber sensors on two different optical fibers, in order to allow the reposition of the sensors in the desired positions;

- the third prototype is the final one, including a larger number of sensors included in the same optical fiber; due to the production waiting times of the optical fiber with the sensors spaced out by the custom amount, this prototype will be realized in the future.

5.2. Stick realization motivation

There are two main points which require motivation regarding the realization of the stick, that are, the utilization of a carbon fiber composite material and the sensorization of the stick itself. About the first point, the main reason for using a composite material is not, as in most cases, the high strength-to-weight ratio (which certainly is an advantage), since the loads applied to the stick in a normal flight condition are well lower than the limit ones of steel and aluminum, which are the two materials currently employed for the control stick realization. One of the main advantages is, instead, the weight saving itself. Considering the stick isolated, the weight saving amounts to 92% with respect to the weight of the same stick made of steel and to 77% with respect to the one made of aluminum. The weight reduction is significant, also considering the fact that the control inceptors are doubled. The weight saving does not merely reduce to the one of the stick itself, but also to the lumped masses that are needed below the inceptor elbow to make the inceptor balanced, i.e., such to have its center of gravity on the elbow itself. As an example, in Figure 5.3 is reported the comparison between the lumped masses needed for the stick made of steel, for the one made of aluminum and for the same made of composite material, considering the same grip and assigning to it a typical mass value. The lumped mass saving with respect to the steel stick is of 74% and the one with respect to the aluminum stick is of 48%. The overall weight saving is relevant, in both cases. The drawback with respect to the use of steel and aluminum is the cost increase.

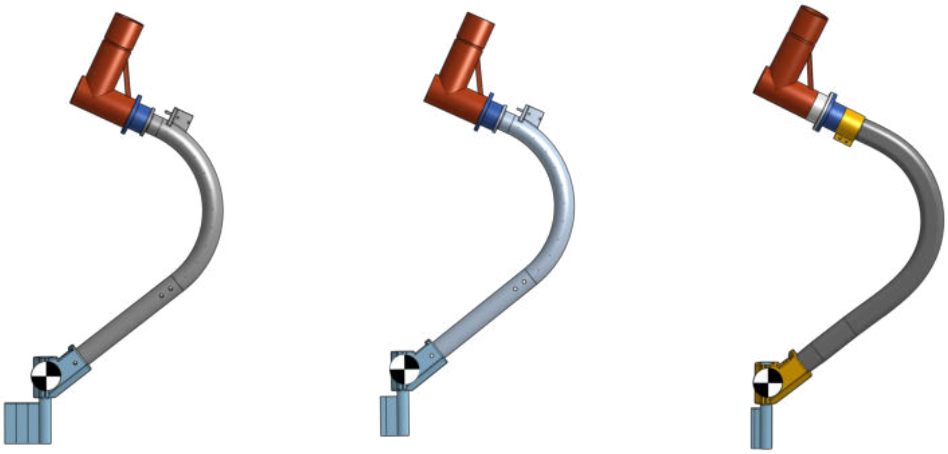

Figure 5.3: Steel (left), aluminum (center) and carbon fiber-reinforced composite material (right) stick: lumped masses needed for balancing comparison

The second motivation, i.e., the reason why realize a sensorized stick, lies on the fact that the measure of the loads applied to the stick has a paramount importance in the prevention and study of RPC phenomena. As a matter of fact, the sensors embedded in the stick allows to measure the force applied by the pilot without the use of costly, heavy and cumbersome load cells, which are not usually present in production helicopters. The force measurement allows to compute one of the two fundamental indices of the pilot-vehicle interaction, that is the BDFT. The classical BDFT is the transfer function relating the vehicle acceleration $\ddot{x}$ (input) and the control deflection δ (output):

$$H_{BDFT}(s) = \frac{\delta(s)}{\ddot{x}(s)} \tag{5.1}$$

The BDFT which can be measured with the sensorized stick is instead defined using the pilot force F as output:

$$\tilde{H}_{BDFT}(s) = \frac{F(s)}{\ddot{x}(s)} \tag{5.2}$$

The computation of $\tilde{H}_{BDFT}$ is particularly useful in case of a high level of friction present in the controls. In this case, the motion of the inceptor is small and typically highly non-linear, while the force applied by the pilot is not, especially in high load factor flight conditions.

5.3. Optical fiber overview

Optical fiber has found increasing applications as sensor in which it is exploited the correlation between the external phenomena to which the optical fiber is subjected and

the properties of the light pulsing along it. It is easy to find examples of aerospace, structural, medical and chemical applications for vibration, temperature, strain, impact and general structural health monitoring (Ref. [29]). Optical fiber-based sensors provide a number of benefits, including their light weight, compact sizes, good sensitivity, good long term stability, corrosion resistance and immunity to magnetic and electromagnetic interference. Because of their modest sizes and compatibility with conventional polymeric materials, they may be easily incorporated inside a structure without causing a significant weakening of the material. As can be seen in Figure 5.4, the optical fiber is made of three different layers arranged concentrically, that are:

- *core*: central section made of silica, it is the high transmitting region of the fiber;
- *cladding*, it creates an optical wave guide that confines the light. It is usually made of silica;
- *coating*, that is a non-glass protective layer which gives the robustness to the inner layers.

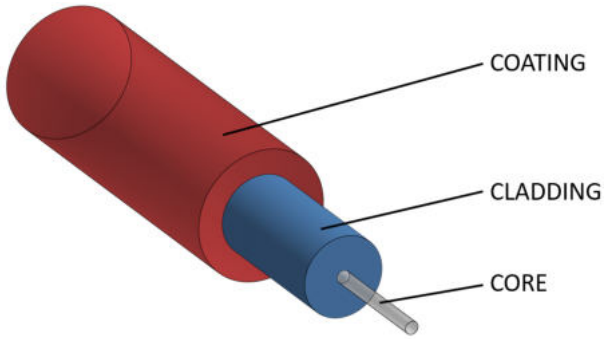

Figure 5.4: Optical fiber layers

The working principle takes place in the two inner parts of the optical fiber. There are no physical discontinuities between them: the only distinction is their refractive indices, which difference allows for total reflection of the signal at their interface and subsequent transmission of the signal inside the core. The refractive index n which characterizes a material is defined as:

$$n = \frac{c}{\nu} > 1 \tag{5.3}$$

where:

- c is the speed of light in vacuum;
- ν is the phase velocity of light in the medium.

Considering optical fiber glass, it ranges from 1.2 to 1.5. Figure 5.5 shows the interface between the core (refractive index n_1) and the cladding (refractive index n_2); considering an incident ray which forms an angle equal to θ_1 with respect to the normal to the interface, three situations are possible:

(a) $\theta_1 < \theta_{cr}$: in this case the ray is refracted in the cladding, forming an angle $\theta_2 < 90°$ with respect to the interface normal;

(b) $\theta_1 = \theta_{cr}$: in this case the refracted ray forms an angle $\theta_2 = 90°$ with respect to the interface normal, so it is parallel to the interface;

(c) $\theta_1 > \theta_{cr}$: in this case the refracted ray is actually a reflected ray, since $\theta_2 > 90°$, so it turns back into the core.

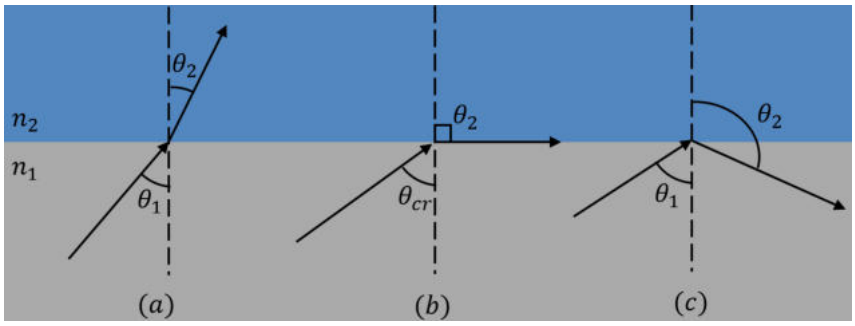

Figure 5.5: Interface between core and cladding: possible cases

The case of interest for the working principle of the optical fiber is the third one: by imposing an angle $\theta_1 > \theta_{cr}$ to the incident ray, it is possible to transmit it (and so the signal, i.e., the information) throughout the core. The only thing to know is thus the value of θ_{cr}, which is obtainable recalling the Snell's law, that applied to the schematics reported in Figure 5.5 reads:

$$\frac{\sin(\theta_1)}{\sin(\theta_2)} = \frac{n_2}{n_1} \tag{5.4}$$

and, by substituting $\theta_2 = 90°$ to find the critical angle, one obtains:

$$\theta_{cr} = \sin^{-1}\left(\frac{n_2}{n_1}\right) \tag{5.5}$$

It is necessary to be aware that not all the signals can be introduced in the optical fiber: looking at the spectrum of the light signal loss as a function of light wavelength on Figure 5.6, it is possible to see that there are three windows in which the loss of the signal is minimum, so the optical fiber has to be used inside these three transmission windows. For sensors application, the most common window is the third one, with wavelengths

ranging from $1.5\mu m$ to $1.6\mu m$, which is the one with the minimum attenuation. The three windows are in the range of NIR (Near-InfraRed), that is near the visible range but not inside it.

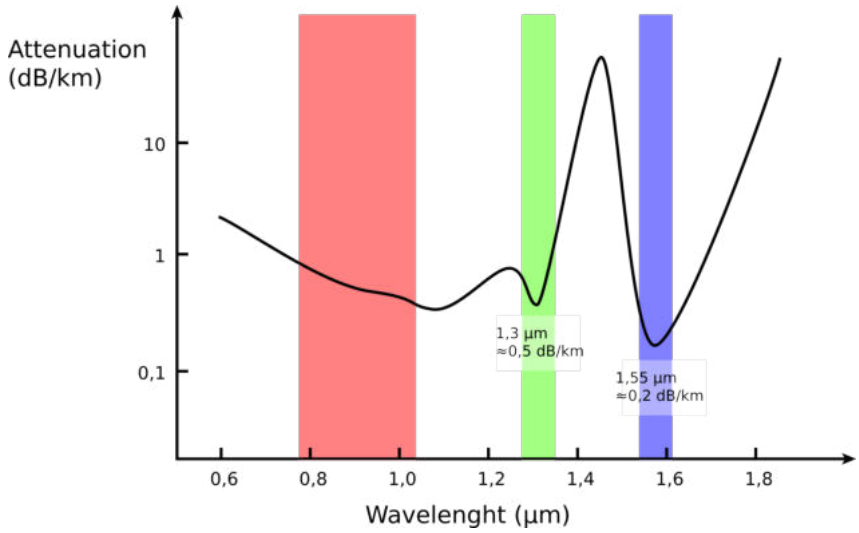

Figure 5.6: Optical fiber attenuation as a function of light wavelength (source: Wikipedia)

5.4. FBG sensors working principle

It is possible to obtain sensors using the optical fiber creating a correlation between the external phenomena to which the fiber is subjected and one of the following characteristics of light:

- amplitude change;
- phase shift;
- frequency shift.

The sensors used for the stick are based on the measure of the frequency shift of light and are commonly known as FBG sensors. The individual FBG is created by inscribing an invisible permanent periodic refractive index change in the core of the optical fiber, as can be seen in Figure 5.7.

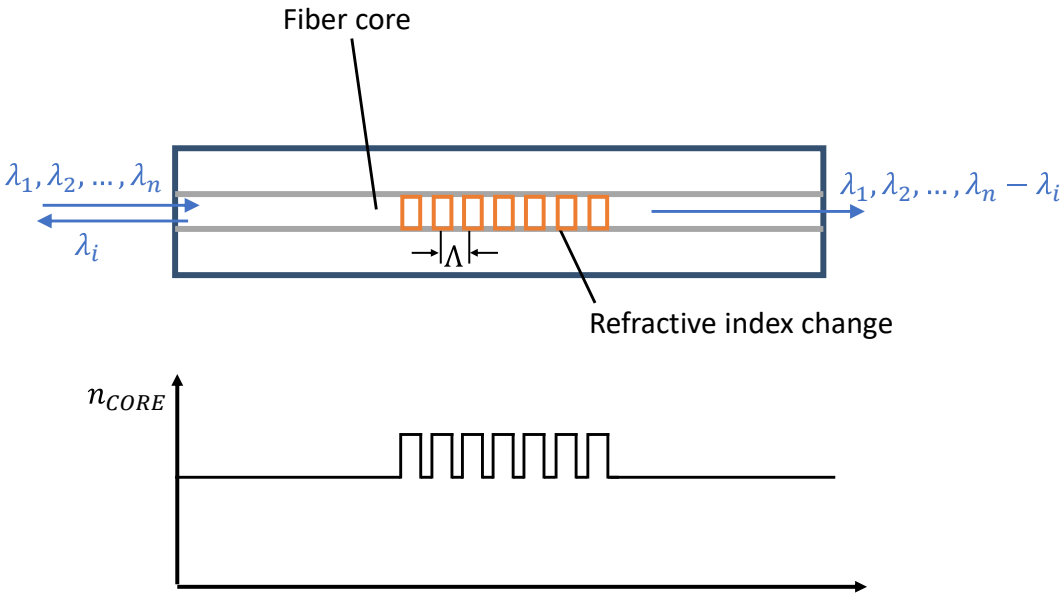

Figure 5.7: Grating of the optical fiber core

When an incident spectrum of light, characterized by the wavelengths $\lambda_1, \lambda_2, ..., \lambda_n$, propagates through the grating, a specific wavelength λ_i matching the Bragg grating wavelength, named *Bragg's wavelength*, is reflected back, while the rest of the spectrum is transmitted unaffected. This happens because, as can be seen in Figure 5.8, when a light is launched into a FBG, one particular wavelength is in phase with the grating period and is reflected back to the input end. All the other wavelengths pass through the other end, since they are not in phase with the grating period.

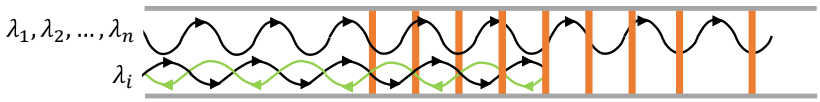

Figure 5.8: Wavelength not matching (above) and matching (bottom) the Bragg grating period

The value of the reflected wavelength can be obtained by writing the momentum conservation of the Bragg grating condition, which reads:

$$2\left(\frac{2\pi n_{eff}}{\lambda_B}\right) = \frac{2\pi}{\Lambda} \tag{5.6}$$

where:

- n_{eff} is the effective refractive index of the core;

- λ_B is the Bragg's wavelength;
- Λ is the period used for the modulation of the core, sometimes referred to as *grating pitch*.

Rearranging Equation 5.6 one obtains:

$$\lambda_B = 2n_{eff}\Lambda \tag{5.7}$$

Equation 5.7 is the basis of the working principle of the sensor: being the optical fiber embedded in the structure, if for example an axial strain is induced, the FBG sensor reacts accordingly, causing a shift in the reflected Bragg wavelength, as shown in Figure 5.9.

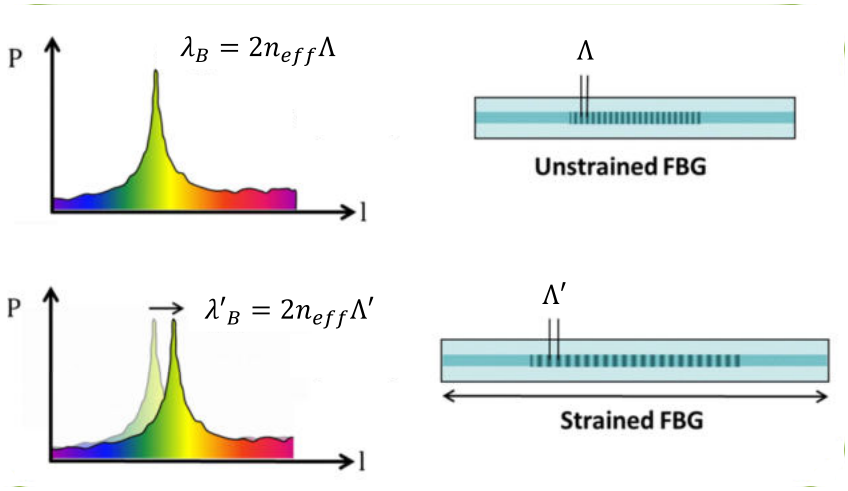

Figure 5.9: Spectral response of the reflected wave as a result of an axial strain (source: fbgs.com)

With one-time instrument calibration, strain parameters and other derived quantities can be measured dynamically by the use of an optical sensing interrogator, like the one of Figure 5.10.

Figure 5.10: Optical sensing interrogator

A key advantage of the FBG technology is that measurement points can be fabricated as an array on independent sensors along the same fiber, enabling *multiplex* or even *distributed measurements*. Note that the measured quantity is averaged over the grating length but, since the latter could range from 1 mm to 12 mm, the measure can be considered pointwise if a sufficiently small grating length is used. By differentiating Equation 5.7 one obtains:

$$\Delta\lambda_B = 2\left(\Lambda\frac{\partial n}{\partial \ell} + n\frac{\partial \Lambda}{\partial \ell}\right)\Delta\ell + 2\left(\Lambda\frac{\partial n}{\partial T} + n\frac{\partial \Lambda}{\partial T}\right)\Delta T \tag{5.8}$$

where ℓ and T are respectively the grating length and temperature. Being aware that in general the thermal effect has to be compensated/decoupled from the effect of the length variation, in the specific application of this thesis the variation of the temperature is negligible, hence this aspect can be ignored.
The method to *write* the grating inside the core is known as *cold-writing technique*. As can be seen in Figure 5.11, it is based on the use of an intense ultraviolet (UV) source such as a UV laser and an interference matrix (interference pattern), that is a mask which permits to modulate the refractive index of portions of the core in a precise way.

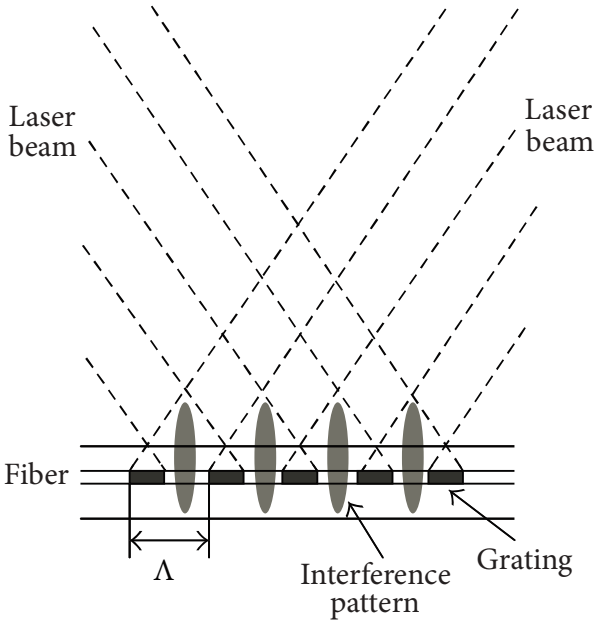

Figure 5.11: Cold-writing technique scheme (Ref. [30])

The fiber is embedded between the first and the second ply of the stick, considering that the greater the distance of the optical fiber from the neutral axis, the better the measure of the bending moment, which is the most relevant internal action to be measured.

5.5. Soluble mandrel design

The starting point for the design of the 3D printed soluble mandrel is the available CAD of the mould: the external surface of the mandrel corresponds to the internal one of the mould cavity, since the mandrel will be placed on the hollow of the stick. In this step it has to be considered an offset to give room for the pre-preg plies and for the lamination consumables. In particular, starting from the mandrel surface, it has to be considered the thickness of:

- 3 pre-preg plies, each of thickness 0.2 mm;
- teflon layer, of thickness 0.15 mm.

Notice that the offset has to be applied to the lateral surfaces only, since the length of the stick must be the same of the corresponding one on the mould, so no offset has to be used for the base surfaces of the mandrel. Up to this point, the mandrel is reported in Figure 5.12.

Figure 5.12: CAD of the full version of the mandrel

Then, since the mandrel has to contain the needed equipment for the autoclave cycle, the stick is transformed from being full to hollow (see Figure 5.13).

Figure 5.13: CAD of the hollow version of the mandrel

Considering the trade-off between rigidity and production costs, the thickness of the mandrel has been chosen to be equal to $5mm$. The optical fiber, which is embedded between the first two plies (starting from the internal surface) at some point must come out, so a support is needed to prevent it from breaking. The support is 3D printed and its geometry is removed from the one of the mandrel, as can be seen in Figure 5.14. For this operation, it has to be taken into account that the optical fiber support is covered by a ply, so an offset of $0.2mm$ has to be used. The support has a cavity where the optical fiber can pass, so it is necessary to be careful to prevent resin from entering. The support's cavity has a diameter of 1.2 mm because the optical fiber is protected by an outer plastic sheath with a a diameter of 1 mm. A margin of 0.2 mm is used to guarantee the sliding of the fiber inside the support, also considering the fact that in general a 3D printer tends to slightly tighten the holes diameter rather than widening it.

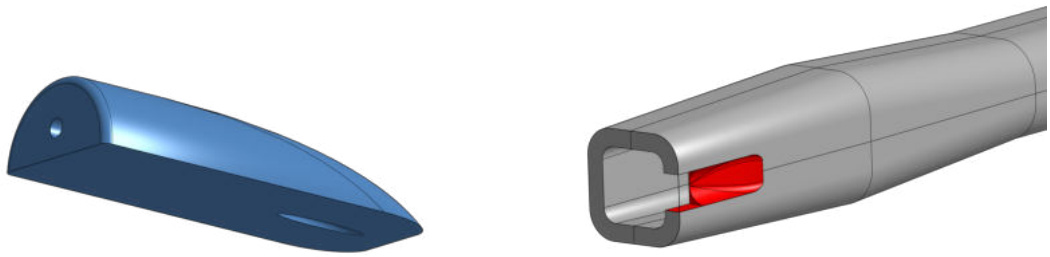

Figure 5.14: Optical fiber support (left) and corresponding slot on the mandrel

Note that the optical fiber support is not aligned with the mandrel base surface in order to allow an eventual finishing operation on the latter and on the stick. Given the curved geometry of the stick, the pre-preg plies would likely tend to wrinkle in the portions of the stick with the largest curvature. For this reason, it has been decided to split the mandrel in two parts, as shown in Figure 5.15, so that, when exposed to the temperatures of the autoclave process, the mandrel tends to expand, pushing the pre-preg plies against the mould surfaces. Special attention has to be paid in order to assure that the fiber does not pass along the conjunction line between the two halves of the mandrel.

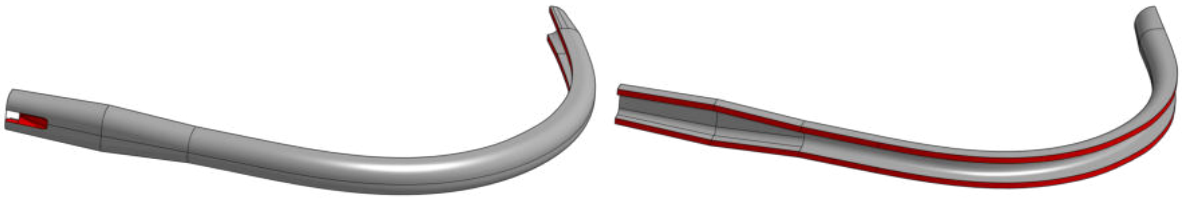

Figure 5.15: CAD of the two halves of the mandrel

To avoid the relative sliding of the two halves of the mandrel and so to guarantee their correct alignment, an alignment system has been designed, consisting on six plug-like spheres, as can be seen in Figure 5.16. The spheres diameter is equal to 2.5 mm, while the corresponding slot is of 2.7 mm diameter.

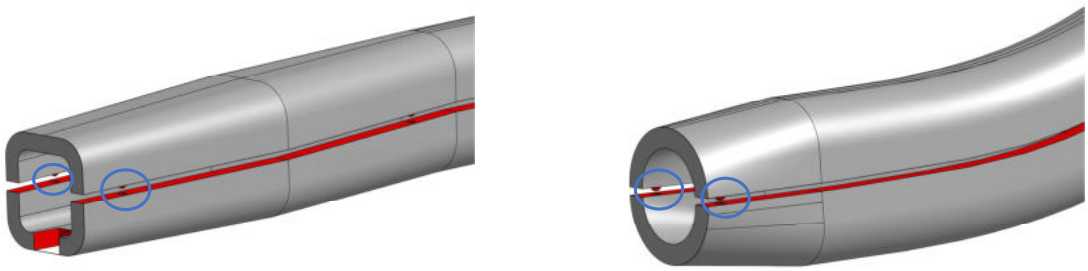

Figure 5.16: Alignment system between the two halves of the mandrel

To allow the connection of the optical fiber to the data acquisition system, a certain quantity of the optical fiber must be available exiting from the support of Figure 5.14. For this reason, a case which permits the winding of the optical fiber has been designed (Figure 5.17). It is needed to protect the optical fiber from being reached by the resin during the autoclave cycle.

Figure 5.17: Optical fiber protection case (front and rear)

A picture of the assembly including the two mandrel halves, the optical fiber support and protection case is reported in Figure 5.18.

Figure 5.18: Final assembly of the mandrel

The optical fiber support, as well as the protection case, are made of ULTEM 1010 resin. It is a high-performance Fused Deposition Modelling (FDM) polyetherimide (PEI) ther-

moplastic. It exhibits high tensile strength in addition to broad chemical resistance and excellent thermal stability. The mandrel is instead printed using the resin ST-130. It is a model material for sacrificial tooling that simplifies the production of hollow composite parts: complex tools can be 3D printed and easily dissolved after curing (the resin withstands the heat and pressure of autoclave curing). The 3D printer used for the realization of the model is the Stratasys Fortus 450mc, reported in Figure 5.19.

Figure 5.19: Stratasys Fortus 450mc 3D printer

A picture of the 3D printed mandrel inside the 3D printer chamber is reported in Figure 5.20.

Figure 5.20: Mandrel inside the 3D printer chamber

Note that the gray parts are the mandrel itself, while the black ones are the support. In particular, it is possible to see that each sphere of the alignment system requires appropriate support structure. Figure 5.21 shows the matching between the two halves of the mandrel.

Figure 5.21: Matching of the two mandrel halves

In Figure 5.22 a detailed view of the mandrel is shown, in which it is possible to see four alignment devices and the slot for the optical fiber support.

Figure 5.22: Detailed view of the alignment devices of the mandrel

5.6. Material characterization

The FE model of the stick, which is treated in Section 6.2, requires the material properties as input. The stick is made of a carbon fiber epoxy-based pre-preg fabric (TC2003T125/M79). Tensile and shear tests on coupons have already been conducted in another thesis work (Ref. [31]). The tests were performed using coupons with the fibers aligned to the tensile force to determine the Young's modulus and the Poisson's ratio. Coupons with the fibers oriented at 45° with respect to the applied force have been used to determine the shear modulus. The tests have been performed using four coupons for the tensile properties and four coupons for the shear properties. The results have been provided as time histories of the axial displacement, axial force and axial deformations. The latter have been measured by an uni-directional strain gauge positioned in one coupon face aligned with the load and by a bi-axial strain gauge positioned in the other coupon face. For each coupon also three measurements of its width and thickness are provided, which are used to compute the average section area of the coupon. To determine the Young's modulus, the σ_x *vs* ε curve for each coupon has been obtained and reported in Figure 5.23 (indicating with x the direction of the applied force and with y the in-plane direction perpendicular to x).

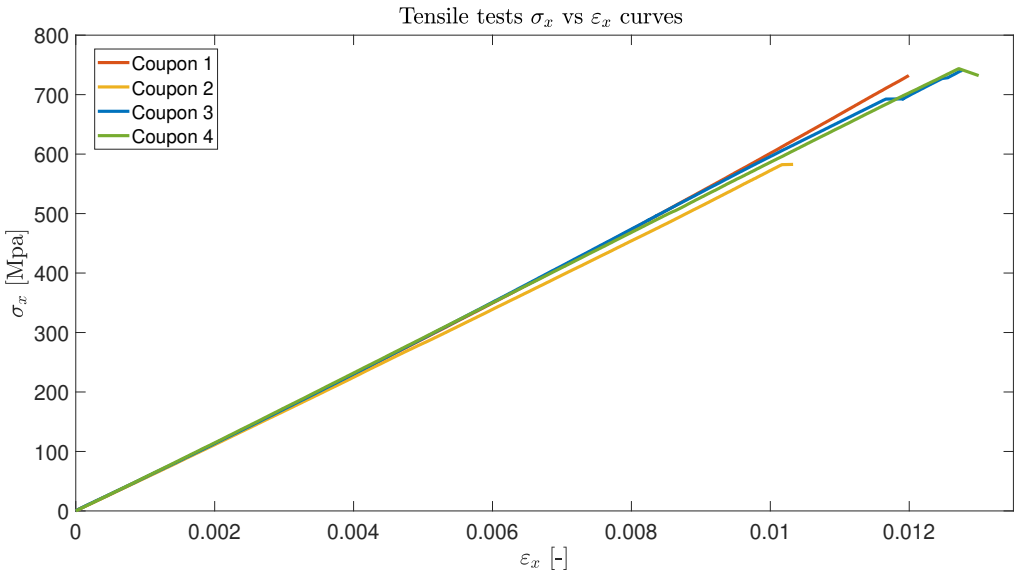

Figure 5.23: Material characterization: σ_x vs ε_x curves for the coupons with the fibers oriented at 0° with respect to the applied force

For the determination of the material tensile properties, the ASTM standard of Ref. [32] is used, which is valid for polymer matrix composite materials reinforced by high-modulus fibers. In particular, the Young's modulus has to be computed as:

$$E = \frac{\Delta\sigma_x}{\Delta\varepsilon_x} \tag{5.9}$$

where:

- $\Delta\varepsilon_x$ is the difference between the two strain points with $\varepsilon = 0.001$ and $\varepsilon = 0.003$ (nominally equal to 0.002);
- $\Delta\sigma_x$ is the difference in applied tensile stress between the two strain points used to compute $\Delta\varepsilon_x$.

This calculation is repeated for each coupon, i.e., for each curve of Figure 5.23, and is averaged between the coupons, obtaining $E_x = 57246\ MPa$. Since the composite pre-preg used is a fabric, the Young's modulus in the direction along the fibers is equal to the one in the direction perpendicular to them, whence $E_x = E_y = 57246\ MPa$. Ref. [32] is used to compute also the Poisson ratio, of which a plot of its trend with respect to the applied force is reported in Figure 5.24. The Poisson's ratio can be computed as:

$$\nu_{xy} = -\frac{\Delta\varepsilon_y}{\Delta\varepsilon_x} \tag{5.10}$$

where:

- $\Delta\varepsilon_x$ is the difference between the two longitudinal strain points with $\varepsilon = 0.001$ and $\varepsilon = 0.003$ (nominally equal to 0.002);
- $\Delta\varepsilon_y$ is the difference in lateral strain between the two longitudinal strain points used to compute $\Delta\varepsilon_x$.

The same averaging procedure used for the Young's modulus is used, obtaining $\nu_{xy} = 0.0298$.

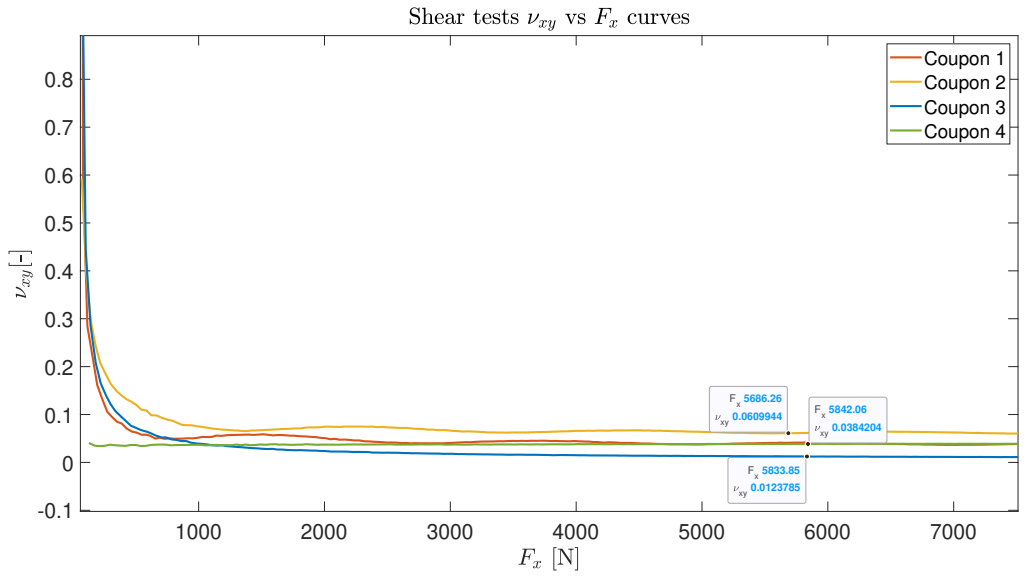

Figure 5.24: Material characterization: ν_{xy} vs F_x curves

For the determination of the shear modulus G_{xy}, the reference is the ASTM standard of Ref.[33], which establishes that:

$$G_{xy} = \frac{\Delta\tau_{xy}}{\Delta\gamma_{xy}} \tag{5.11}$$

where:

- τ_{xy} is the engineering shear stress, computed as:

$$\tau_{xy} = \frac{F_x}{2A} \tag{5.12}$$

  being A the coupon cross section area;

- $\Delta\tau_{xy}$ is the difference in applied engineering shear stress between two shear strain points, starting with the lower strain point in the range of 0.0015 to 0.0025 and using a $0.004 \pm 200\mu\varepsilon$;

- $\Delta\gamma_{xy}$ is the difference between the two engineering shear strain points used to compute $\Delta\tau_{xy}$ (nominally equal to 0.004).

The τ_{xy} *vs* γ_{xy} curves are reported in Figure 5.25.

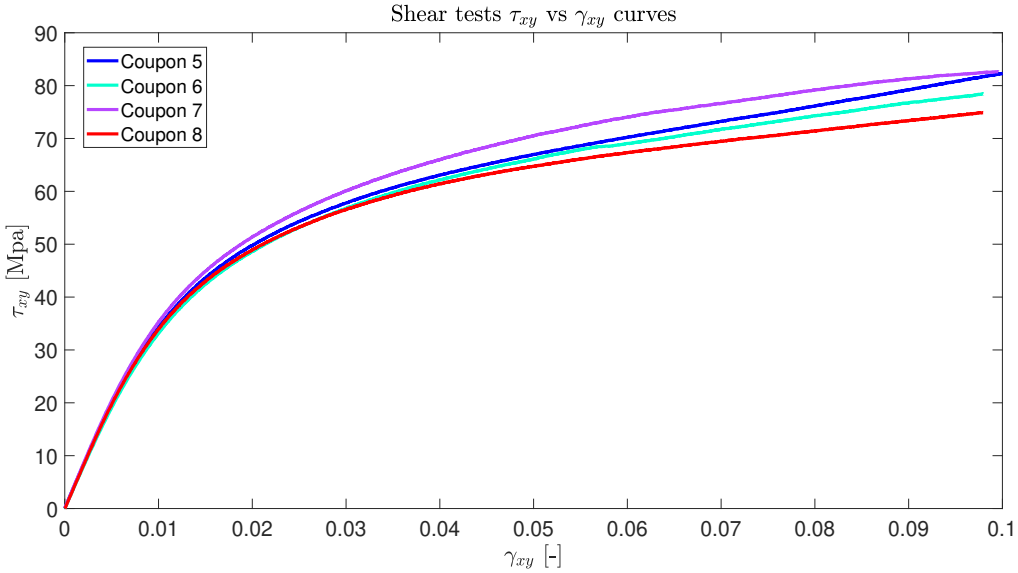

Figure 5.25: Material characterization: τ_{xy} vs γ_{xy} curves

By applying the averaging procedure previously discussed, one obtains $G_{xy} = 3871\ MPa$. For the symmetry of the stiffness matrix, $G_{yx} = G_{xy}$.
The material characteristics are summarized in Table 5.1.

E_x	57246 MPa
E_y	57246 MPa
G_{xy}	3871 MPa
ν_{xy}	0.0298

Table 5.1: Material characteristics

5.7. Plies cutting procedure

Each pre-preg ply must be shaped so that it can be properly wrapped around the mandrel, i.e., each ply must be such that, once placed on the mandrel surface, the match of its edges is obtained. It is thus necessary to perform an accurate 2D development of the plies, for which the software *DesignConcept* by Lectra is used, that is a virtual prototyping and

modeling software widespread in the fashion, automotive and furniture industries alike. It enables a lower error with respect to other software (approximately of the order of 1%). The preliminary step is to create a cutting profile on the CAD of the mandrel to impose the path along which the match of the plies' edges is obtained (Figure 5.26).

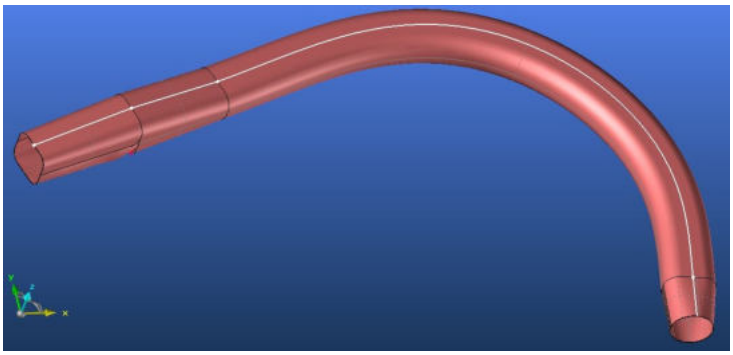

Figure 5.26: Cutting profile on the mandrel surface

The software generates a mesh on the mandrel surface (Figure 5.27). The mesh refinement is chosen to have an adequate compromise between the accuracy of the 2D development and the time required to generate it.

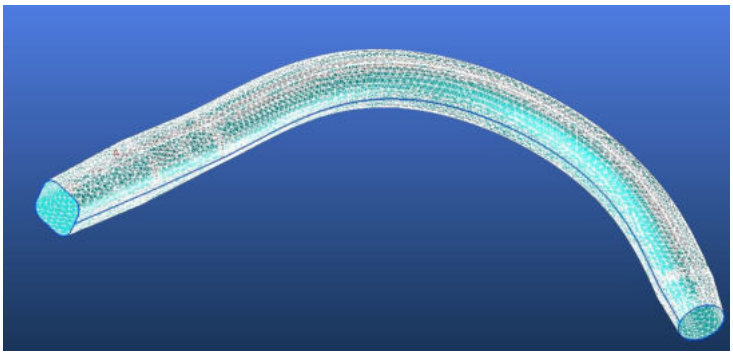

Figure 5.27: Mesh generated on the mandrel surface

An example of the 2D development of the first ply is reported in Figure 5.28

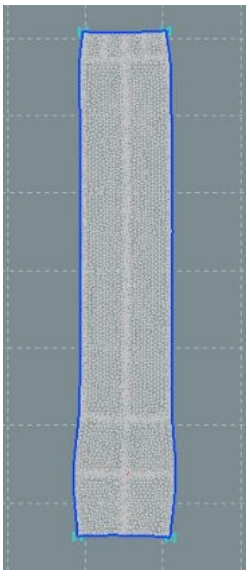

Figure 5.28: 2D development of the first ply

The 2D development, that is a 2D meshed surface, is transformed in a cutting profile. In this passage it is possible to add a seam margin to allow an overlapping of the edges once the ply is wrapped around the mandrel. The same procedure is repeated for the other two plies. To do this, the software asks to give as input the ply nominal thickness, equal to $0.2mm$, to consider the offset between the plies. The software implements the nesting procedure, i.e., it lays out the cutting patterns minimizing the raw material waste. Prior to this, it is possible to impose the direction of the pre-preg fibers to give to the final component the desired stiffness characteristics. The output of the software is a *.dxf* (or *.dwg*) file, which is given as input to the automatic cutting machine, that is the Lectra Vector FX TechTex, of which a picture is reported in Figure 5.29.

Figure 5.29: Lectra Vector FX TechTex automatic cutting machine

The cutting machine basically uses vacuum to hold in place the pre-preg layer in the cutting area. To achieve this, another ply is needed above the pre-preg, that is a sealing film to permit to maintain vacuum. Among the others, a significant advantage from the technological point of view is the fact that the automatic cutting machine does not require cutting templates.

5.8. Stick first prototype realization

Prior to the start of the manufacturing process, it is required to perform the mould's surface preparation, in particular by arranging several layers of:

1. cleaner, to remove old release agents (including chemical release agents and wax), dirt, grease and other contaminants from the mould's surface, without damaging the mould;
2. sealant (or pore filler), to seal micro-porosities and condition the raw bonding sites found on virtually all mould substrates;
3. release agent, to ensure adequate lubricity and non-sticking properties to the mould; it protects the mould surface from resins and other highly abrasive raw materials.

The stick realization is performed following the deposition sequence reported in Figure 5.30. The mandrel (3) is covered by a teflon layer to facilitate the detachment of the first pre-preg layer (5.1). Note that both (4) and (5.1) follow the path of the slot on the mandrel for the optical fiber support (7). Between the first pre-preg layer (5.1) and the second one (5.2) is embedded the optical fiber (6), which enters the support and is wrapped on the housing. The last (third) pre-preg layer (5.3) is in contact with the mould surface (8). The mould is enclosed in the vacuum bag (10), again with a breather layer (9) with the function of catching the eventual resin spills. A breather layer (2) is used also inside the mandrel with the same function. The innermost layer consists of a tubular bag (1) which, as consequence of the pressure inside it during the autoclave process, pushes the mandrel (the two halves of it) against the mould surface, enhancing the compaction procedure of the pre-preg plies. As can be seen in Figure 5.30, on the external surface of the vacuum bag acts the autoclave pressure (p_{ext}), on the surface of the tubular bag acts the pressure p_{int}, which is the pressure inside the cavities of the mould. On the interfaces vacuum bag (9) - mould (6) and tubular bag (1) - breather layer (2), instead, acts the pressure generated by vacuum (p_{vac}).

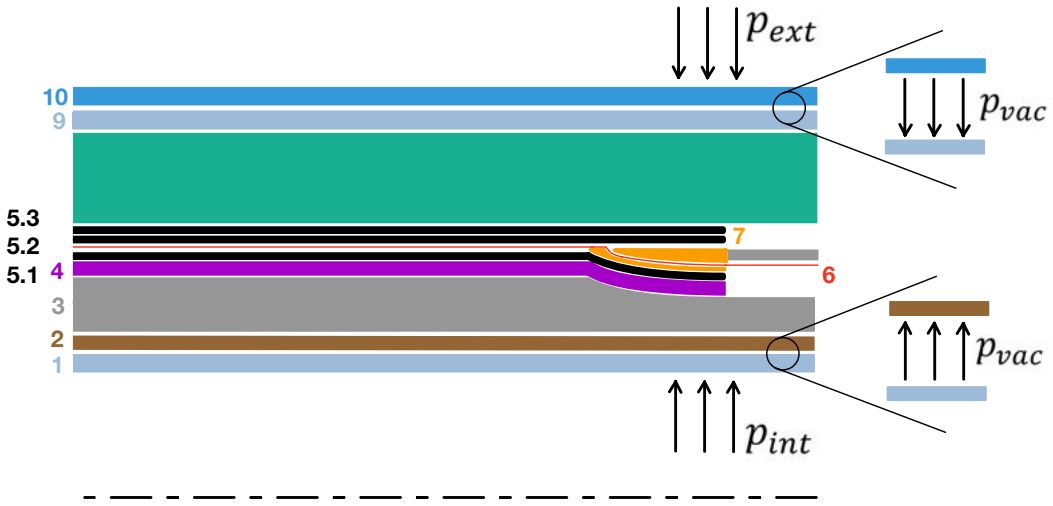

Figure 5.30: Deposition sequence for the stick realization

The main steps of the stick practical realization process are reported hereunder:

- Figure 5.31 shows the six layers obtained from the pre-preg sheet; note that their reddish color is due to the presence of a protective layer;

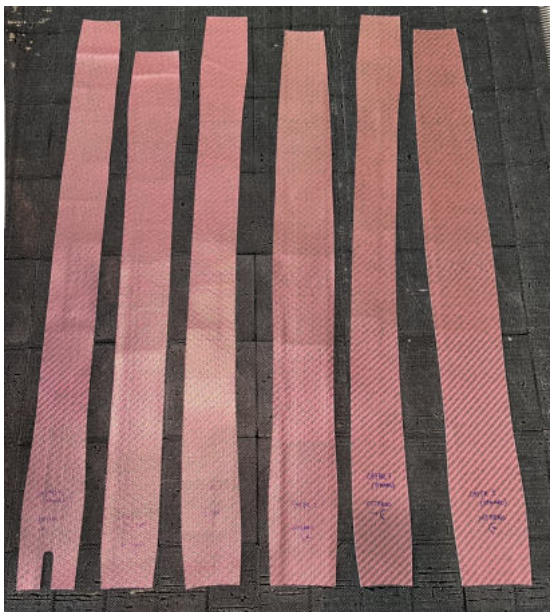

Figure 5.31: Pre-preg layers cut

- Figure 5.32 shows the first step of the realization process, that is the disposition of the tubular bag inside the cavity of the mandrel and of the breather layer that surrounds the tubular bag;

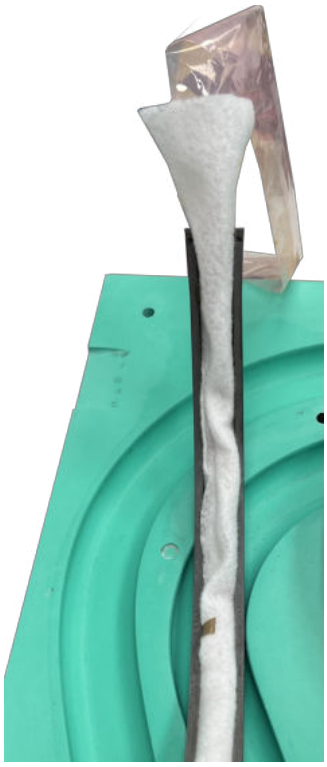

Figure 5.32: Tubular bag and breather layer inside the mandrel cavity

- Figure 5.33 shows the mandrel closed by some tape, in which is possible to see the tubular bag and the breather layer coming out from it;

Figure 5.33: Mandrel closed with some tape

- Figure 5.34 shows the mandrel with the teflon layer on its external surface;

Figure 5.34: Mandrel with the teflon layer

- Figure 5.35 shows the mandrel after the deposition of the first pre-preg ply (i.e., of the first two halves forming the first layer); the pre-preg layers are arranged up so that the carbon fibers are aligned with the stick medium line; the lay-up process is performed inside the clean room available at the Department of Aerospace Science and Technology of Politecnico di Milano;

Figure 5.35: First pre-preg ply wrapped around the mandrel

- Figure 5.36 shows the optical fiber embedded after the first pre-preg ply; it is arranged throughout the mandrel length and it enters the optical fiber support (yellow component);

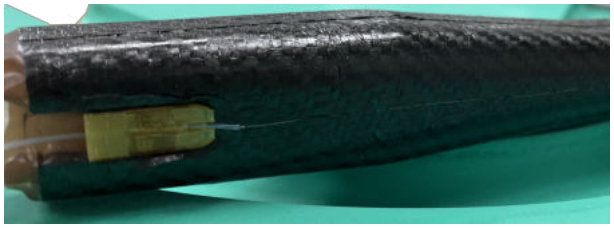

Figure 5.36: Particular of the optical fiber embedded after the first pre-preg ply

- Figure 5.37 shows the wrapping procedure of one pre-preg semi-ply; note the difficulty of this passage on the curved parts of the mandrel;

Figure 5.37: Particular of the wrapping procedure on the curved part of the mandrel

- Figure 5.38 shows the mandrel covered with the three pre-preg plies and disposed on the mould; it is possible to see the two thermocouples used for the autoclave cycle: one is placed inside the mandrel and the other one on the other mould cavity (that is for the realization of another helicopter stick);

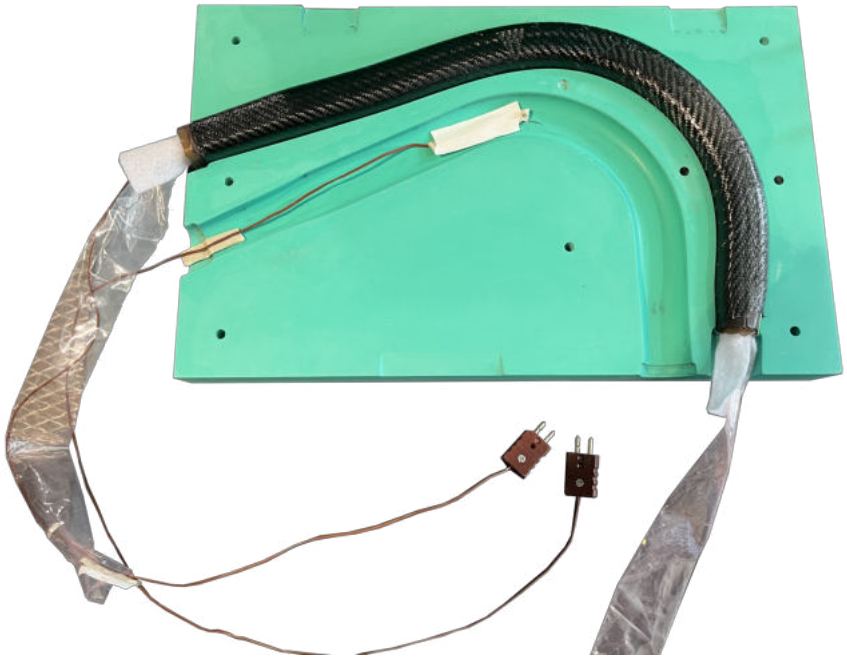

Figure 5.38: Stick before the autoclave process

- Figure 5.39 shows the vacuum bag containing the mould ready to be inserted in the autoclave; two vacuum valves are used and in correspondence of them the breather layer is reinforced to prevent the action of the vacuum from damaging the mould as a consequence of the valve-mould contact;

Figure 5.39: Vacuum bag

- Figure 5.40 shows the vacuum bag placed inside the autoclave with the vacuum valves and the thermocouples connected to the autoclave;

Figure 5.40: Vacuum bag inside the autoclave room

- Figure 5.41 shows the stick after the autoclave cycle, with the optical fiber support and housing removed;

Figure 5.41: Stick after the autoclave cycle

- Figure 5.42 shows the stick inside the oven for the mandrel dissolution process. The mandrel is filled with a solution of sodium hydroxide. The oven temperature is set to 90° and the time needed for the process depends on the 3D printed part thickness. This process did not work for the stick first prototype: the mandrel revealed to be too resistant to the sodium hydroxide solution. In Section 5.9 is reported the solution to this problem adopted for the second prototype realization. Regarding the possible problematic aspects of the contact between the epoxy resin and the sodium hydroxide solution, *engineeringtoolbox* reports that epoxy resin is resistant to sodium hydroxide solutions with a concentration up to 50% and at temperatures up to 50°. Since the oven temperature is higher than 50°, an analysis of the effects of the sodium hydroxide on the epoxy resin should be conducted.

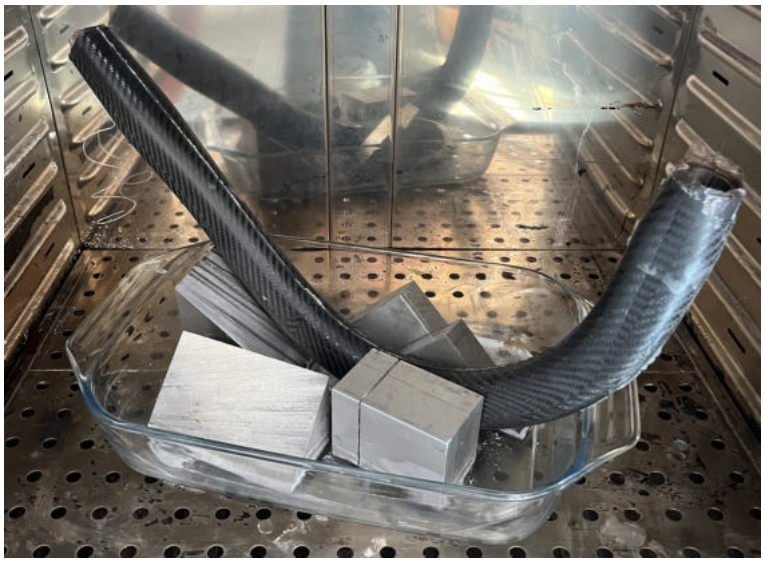

Figure 5.42: Stick in the oven for the mandrel dissolution process

5.9. Stick second prototype realization

The first stick prototype presented four issues:

1. the failure of the mandrel dissolution process;
2. at the start of the autoclave cycle, the heating of the mould (measured by the thermocouple placed in its the empty cavity) took a long time (3-4 hours) due to the high thermal inertia of the polyurethane;
3. during the autoclave cycle, the autoclave pressure caused a portion of the vacuum bag to be sucked inside the empty mould cavity (that is for the realization of another helicopter stick);
4. during the autoclave cycle, the optical fiber housing of Figure 5.17 shifted a little from its nominal position, causing the optical fiber to break;

To cope with the first problem, the 3D printer settings have been changed so that the mandrel external shape is equal to the one of the first prototype but the internal pattern is different: as can be seen in Figure 5.43, the mandrel is almost hollow. This entails a reduction of the mandrel robustness which, while making the support removal process more difficult, allows to perform the dissolution and consequent removal of the mandrel.

Figure 5.43: 3D printer pattern on the mandrel internal

Despite these precautions, the mandrel solving process was not successful. Since its structural contribution can be considered negligible, this stick prototype was nonetheless used for the following steps. The second and third issues have been solved in one shot by placing a tubular bag inside the empty mould cavity, as shown in Figure 5.44.

Figure 5.44: Tubular bag inside the mould empty cavity to solve the problem encountered during the autoclave cycle of the first stick prototype

Since the tubular bag is inflated by the autoclave pressure, it prevents the vacuum bag to be sucked inside the cavity. Moreover, since the autoclave air flows inside the tubular

bag, the latter helps in the heating process of the mould, speeding it up. The fourth issue has been fixed by printing the optical fiber housing of Figure 5.17 joined to one of the two mandrel halves. This allows also to avoid the realization of the alignment devices for the two mandrel halves, saving the 3D printer support for their realization.

6 | Stick load identification

One of the fundamental steps in the development and setting up of a measuring instrument is the calibration process. In the case of interest, it consists on the calibration of the optical fiber sensors of stick second prototype. A summary scheme of the calibration process is reported in Figure 6.1: the stick will be instrumented with some strain gauges, which readings will be compared to the ones coming from a FE model of the test setup. If the comparison is not successful, an update of the FE will be required, otherwise the latter can be considered correlated. The FE model is used to perform the optimization of the FBG sensors positioning. Experimental tests on the stick containing the sensors are performed by applying known loads and by reading the sensors measurement, obtaining the experimental influence coefficients matrix.

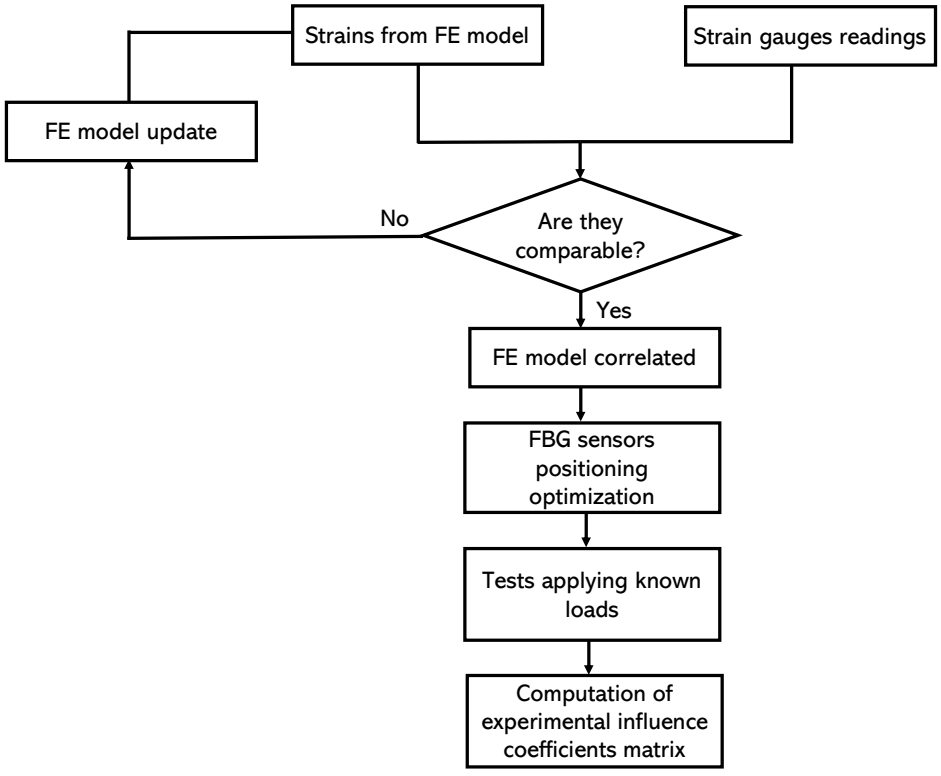

Figure 6.1: Calibration process summary scheme

6.1. Stick calibration setup

The cyclic inceptor is subjected to longitudinal forces, to lateral ones and to any combination of them. The calibration process consists on the reproduction of these loading conditions and to do that the stick is clamped to a wall, as can be seen in Figure 6.2, in which the stick is positioned to perform the lateral force calibration.

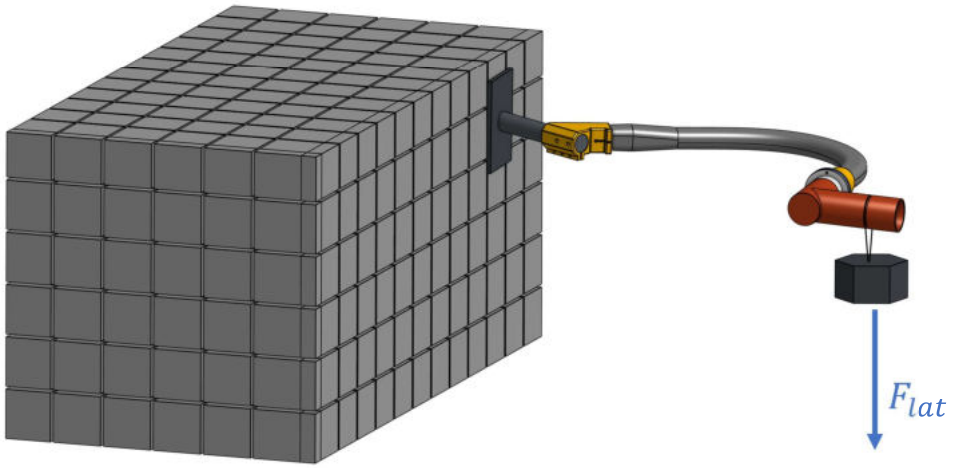

Figure 6.2: Test setup for the stick sensor calibration for the lateral force

In particular, the stick is attached, through a 3D printed connector, to a circular bar, which is welded to a flat plane, which in turn is constrained to the wall. It has been decided to use a dummy grip to simplify the application of the load: instead of using the real ergonomics, an *L-shaped* grip has been purposely 3D printed. It presents a groove to wrap around a row without the sliding of it, to which it is suspended a weight of known mass. The groove is positioned in correspondence of the so-called *third finger reference point*, which is the point in which a medium pilot puts his third finger, considered as the point in which the equivalent concentrated load can be placed. A picture of the 3D printed grip and of the stick-wall connection element is reported in Figure 6.3. The 3D printer used in this case is the Formlabs Form 3L and the resin used is the Formlabs *Tough 2000* (technical sheet in Ref. [34]), which guarantees good mechanical properties (e.g., ultimate tensile strength of 46 Mpa, tensile modulus of 2.2 GPa), ensuring that the 3D printed elements will not bend when subjected to the loads of interest.

Figure 6.3: 3D printed grip for the load application (left) and stick-wall connection element (right)

To test the pure longitudinal force loading condition, since the load is applied by exploiting gravity, the stick geometry leads to the necessity to use an *ad hoc* setup. In particular, referring to Figure 6.4, the circular bar needs to be welded to the plate with an angle α with respect to the wall. A picture of the circular bar is reported in Figure 6.5.

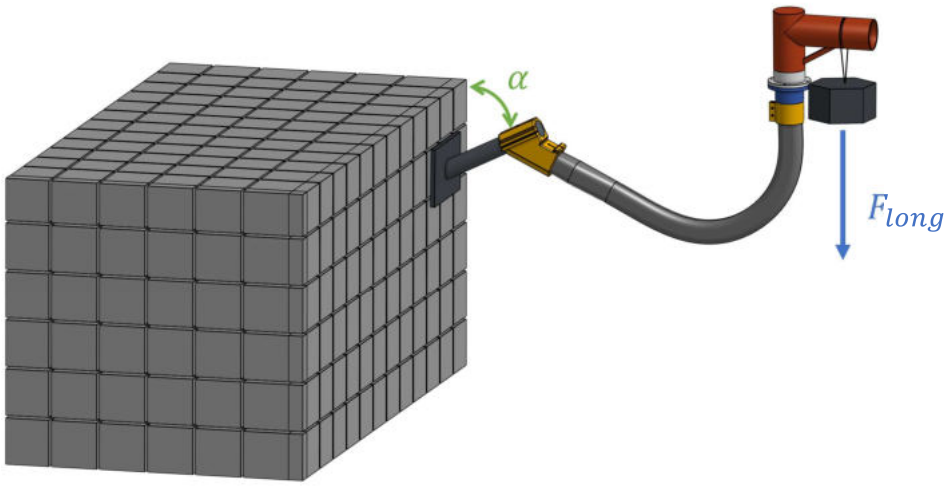

Figure 6.4: Test setup for the stick sensor calibration for the longitudinal force

Figure 6.5: Test setup for the stick sensor calibration for the lateral force

The angle α is obtained such that by simply rotating the stick around the circular bar all the forces applied with the masses would be a linear combination of F_{long} and F_{lat} laying in the plane perpendicular to the grip axis.

6.2. Finite element model

The FE model of the test setup has been developed, allowing to optimize the position of the FBG sensors for the load monitoring. It could be used also to verify that the stress to which the stick is subjected is lower than the ultimate one. As a matter of fact, even though the forces introduced by the pilot are well below the stick structural limits, this verification would be needed if the aim was of making the control inceptor flyable (i.e., certifiable). Not least, the FE model enables to conduct a sensitivity analysis, for example to understand the insensitivity of the stick to changes of loads both in terms of magnitude and orientation. The software used for the FE model is *Simulia/Abaqus*. The starting point for the FE model is the CAD geometry of the stick. The first step is the generation of the mesh, for which 4-nodes shell elements of 3 mm medium size are used. They are suitable for thin-walled structures, since the shell elements are characterized by a plane stress state. A view of the meshed stick is reported in Figure 6.6.

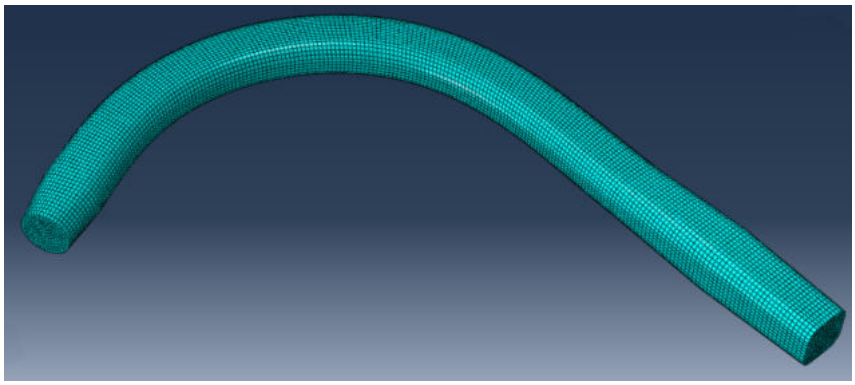

Figure 6.6: Mesh generated on the stick

The material is defined, using the characteristics computed on Section 5.6, and subsequently the material orientation is assigned. In particular, it is necessary to define three reference systems: one cylindrical for the curved part of the stick and two linear for the straight parts of the stick. The reference systems are chosen such that the x-axis follows the stick medium line, i.e., the direction of the carbon fibers. In Figure 6.7 is reported a view of the material orientation on the stick: the x-axis of the reference system of each element follows the medium line of the stick.

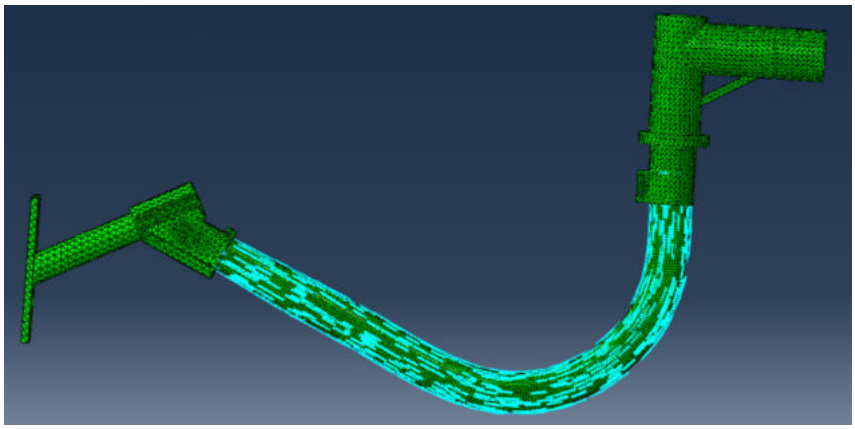

Figure 6.7: x-axis material orientation on the stick

The final assembly is reported in Figure 6.8, which includes the plate with the inclined tube to constrain the stick to the wall, the connection part between the stick and the tube, the grip for the load application and the connection part between the stick and the grip. Other than this, it is possible to see the cutting planes used to divide the curved part of the stick from the straight ones (to obtain a more regular mesh), the global reference system (on the left) and the other three local reference systems for the material orientation. Also, it is possible to see the two reference points, that are used for the load

application (the one on the right) and to clamp the plate to the wall (the one on the left). All the parts different from the stick are considered rigid, even though they are not, since the purpose of the tests is not the calibration of the stick stiffness.

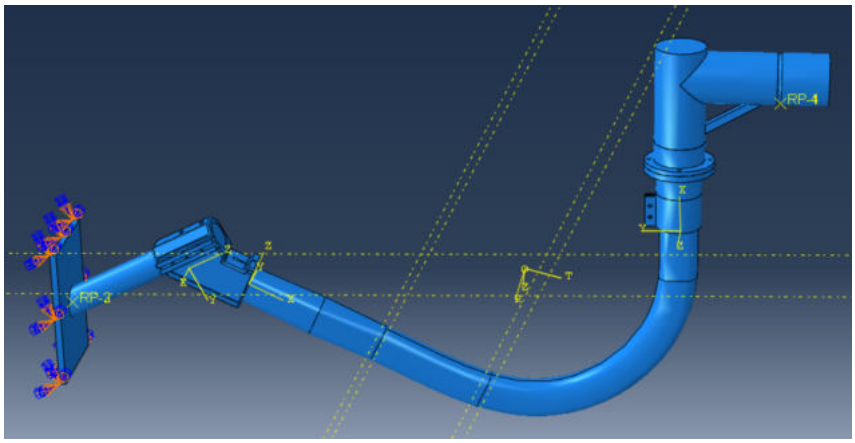

Figure 6.8: Final assembly of the calibration test setup

Performing a linear static analysis, the deformed shape with the relative contour plot of the displacement consequent to the application of a lateral force equal to $F_{lat} = 100\ N$ (see Figure 6.2) is reported in Figure 6.9. The deformed shape is superimposed with the undeformed one (the white one). The same plot relative to the application of a longitudinal force $F_{long} = 100\ N$ (see Figure 6.4) is reported in Figure 6.10.

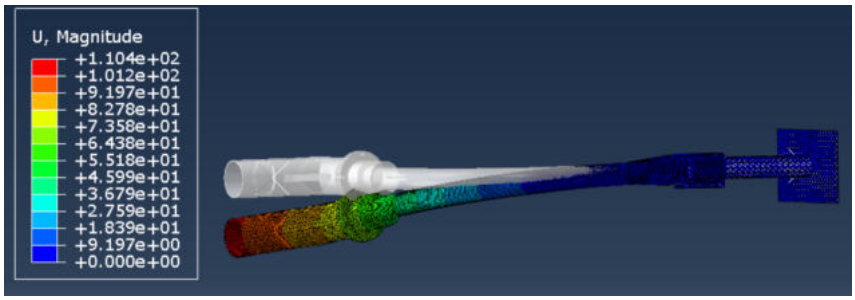

Figure 6.9: Deformed shape and relative displacement (in mm) contour plot with the application of a lateral force on the stick

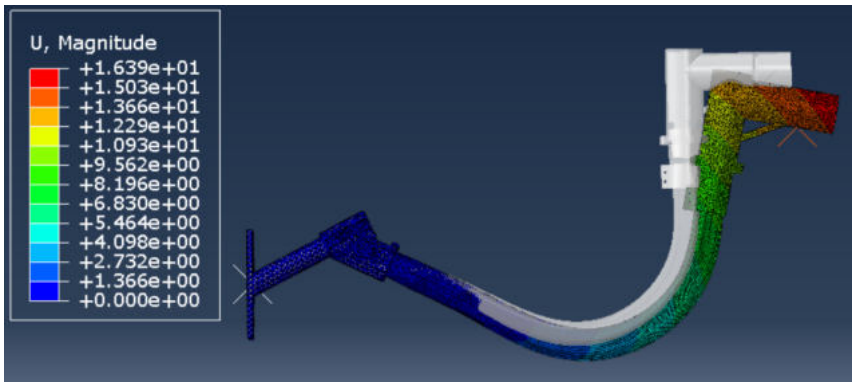

Figure 6.10: Deformed shape and relative displacement (in mm) contour plot with the application of a longitudinal force on the stick

6.3. Stick strain gauges positioning

The FE model has been exploited also to decide the optimal position of the strain gauges on the stick. In particular, they should be placed on the regions in which the deformation magnitude is large and its gradient is low. A plot of the in-plane deformation component along the carbon fibers (ε_{xx}) for the lateral force loading condition is reported in Figure 6.11. From these results, it has been decided to place a strain gauge (strain gauge 1) on the blue region of Figure 6.11, aligned with the local carbon fibers x-direction, which measure the deformations generated by the bending moment.

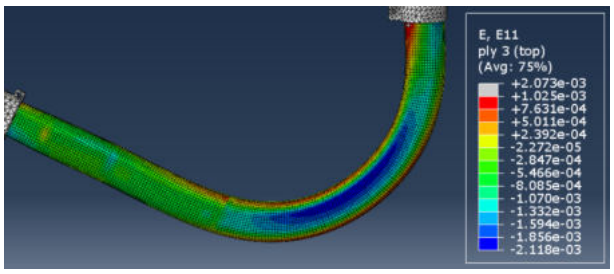

Figure 6.11: In-plane deformation along the carbon fibers x-direction for the lateral force loading condition

Considering the same component of deformation (ε_{xx}) for the longitudinal force loading condition, the result is reported in Figure 6.12. It has been decided to put a strain gauge (strain gauge 2) on the orange region, again aligned with the local carbon fiber x-direction.

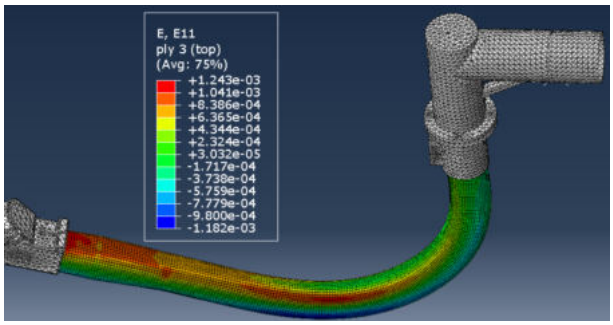

Figure 6.12: In-plane deformation along the carbon fibers x-direction for the longitudinal force loading condition

The FE model analysis results show that the lateral force loading condition generates a non-negligible shear deformation (γ_{xy}), as reported in Figure 6.13.

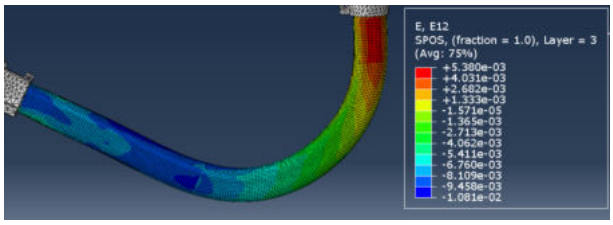

Figure 6.13: Shear deformation for the lateral force loading condition

For this reason, it has been decided to place, on the blue region of Figure 6.13, two strain gauges (strain gauges 3, 4) oriented at ±45° with respect to the carbon fiber direction, which measure the deformation induced by the torque. Figure 6.14 shows the strain gauges final setup.

Figure 6.14: Strain gauges final setup

In Figure 6.15 is reported a detailed view of one single strain gauge and of the two strain gauges positioned at ±45°.

Figure 6.15: Detailed view of the strain gauges

Each of the four strain gauges is connected to the strain indicator and recorder of Figure 6.16.

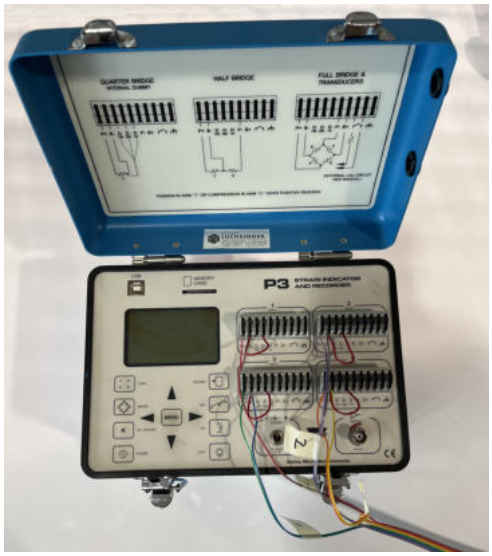

Figure 6.16: Strain indicator and recorder

6.4. Preliminary load identification with strain gauges

A preliminary load identification is carried out performing tests with the strain gauges on the stick, consisting on the application of known loads to the stick in the pure lateral/longitudinal force configuration (Figure 6.17) and in the measure of the corresponding strain gauges output ($\mu\varepsilon$).

Figure 6.17: Pure lateral (left) and longitudinal (right) load application

Making the hypothesis of linearity, the relationship between the strain gauge output and the applied loads can be expressed as:

$$\boldsymbol{\epsilon} = \mathbf{KP} \tag{6.1}$$

where:

- $\boldsymbol{\epsilon} = \begin{Bmatrix} \varepsilon_1 \\ \varepsilon_2 \\ \varepsilon_3 \\ \varepsilon_4 \end{Bmatrix}$ is the vector containing the four strain gauges outputs for the considered loading condition;
- $\mathbf{K} = \begin{bmatrix} \alpha_{11} & \alpha_{12} \\ \alpha_{21} & \alpha_{22} \\ \alpha_{31} & \alpha_{32} \\ \alpha_{41} & \alpha_{42} \end{bmatrix}$ is the matrix of the *influence coefficients*;
- $\mathbf{P} = \begin{Bmatrix} F_{lat} \\ F_{long} \end{Bmatrix}$ is the vector containing the applied loads.

By applying a pure lateral force of 9.81N the results are:

$$\mathbf{P} = \begin{Bmatrix} F_{lat} = 9.81N \\ F_{long} = 0\ N \end{Bmatrix} \rightarrow \boldsymbol{\epsilon}_{\boldsymbol{F_{lat}}} = \begin{Bmatrix} 80 \\ -4 \\ 0 \\ 8 \end{Bmatrix} [\mu\varepsilon] \tag{6.2}$$

and the influence coefficients can be computed as (Ref. [35]):

$$\begin{Bmatrix} \alpha_{11} \\ \alpha_{21} \\ \alpha_{31} \\ \alpha_{41} \end{Bmatrix} = \boldsymbol{\epsilon}_{\boldsymbol{F_{lat}}}/F_{lat} \tag{6.3}$$

Similarly, by applying a pure longitudinal force of 9.81N the results are:

$$\mathbf{P} = \begin{Bmatrix} F_{lat} = 0\ N \\ F_{long} = 9.81N \end{Bmatrix} \rightarrow \boldsymbol{\epsilon}_{\boldsymbol{F_{long}}} = \begin{Bmatrix} 36 \\ -48 \\ 306 \\ -290 \end{Bmatrix} [\mu\varepsilon] \tag{6.4}$$

and the influence coefficients can be computed as:

$$\begin{Bmatrix} \alpha_{12} \\ \alpha_{22} \\ \alpha_{32} \\ \alpha_{42} \end{Bmatrix} = \boldsymbol{\epsilon}_{\boldsymbol{F_{long}}}/F_{long} \tag{6.5}$$

In the (real) case, the load ($\mathbf{P}$) is unknown and can be retrieved from Equation 6.24, since $\boldsymbol{\epsilon}$ is read on the strain indicator and $\mathbf{K}$ is known from the calibration process. However, $\mathbf{K}$ is in general not invertible (being a rectangular matrix), hence the least square method has to be employed. It consists on pre-multiplying Equation 6.24 by $\mathbf{K}^T$:

$$\mathbf{K}^T\boldsymbol{\epsilon} = \mathbf{K}^T\mathbf{K}\mathbf{P} \tag{6.6}$$

from which is possible to compute $\mathbf{P}$ as:

$$\begin{aligned} \mathbf{P} &= (\mathbf{K}^T\mathbf{K})^{-1}\mathbf{K}^T\boldsymbol{\epsilon} \\ &= \mathbf{K}^+\boldsymbol{\epsilon} \end{aligned} \tag{6.7}$$

being $\boldsymbol{K}^+$ the Moore–Penrose inverse of $\boldsymbol{K}$. The results reported in Equation 6.2 and in Equation 6.4 are averaged over several tests. The same tests are repeated with increasing values of the applied force to verify the linearity of the strain gauges outputs. Figure 6.18 shows that all the strain gauges output is linear as the force magnitude increases. The linearity reference is obtained starting from the first point of each plot.

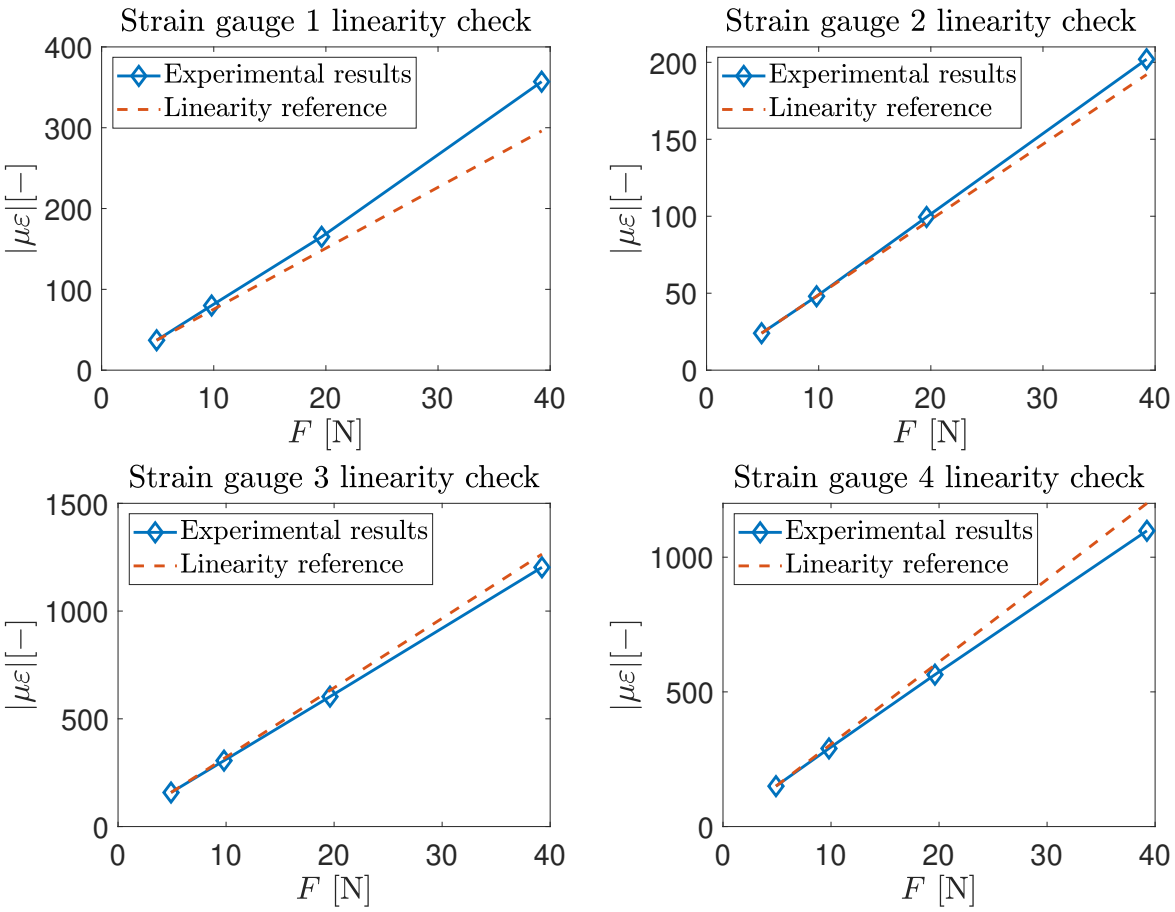

Figure 6.18: Strain gauges linearity check

In particular, the linearity is well verified for the first three tests (corresponding to the application of known masses of 0.5 kg, 1 kg, 2 kg), so the final $\mathbf{K}$ matrix is computed by averaging the results of these three tests:

$$\mathbf{K} = mean(\mathbf{K_{0.5kg}}, \mathbf{K_{1kg}}, \mathbf{K_{2kg}}) \tag{6.8}$$

The matrix of influence coefficients results to be:

$$\mathbf{K} = \begin{bmatrix} \alpha_{11} & \alpha_{12} \\ \alpha_{21} & \alpha_{22} \\ \alpha_{31} & \alpha_{32} \\ \alpha_{41} & \alpha_{42} \end{bmatrix} = \begin{bmatrix} 3.5009 & 8.3015 \\ -5.0013 & 0.1784 \\ 31.1990 & 0.2548 \\ -29.2176 & 0.6817 \end{bmatrix} [\mu\varepsilon/N] \tag{6.9}$$

A validation procedure is hereinafter presented, consisting in the application of known loads to the stick in a general loading condition, i.e., in a condition in which a combination

of F_{long} and F_{lat} is applied (Figure 6.19) and in the measure of the corresponding strain gauges outputs ($\mu\varepsilon$). This procedure represents a preliminary validation process: the loads applied to the stick are instead identified in the stick prototype with the FBG sensors. With reference to Figure 6.19, this test is repeated three times, using $\theta = 30°$, 45°, 60°.

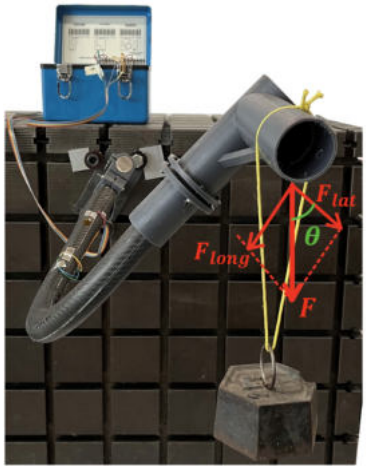

Figure 6.19: Validation process setup

An inclinometer is used to assure that the correct angle is used. It has to be verified that the values of the known applied loads:

$$\mathbf{P_{known}} = \begin{Bmatrix} F_{long,\ known} \\ F_{lat,\ known} \end{Bmatrix} = \begin{Bmatrix} F\sin(\theta) \\ F\cos(\theta) \end{Bmatrix} \tag{6.10}$$

coincide with the ones computed as:

$$\mathbf{P_{computed}} = \begin{Bmatrix} F_{long,\ computed} \\ F_{lat,\ computed} \end{Bmatrix} = \mathbf{K^{-1}}\boldsymbol{\epsilon} \tag{6.11}$$

where $\boldsymbol{\epsilon}$ are the readings of the strain gauges. The errors between the known and computed loads are:

$$e_{F_{long}} = \frac{|F_{long,\ computed} - F_{long,\ known}|}{||\mathbf{P_{computed}}||} \cdot 100 \tag{6.12}$$

$$e_{F_{lat}} = \frac{|F_{lat,\ computed} - F_{lat,\ known}|}{||\mathbf{P_{computed}}||} \cdot 100 \tag{6.13}$$

The validation process is performed using a mass of 1 kg and 2 kg, leading to the results respectively of Table 6.6 and Table 6.7.

θ	$\mathbf{e_{F_{long}}}$ [%]	$\mathbf{e_{F_{lat}}}$ [%]
30°	16.17	3.88
45°	11.70	8.41
60°	3.03	10.32

Table 6.1: Validation process results using a mass of 1 kg

θ	$\mathbf{e_{F_{long}}}$ [%]	$\mathbf{e_{F_{lat}}}$ [%]
30°	3.06	8.42
45°	12.27	10.14
60°	0.33	11.26

Table 6.2: Validation process results using a mass of 2 kg

Apart from the error on the longitudinal force with the mass of 1 kg, all the errors are lower than 13%. Being a preliminary load identification procedure, the results can be considered acceptable.

6.5. Correlation with the FE model

It is possible to make a comparison between the FE model results and the experimental ones. This allows to correct the FE model so that the subsequent optimization procedure for the FBG sensors positioning can be carried out with a model that is more faithful to reality. The errors between the FE model results and the strain gauges readings are reported in Table 6.3. In particular, in the longitudinal force loading condition only the strain gauge 1 reading is relevant, while for the lateral force loading condition only the ones of the strain gauges 2, 3, 4 are significant.

Strain gauge 1, F_{long} [%]	7.29
Strain gauge 2, F_{lat} [%]	156.00
Strain gauge 3, F_{lat} [%]	23.20
Strain gauge 4, F_{lat} [%]	16.75

Table 6.3: Strain components error between FE model and strain gauges readings

The correlation for the strain gauges 1, 3, 4 is good, but this is not valid for the strain gauge 2. This is due to the wrong placement of this strain gauge: it probably stands in correspondence of an overlapping region between two semi-plies. To account for that, the FE model has been updated, adding a ply on the regions highlighted in Figure 6.20, which therefore are composed by four plies.

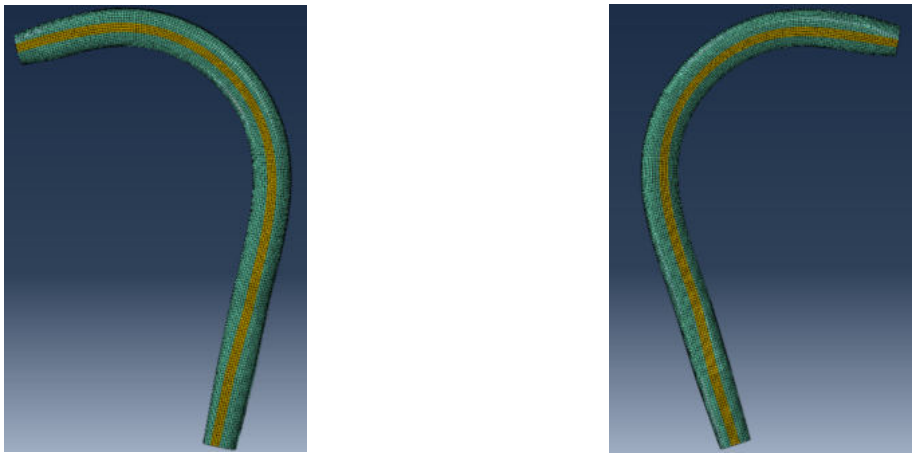

Figure 6.20: Stick regions in which a ply has been added on the FE model

Nevertheless, the result obtained for the strain gauge 2 was still not well correlated with the FE model. To improve this results, the *normalization theory* has been used (Ref. [36]). It stems from the fact that composite materials mechanical properties that are dominated by the properties of the reinforcing fiber are dependent on the volume fraction of fiber in the laminate. Two factors can cause laminate fiber volume fraction to vary:

1. the amount of matrix resin present relative to the amount of fiber (resin content);
2. the amount of porosity (void volume).

These factors give rise to changes in fiber volume fraction from material to material, batch to batch, panel to panel, and even specimen to specimen within a panel. In particular, it has been assumed that, in the region of interest for the strain gauge 2, the amount of resin that flowed out was lower than the correct one, resulting in a lower Young's modulus of the material. Since, in theory, fiber-dominated strength and stiffness properties vary linearly with fiber volume fraction, it is possible to compute the *normalized* Young's modulus ($E_{x,normalized}$) for the region of interest as:

$$E_{x,normalized} = E_{x,nominal} \frac{t_{nominal}}{t_{real}} \tag{6.14}$$

where:

- $E_{x,nominal}$ is the nominal Young's modulus, equal to 57246 MPa;
- $t_{nominal}$ is the nominal laminate thickness, equal to $4 \cdot 0.2\ mm = 0.8\ mm$;
- t_{real} is the real laminate thickness; since it has been assumed that there is an excess amount of resin, the real laminate thickness has been considered equal to $4 \cdot 0.25\ mm = 1.00\ mm$.

Using Equation 6.14 and the data just reported, one obtains $E_{x,normalized} = 45796\ MPa$. The resulting errors are reported in Table 6.4.

Strain gauge 1, F_{long} [%]	5.97
Strain gauge 2, F_{lat} [%]	24.43
Strain gauge 3, F_{lat} [%]	0.98
Strain gauge 4, F_{lat} [%]	−4.48

Table 6.4: Strain components error between FE model and strain gauges readings after the normalization theory application

Even though the error on the strain gauge 2 is still high, the results are accepted and they suggest to avoid the regions of overlapping of the pre-preg layers for the FBG sensors positioning. The results for the other strain gauges are acceptable, so it is possible to proceed with the optimization process reported in Section 6.6.

6.6. Genetic algorithm for the stick sensors position optimization

The FBG sensors position has to be such to allow a correct identification of the loads applied to the stick. The critical point is the fact that the matrix $\mathbf{K}$ of Equation 6.24 is generally ill-conditioned, i.e., $cond(\mathbf{K}) >> 1$ (Ref. [35]). The optimization process for the sensors positioning is carried out in a portion of the stick, defining a subset of elements in the FE model, that is shown in Figure 6.21.

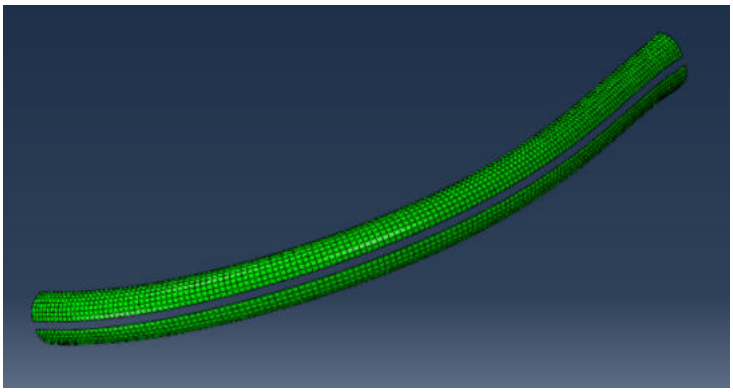

Figure 6.21: Stick surface region for the sensor positioning optimization process

In particular, it is possible to observe that half of the curved part of the stick (referring to Figure 5.21, the curved part of the right half of the mandrel) has been excluded due to the difficulty of performing a smooth lay up of the pre-preg in that region. This is due to the fact that a surface irregularity rather that a wrinkle could invalidate the sensors reading. Moreover, the region close to the mould closing is not optimal for the sensors positioning, hence it has been excluded in the remaining surface. Each element of the FE model is assimilated to a FBG sensor: one of the outputs of the optimization process is the identification number of the elements related to the FE model, which defines the position of the sensors. For each element of the optimization surface of Figure 6.21 the deformation components ε_{11}, ε_{22} and γ_{12} have been retrieved from the FE model. This is repeated for both the loading conditions (F_{long}, F_{lat}) and the deformation components of each element are arranged as the rows of the following matrices, together with the corresponding element ID:

$$\boldsymbol{\epsilon_{F_{long}}} = \begin{bmatrix} ID_1 & \varepsilon_{11,1_{F_{long}}} & \varepsilon_{22,1_{F_{long}}} & \gamma_{12,1_{F_{long}}} \\ ID_2 & \varepsilon_{11,2_{F_{long}}} & \varepsilon_{22,2_{F_{long}}} & \gamma_{12,2_{F_{long}}} \\ \vdots & \vdots & \vdots & \vdots \\ ID_n & \varepsilon_{11,n_{F_{long}}} & \varepsilon_{22,n_{F_{long}}} & \gamma_{12,n_{F_{long}}} \end{bmatrix} = \begin{bmatrix} ID_1 & \boldsymbol{\epsilon_{1_{F_{long}}}} \\ ID_2 & \boldsymbol{\epsilon_{2_{F_{long}}}} \\ \vdots & \vdots \\ ID_n & \boldsymbol{\epsilon_{n_{F_{long}}}} \end{bmatrix} \tag{6.15}$$

$$\boldsymbol{\epsilon_{F_{lat}}} = \begin{bmatrix} ID_1 & \varepsilon_{11,1_{F_{lat}}} & \varepsilon_{22,1_{F_{lat}}} & \gamma_{12,1_{F_{lat}}} \\ ID_2 & \varepsilon_{11,2_{F_{lat}}} & \varepsilon_{22,2_{F_{lat}}} & \gamma_{12,2_{F_{lat}}} \\ \vdots & \vdots & \vdots & \vdots \\ ID_n & \varepsilon_{11,n_{F_{lat}}} & \varepsilon_{22,n_{F_{lat}}} & \gamma_{12,n_{F_{lat}}} \end{bmatrix} = \begin{bmatrix} ID_1 & \boldsymbol{\epsilon_{1_{F_{lat}}}} \\ ID_2 & \boldsymbol{\epsilon_{2_{F_{lat}}}} \\ \vdots & \vdots \\ ID_n & \boldsymbol{\epsilon_{n_{F_{lat}}}} \end{bmatrix} \tag{6.16}$$

where n is the number of the elements included in the subset used for the optimization. Since the optical fiber is embedded between the first and the second ply, the deformations

are extracted from the top integration point of the first ply. The deformations of each element are normalized with respect to the corresponding load applied to the FE model:

$$\tilde{\boldsymbol{\epsilon}}_{\boldsymbol{i}_{\boldsymbol{F_{long}}}} = \frac{\boldsymbol{\epsilon}_{\boldsymbol{i}_{\boldsymbol{F_{long}}}}}{F_{long}} \tag{6.17}$$

$$\tilde{\boldsymbol{\epsilon}}_{\boldsymbol{i}_{\boldsymbol{F_{lat}}}} = \frac{\boldsymbol{\epsilon}_{\boldsymbol{i}_{\boldsymbol{F_{lat}}}}}{F_{lat}} \tag{6.18}$$

The deformations are expressed in the local reference frame of each element, hence they must be rotated in order to express them in the direction in which the FBG sensors measure, which is the other unknown of the optimization problem. The rotated deformation components for the $i-th$ element are obtained as:

$$\hat{\boldsymbol{\epsilon}}_{\boldsymbol{i}_{\boldsymbol{F_{long}}}} = \boldsymbol{R}\boldsymbol{T}_{\boldsymbol{i}}^{\boldsymbol{-1}}\boldsymbol{R}^{\boldsymbol{-1}}\tilde{\boldsymbol{\epsilon}}_{\boldsymbol{i}_{\boldsymbol{F_{long}}}} \tag{6.19}$$

$$\hat{\boldsymbol{\epsilon}}_{\boldsymbol{i}_{\boldsymbol{F_{lat}}}} = \boldsymbol{R}\boldsymbol{T}_{\boldsymbol{i}}^{\boldsymbol{-1}}\boldsymbol{R}^{\boldsymbol{-1}}\tilde{\boldsymbol{\epsilon}}_{\boldsymbol{i}_{\boldsymbol{F_{lat}}}} \tag{6.20}$$

where:

- $\mathbf{R} = \begin{bmatrix} 1 & 0 & 0 \\ 0 & 1 & 0 \\ 0 & 0 & 2 \end{bmatrix}$;
- $\mathbf{T_i} = \begin{bmatrix} \cos^2\theta_i & \sin^2\theta_i & 2\cos\theta_i\sin\theta_i \\ \sin^2\theta_i & \cos^2\theta_i & -2\cos\theta_i\sin\theta_i \\ -\cos\theta_i\sin\theta_i & \cos\theta_i\sin\theta_i & \cos^2\theta_i - \sin^2\theta_i \end{bmatrix}$, being θ_i the angle between the x-axis of the local reference system of the element and the axis aligned with the optical fiber. θ_i is one of the outputs of the optimization problem.

The FBG sensors measure the deformation component aligned with the optical fiber axis, which in this work is considered as the $\hat{x}$-axis, so the optimization process has to be performed using the $\hat{x}$-component of $\hat{\boldsymbol{\epsilon}}_{\boldsymbol{i}_{\boldsymbol{F_{long}}}}$ and $\hat{\boldsymbol{\epsilon}}_{\boldsymbol{i}_{\boldsymbol{F_{lat}}}}$, indicated respectively with $\hat{\epsilon}_{i_{F_{long},\hat{x}}}$ and $\hat{\epsilon}_{i_{F_{lat},\hat{x}}}$. At this point the matrix $\mathbf{K}$ of the linear system of Equation 6.24 is assembled as:

$$\boldsymbol{K} = \left[\boldsymbol{K}_{\boldsymbol{F_{long}}} | \boldsymbol{K}_{\boldsymbol{F_{lat}}}\right] \tag{6.21}$$

where:

- $\mathbf{K_{F_{long}}} = \begin{Bmatrix} \hat{\epsilon}_{1_{F_{long,\hat{x}}}} \\ \hat{\epsilon}_{2_{F_{long,\hat{x}}}} \\ \vdots \\ \hat{\epsilon}_{n_{F_{long,\hat{x}}}} \end{Bmatrix}$;
- $\mathbf{K_{F_{lat}}} = \begin{Bmatrix} \hat{\epsilon}_{1_{F_{lat,\hat{x}}}} \\ \hat{\epsilon}_{2_{F_{lat,\hat{x}}}} \\ \vdots \\ \hat{\epsilon}_{n_{F_{lat,\hat{x}}}} \end{Bmatrix}$;

The problem objective is:

$$\begin{aligned} &min[cond(\boldsymbol{K})] \\ &find(ID_i, \theta_i) \end{aligned} \tag{6.22}$$

The choice to use a genetic algorithm to perform the minimization process lies in its capability to take as input both discrete and continuous variables, as in the case of interest. As a matter of fact, the problem variables are the elements ID, that are discrete variables, and the sensors orientations, that in general are continuous variables. An overview of a genetic algorithm working principle is reported in the Appendix. The results of the optimization process are the following:

- the mean value and the minimum value of ($cond(\boldsymbol{K})$) for each generation, reported in Figure 6.22.

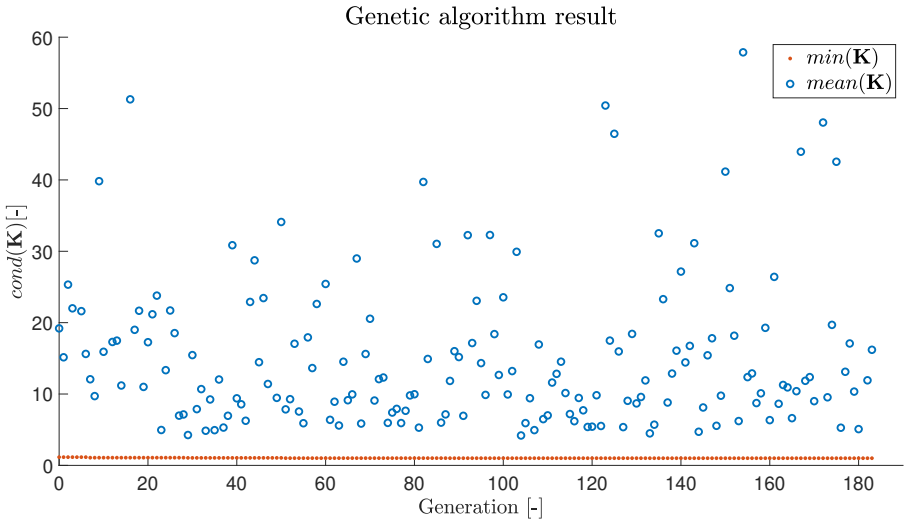

Figure 6.22: Genetic algorithm plot result

Considering all the generations, the best result obtained is $cond(\boldsymbol{K}) = 1.00735$;

- the elements in which position the FBG sensors, that are shown in Figure 6.23;

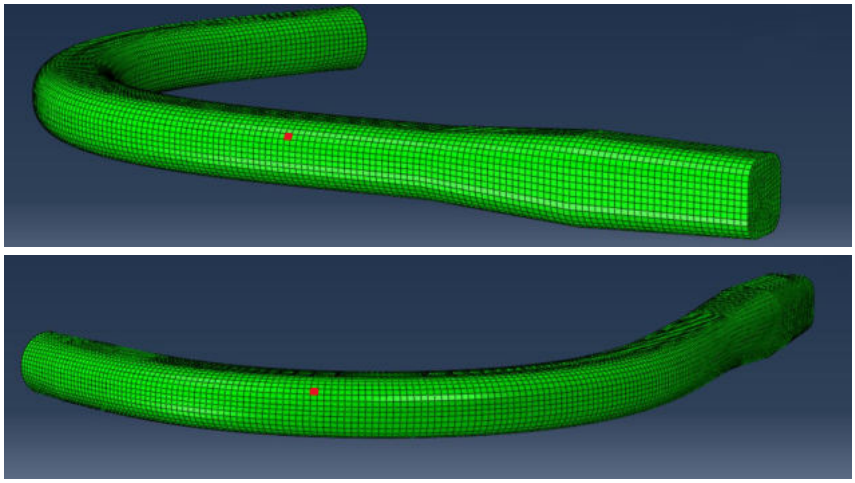

Figure 6.23: The two elements resulting from the optimization process in which position the FBG sensors

- the orientation of the FBG sensors, i.e., θ_1 and θ_2; from the technological point of view, it is not feasible to orient the sensors with an arbitrary value but usually the sensors are arranged parallel to the carbon fibers, perpendicular to them or with an angle of 45°. For this reason, the output angles have been discretized to the nearest angle of the following vector:

$$\boldsymbol{\theta} = \begin{Bmatrix} -45^\circ & 0^\circ & 45^\circ & 90^\circ \end{Bmatrix} \tag{6.23}$$

According to that, the resultant orientation of the FBG sensors is $\theta_1 = \theta_2 = 0°$, i.e., they are both aligned with the local $\hat{x}$-axis of the corresponding FE model element. From now on, the two sensors shown in Figure 6.23 will be refereed to as *FBG sensor 1* and *FBG sensor 2*.

6.7. Load identification using the FBG sensors

The procedure for the tests with the FBG sensors is the same of the one with the strain gauges described in Section 6.4, with the difference that the FBG sensors embedded in the stick are two, while the strain gauges previously used were four. Making the hypothesis of linearity, the relationship between the FBG sensor output and the applied loads can be expressed as:

$$\boldsymbol{\epsilon} = \mathbf{KP} \tag{6.24}$$

where:

- $\boldsymbol{\epsilon} = \begin{Bmatrix} \varepsilon_1 \\ \varepsilon_2 \end{Bmatrix}$ is the vector containing the two FBG sensors outputs for the considered loading condition;
- $\mathbf{K} = \begin{bmatrix} \alpha_{11} & \alpha_{12} \\ \alpha_{21} & \alpha_{22} \end{bmatrix}$ is the matrix of the *influence coefficients*;
- $\mathbf{P} = \begin{Bmatrix} F_{lat} \\ F_{long} \end{Bmatrix}$ is the matrix containing the applied loads.

While some strain gauges reading is relevant for just one loading condition between the pure longitudinal force and the pure lateral force (e.g., strain gauge 1 output is not relevant for the lateral force loading condition), the FBG sensors reading is relevant for both the loading conditions. The resultant linearity check plots for the two FBG sensors are reported in Figure 6.24. The linearity reference is obtained starting from the first point of each plot.

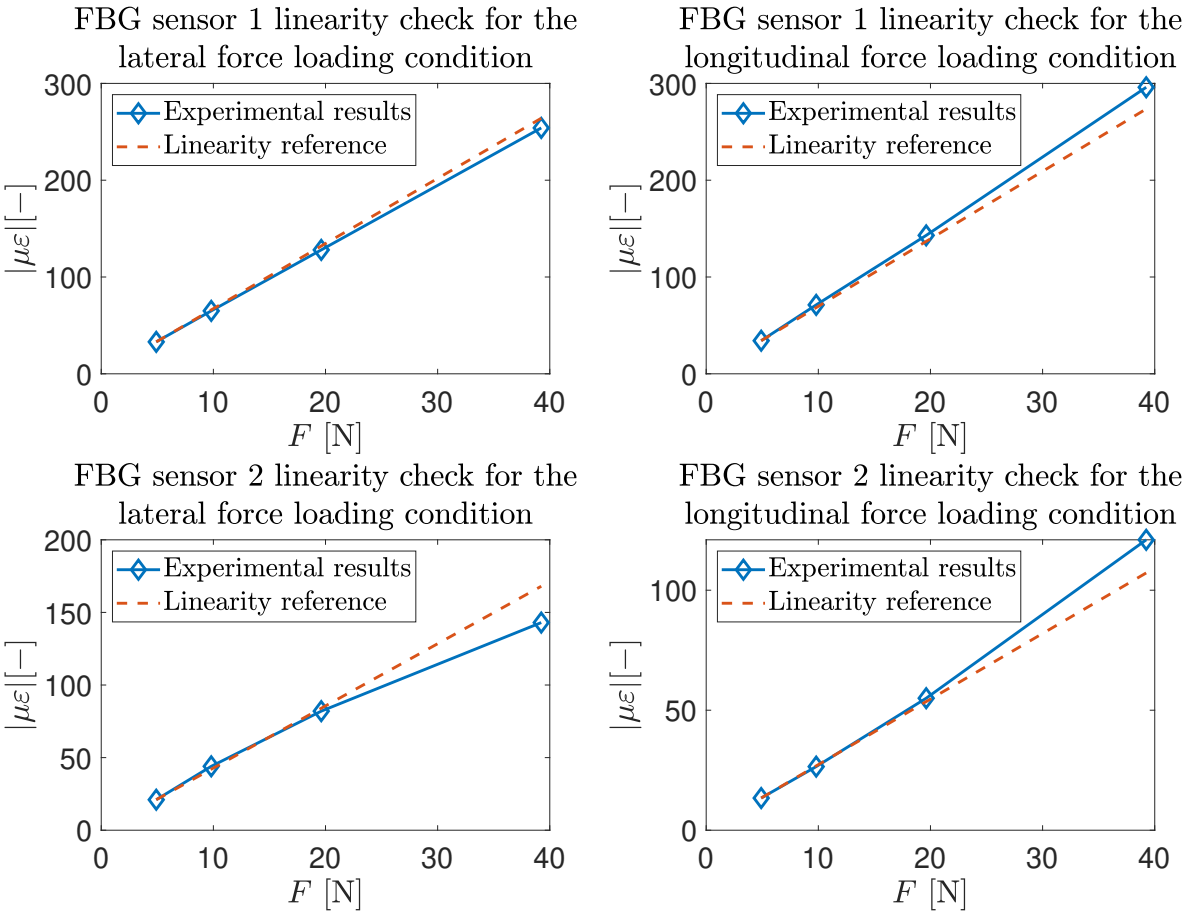

Figure 6.24: FBG sensors linearity check

The slopes of the plots of Figure 6.24 represents the influence coefficients:

$$\mathbf{K} = \begin{bmatrix} \alpha_{11} & \alpha_{12} \\ \alpha_{21} & \alpha_{22} \end{bmatrix} = \begin{bmatrix} -6.5877 & -7.2655 \\ 4.1476 & -2.8300 \end{bmatrix} [\mu\varepsilon/N] \tag{6.25}$$

A validation procedure for the FBG sensors is carried out analogously to the one of the strain gauges. The validation procedure is performed using masses of 0.5 kg, 1 kg, 2 kg, 4 kg and the results are reported in Table 6.5, Table 6.6, Table 6.7 and Table 6.8.

θ	$\mathbf{e}_{\mathbf{F}_{\mathbf{long}}}$ [%]	$\mathbf{e}_{\mathbf{F}_{\mathbf{lat}}}$ [%]
30°	0.08	16.87
45°	7.18	0.05
60°	4.16	8.02

Table 6.5: Validation process results using a mass of 0.5 kg

θ	$\mathbf{e}_{\mathbf{F}_{\mathbf{long}}}$ [%]	$\mathbf{e}_{\mathbf{F}_{\mathbf{lat}}}$ [%]
30°	0.06	13.48
45°	6.06	2.98
60°	0.20	8.44

Table 6.6: Validation process results using a mass of 1 kg

θ	$\mathbf{e}_{\mathbf{F}_{\mathbf{long}}}$ [%]	$\mathbf{e}_{\mathbf{F}_{\mathbf{lat}}}$ [%]
30°	1.41	5.46
45°	3.54	2.74
60°	2.24	0.02

Table 6.7: Validation process results using a mass of 2 kg

θ	$\mathbf{e_{F_{long}}}$ [%]	$\mathbf{e_{F_{lat}}}$ [%]
30°	3.74	1.90
45°	4.61	5.81
60°	2.91	5.00

Table 6.8: Validation process results using a mass of 4 kg

The results can be considered acceptable, since all the errors are below 6% except for two cases.

6.8. Comparison between the FBG readings and the FE model results

A comparison between the FBG sensors reading and the corresponding FE element deformation is carried out for each case and the results are reported in Table 6.9, Table 6.10, Table 6.11 and Table 6.12.

FBG sensor 1, F_{long} [%]	−3.5
FBG sensor 1, F_{lat} [%]	−6.06
FBG sensor 2, F_{long} [%]	−2.98
FBG sensor 2, F_{lat} [%]	37.61

Table 6.9: Strain components error between FE model and the FBG sensors for the test with a mass of 0.5 kg

FBG sensor 1, F_{long} [%]	0.56
FBG sensor 1, F_{lat} [%]	−7.69
FBG sensor 2, F_{long} [%]	−4.15
FBG sensor 2, F_{lat} [%]	40.45

Table 6.10: Strain components error between FE model and the FBG sensors for the test with a mass of 1 kg

FBG sensor 1, F_{long} [%]	0.97
FBG sensor 1, F_{lat} [%]	−9.37
FBG sensor 2, F_{long} [%]	−0.36
FBG sensor 2, F_{lat} [%]	36.09

Table 6.11: Strain components error between FE model and the FBG sensors for the test with a mass of 2 kg

FBG sensor 1, F_{long} [%]	4.32
FBG sensor 1, F_{lat} [%]	−10.23
FBG sensor 2, F_{long} [%]	8.76
FBG sensor 2, F_{lat} [%]	26.71

Table 6.12: Strain components error between FE model and the FBG sensors for the test with a mass of 4 kg

The error of the FBG sensor 2 for the pure lateral force loading condition is large for all the tests and this is probably due to some mandrel defects present in that region. Apart from that, it is possible to see that there is a good correlation between experimental and numerical results

In particular, the errors are smaller with respect to the ones obtained with the strain gauges (see Table 6.4), meaning that the FBG sensors positioning optimization procedure result is successful.

6.9. Consideration on the K matrix conditioning number

A final check can be made on the conditioning number of the matrix **K**, for which it is possible to consider the result from the experimental tests with the strain gauges, the numerical result of the optimization process and the experimental result from the tests with the FBG sensors, as reported in Table 6.13.

$cond(K_{strain\ gauges})$	5.18579
$cond(K_{FBG\ sensors,\ numerical})$	1.00735
$cond(K_{FBG\ sensors,\ experimental})$	1.98500

Table 6.13: Comparison table for the conditioning number of **K**

The experimental conditioning number of the tests with the FBG sensors does not differ to much with respect to the numerical result. Moreover, it is possible to see that the genetic algorithm optimization process has reduced the experimental conditioning number of matrix **K** by a factor of about 1/3, that can be considered a very good result.

7 | Conclusions and future developments

This thesis work presented two sensors to be embedded in the helicopter control inceptors for the pilot workload evaluation. The sensor included in the collective inceptor grip, re-engineered with respect to previous developments, allowed to monitor the pressure applied by the pilot hand on the grip itself. The pressure applied can be considered directly related to the pilot workload level, as demonstrated by the tests conducted at the motion platform. Indeed, the average grip pressure exerted by the tested subject increases as the MTE difficulty increases. The increase of the difficulty level has been implemented either in terms of the motion platform amplitude than in terms of piloting task difficulty. The peculiarity of the sensor proposed is the fact that, as opposed to the currently used subjective pilot workload assessment methods, it allows to have a measure independent from the pilot subjective feedback. Even though more tests on more subjects should be performed to draw solid conclusions, the trend of the average grip pressure for each test is well correlated to the one of other consolidated workload indicators, as the aggression and the moving median absolute deviation. A comparison between the grip sensor and the NASA-TLX ratings shows a good correlation as well, confirming the validity of the sensor as indicator of the pilot workload level. A relevant result from the tests performed with the motion platform is the finding that a relaxation of the arm muscles can help to counteract the vibrations induced by the vehicle to the pilot, that in turn translated in a better target tracking performance. This could be a useful results also in terms of PAO event, for which currently pilots are instructed to leave the controls. Also, the integration of the hand pressure measurements with the ones of a dedicated pressure able to detect the arm tension level could help in the study of the pilot behavior.

The developed and realized OPT-IN prototype presented the issue of having a low sensitivity. To improve the future developments of the sensor, it is possible to use a softer material for the hemispherical probes, which could make the sensor able to detect lower pressure variations. Moreover, the sensing elements of the grip could be extended to the whole grip itself, in order to make any pressure variation in any part of the grip detectable

by the sensor. Another improvement could be on the OPT-IN data acquisition: a proper wiring could make it possible to acquire its measurements with the Supervisory Control and Data Acquisition (SCADA) connected to the motion platform.

The novel cyclic inceptor stick realization technique has revealed to be successful, except for the mandrel dissolution process. A solution to this problem could consist in the use of a highly concentrated solution of sodium hydroxide. Despite that, the use of the mandrel allowed to have a good control thickness, that is crucial for the sensorization of the stick itself: the positioning of the strain gauges and of the FBG sensors has to be performed in regions of the stick in which the thickness is equal to the nominal one. Moreover, the thickness control ease to create a higher-fidelity FE model of the stick. The results obtained for the tests with the FBG sensors allowed to successfully accomplish the calibration process of the stick. The results of the optimization of the FBG sensors position carried out using the genetic algorithm has revealed to be fully satisfactory. Thanks to the genetic algorithm, the measure of two FBG sensors is well better than the one obtained with four strain gauges, for which a qualitative positioning based on the FE model results has been performed. As a matter of fact, both the validation results and the ones coming from the comparison between numerical and experimental model are definitely better for the FBG sensors with respect to the strain gauges.
As the collective grip sensor, the sensorized cyclic stick can be considered a tool for the pilot workload evaluation. As a matter of fact, it will be employed in the motion platform to monitor the loads introduced by the pilot, which have paramount importance in the prevention and study of RPC phenomena. Moreover, the sensors embedded in the stick allows to measure the force applied by the pilot without the use of costly, heavy and cumbersome load cells, which are not usually present in production helicopters. The force measurement allows to compute one of the two fundamental indices of the pilot-vehicle interaction, that is the BDFT. In particular, the stick sensors allow to compute the BDFT using the pilot force as output instead of the inceptor rotation. This particularly useful in case of a high level of friction present in the controls: in this case, the motion of the inceptor is small, while the force applied by the pilot is not, especially in high load factor flight conditions. It is worth mentioning that the cyclic inceptor stick realized in this work represents an experimental laboratory product, currently non-serviceable on a real flight. As a matter of fact, the focus has been placed on the stick realization and sensorization, without addressing problems as, just to mention few of them, the stick-cockpit connection elements, the setup for the in-flight FBG data acquisition system and the interface with the existing wiring. In addition, the certification process needed to make the stick flyable requires additional steps to ensure its airworthiness, such as:

- compliance with Design Standards: each structural component of an aircraft must meet the applicable design standards and regulations. This typically includes demonstrating compliance with specific load factors, fatigue life requirements, material specifications, and structural integrity criteria;
- structural analysis and testing: the component must undergo rigorous structural analysis and testing to ensure its strength, durability, and performance under anticipated loads and operational conditions;
- manufacturing process documentation, control and certification. This includes ensuring compliance with relevant quality management systems, such as ISO 9001, and maintaining appropriate records of the manufacturing and inspection procedures.

The pressure sensor of the grip, instead, is closer to become flyable. To implement its actual configuration on an existing grip, it would be necessary to have the needed space inside the grip and to cut some parts of the grip itself for the placement of the sliding parts of the sensor containing the photoresistor and the hemispherical probes. A potential improvement could be to make the sensor thinner, for example in the form of pressure sensitive films applicable on the grip external surface. This would not require any major modification to the grip geometry.

Bibliography

[1] EASA. Annual safety review, 2022.

[2] M. D. Pavel, M. Jump, B. Dang-Vu, P. Masarati, M. Gennaretti, A. Ionita, L. Zaichik, H. Smaili, G. Quaranta, D. Yilmaz, M. Jones, J. Serafini, and J. Malecki. Adverse rotorcraft pilot couplings—past, present and future challenges. *Progress in Aerospace Sciences*, pages 62–113, 2013. ISSN 0376-0421. doi: https://doi.org/10.1016/j.paerosci.2013.04.003. URL `https://www.sciencedirect.com/science/article/pii/S0376042113000316`.

[3] O. Dieterich, J. Götz, B. Dangvu, H. Haverdings, P. Masarati, M. Pavel, M. Jump, and M. Gennaretti. Adverse rotorcraft-pilot coupling: Recent research activities in europe. *Royal Aeronautical Society*, 9 2008. URL `http://resolver.tudelft.nl/uuid:06900f96-8803-4d52-bb28-43b1211495b0`.

[4] P. Garbo, A. Zanoni, and G. Quaranta. Online evaluation of helicopter pilot workload during a flight simulator experiment. *AIAA Journal*, 2021. ISSN 1533-385X. doi: https://doi.org/10.2514/6.2022-0511. URL `https://arc.aiaa.org/doi/pdf/10.2514/6.2022-0511`.

[5] J. Venrooij, D. A. Abbink, M. Mulder, M. M. van Paassen, and M. Mulder. Biodynamic feedthrough is task dependent. *IEEE International Conference on Systems Man and Cybernetics (SMC), Istanbul, Turkey, pp. 2571-2578*, 2018. doi: 10.1109/ICSMC.2010.5641915.

[6] A. Zanoni, M. Zago, R. Paolini, G. Quaranta, M. Galli, and P. Masarati. On task dependence of helicopter pilot biodynamic feedthrough and neuromuscular admittance: An experimental and numerical study. *IEEE Transactions on Human-Machine Systems, pp. 1–11*, 2021. doi: https://doi.org/10.1109/THMS.2020.3044971.

[7] P. Garbo and A. Zanoni. Optical inceptor for helicopter flight control. *Switch2Product*, 2020.

[8] P. Masarati and A. Zanoni. Pilot-vehicle interaction from a multibody dynamics and

experimental perspective. *MAGIC*, 2022. URL https://re.public.polimi.it/retrieve/55a108d0-87d0-4d11-a803-76373972edda/MASAP02-22_part1.pdf.

[9] V. Muscarello, G. Quaranta, P. Masarati, L. Lu, M. Jones, and M. Jump. Prediction and simulator verification of roll/lateral adverse aeroservoelastic rotorcraft–pilot couplings. *Journal of Guidance, Control, and dynamics*, 39(1), 1 2016. doi: https://doi.org/10.2514/1.G001121.

[10] A. Zanoni, P. Garbo, A. Lavatelli, and G. Quaranta. Sensore di pressione ottico, 3 2023.

[11] Michael Wagner, Yotam Sahar, Tomer Elbaum, Assaf Botzer, and Eyal Berliner. Grip force as a measure of stress in aviation. *The International Journal of Aviation Psychology*, 25(3-4):157–170, 2015. doi: 10.1080/10508414.2015.1162632. URL https://doi.org/10.1080/10508414.2015.1162632.

[12] H. Roscoe. The practical assessment of pilot workload. *AGARD-AG-233, Chapter 1*, pages 3–10, 1978. URL https://www.sto.nato.int/publications/AGARD/AGARD-AG-233/AGARD-AG-233.pdf.

[13] G. E. Cooper and R. P. Harper. The use of pilot rating in the evaluation of aircraft handling qualities. *AGARD*, 1969. URL https://apps.dtic.mil/sti/pdfs/AD0689722.pdf.

[14] H. Roscoe. The practical assessment of pilot workload. *AGARD-AG-282, Chapter 1*, pages 1–10, 1987. URL https://www.sto.nato.int/publications/AGARD/AGARD-AG-282/AGARD-AG-282.pdf.

[15] A.G. Hart. Theoretical basis for workload assessment research at nasa ames research center. *Proceedings of the Workshop on Flight Testing to Identify Pilot Workload and Pilot Dynamics AFFTC-TR-82-5*, 1982.

[16] R. C. Van de GRAAFF. Nlr research on pilot dynamics and workload. *Proceedings of the workshop on Flight Testing to Identify Pilot Workload and Pilot Dynamics. AFFTC-TR-82-5*, 1982.

[17] A. Roscoe and G. Ellis. A subjective rating scale for assessing pilot workload in flight: A decade of practical use. *TR 90019,Royal Aerospace Establishment,*, 1990. URL https://apps.dtic.mil/sti/citations/ADA227864.

[18] J. Forrest, S. Hodge, I. Owen, and G. Padfield. Towards fully simulated ship-helicopter operating limits: The importance of ship airwake fidelity. *AHS 64th Annual Forum, Montréal, Canada*, 2008. URL https://www.researchgate.

net/publication/273765987_Towards_fully_simulated_ship-helicopter_operating_limits_The_importance_of_ship_airwake_fidelity.

[19] Human Performance Research Group. Nasa task load index (tlx). *NASA Ames Research Center*, 1980. URL https://ntrs.nasa.gov/api/citations/20000021488/downloads/20000021488.pdf.

[20] M. Jones, M. Jump, and L. Lu. Development of the phase-aggression criterion for rotorcraft—pilot coupling detection. *Journal of Guidance, Control, and dynamics*, 36(1):35–47, 1 2013. doi: https://doi.org/10.2514/1.58232.

[21] A. Zanoni, M. Zago, R. Paolini, G. Quaranta, P. Masarati, M. Galli, G. Maisano, L. Frigerio, and M. Murawa. Flight simulator testing to enhance comprehension and modeling of rotorcraft pilot couplings. *ERF, Philadelphia, PA, USA*, 2019. URL https://re.public.polimi.it/retrieve/e0c31c0e-7af8-4599-e053-1705fe0aef77/ZANOA02-19.pdf.

[22] B. Johannes, S. Rothe, A. Gens, S. Westphal, K. Birkenfeld, E. Mulder, J. Rittweger, and C. Ledderhos. Psychophysiological assessment in pilots performing challenging simulated and real flight maneuvers. *AMHP Journal*, pages 834–840, 9 2017. doi: 10.3357/AMHP.4782.2017.

[23] Yotam Sahar, Michael Wagner, Ariel Barel, and Shraga Shoval. Stress-adaptive training: An adaptive psychomotor training according to stress measured by grip force. *Sensors*, 22(21):8368, 2022. ISSN 1424-8220. doi: 10.3390/s22218368. URL http://dx.doi.org/10.3390/s22218368.

[24] S. Zhu, A. Yu, D. Hawley, and R. Roy. Frustrated total internal reflection: a demonstration and review. *American Journal of Physics, pp. 601-607*, 1986. doi: https://doi.org/10.1119/1.14514.

[25] A. Lavatelli, A. Zanoni, E. Zappa, and A. Cigada. On the design of force sensors based on frustrated total internal reflection. *IEEE Transactions on Instrumentation and Measurement, pp. 4065-4074*, 2018. doi: 10.1109/TIM.2018.2885604.

[26] P. Garbo, A. Zanoni, and G. Quaranta. An optical pressure measurement system for control inceptors to evaluate pilots' workload. *4th International Conference on Human Systems Engineering and Design: Future Trends and Applications (IHSED 2021)*, 2022. doi: http://doi.org/10.54941/ahfe1001155.

[27] Pierre Garbo. *Development of flight simulation hardware and methods to investigate RPC phenomena and workload estimation.* PhD thesis, Politecnico di Milano, 2023.

[28] A. Zanoni, D. Marchesoli, C. Talamo, P. Masarati, F. Colombo, S. Kemp, and E. Fosco. Experimental test-bed for the identification of biodynamic feedthrough of helicopter-pilot systems. *48th European Rotorcraft Forum (ERF)*, 2022. URL https://re.public.polimi.it/retrieve/aff0948e-6525-4915-98d4-4951d99f6b32/ZANOA08-22.pdf.

[29] C. S. Shin and C. Chiang. Deformation monitoring by using optical fiber grating sensor. *Journal of the Chinese Institute of Engineers, Vol. 28, No. 6, pp. 985-992*, 2005. doi: 10.1080/02533839.2005.9671073.

[30] D. Wrangborg A. Marchenko, B. Lishman and T. Thiel. Thermal expansion measurements in fresh and saline ice using fiber optic strain gauges and multipoint temperature sensors based on bragg gratings. *Journal of Sensors, Volume 2016, Article ID 5678193, 13 pages*, 2006. doi: https://doi.org/10.1155/2016/5678193.

[31] Francisco Javier Sanchez Olivera. Experimental and numerical analysis of hybrid cfrp/aluminum laminates response under high-velocity impacts, 2023.

[32] ASTM International. Standard test method for tensile properties of polymer matrix composite materials, 2007. URL http://file.yizimg.com/175706/2012061422194947.pdf.

[33] ASTM International. Standard test method for in-plane shear response of polymer matrix composite materials by tensile test of a $\pm 45^{\circ}$ laminate, 2007. URL https://oss.jishulink.com/upload/201912/c1045e8a7f5b4d5bba96e018c78c7705.pdf.

[34] Formlabs. Tough 2000 resin for rugged prototyping. URL https://formlabs-media.formlabs.com/datasheets/2001340-TDS-ENUS-0P.pdf.

[35] A. Airoldi, L. Marelli, P. Bettini, G. Sala, and A. Apicella. Strain field reconstruction on composite spars based on the identification of equivalent load conditions. *Sensors and Smart Structures Technologies for Civil, Mechanical, and Aerospace Systems (Vol. 10168, pp. 207-226). SPIE.*, 2017. doi: 10.1117/12.2260161.

[36] US Department of Defense. Polymer matrix composites: guidelines for characterization of structural materials. *Handbook, Military.*, 2018. URL http://l.academicdirect.org/Statistics/tests/kS-AD/MIL-HDBK-17-1F.pdf.

A | Appendix

Overview on the genetic algorithm

A genetic algorithm is a search and optimization technique inspired by the process of natural selection and genetics. It is used to solve minimization problems where traditional algorithms may be impractical or ineffective. The algorithm simulates the evolution of a population of potential solutions over multiple generations, gradually improving the quality of solutions until an acceptable or optimal solution is found. Here's an overview of the working principle of a genetic algorithm, summarized in the flow chart of Figure A.1:

1. *initialization*: the algorithm starts by creating a random population of individuals, where each individual represents a potential solution to the problem at hand. The population typically consists of a fixed number of individuals, each encoded as a string or vector called *chromosome*;

2. *evaluation*: each individual in the population is evaluated and assigned a fitness value based on how well it solves the problem. The *fitness function* determines the quality or suitability of an individual solution;

3. *selection*: individuals are selected from the population to serve as *parents* for the next generation. The selection process is typically based on the fitness values, where individuals with higher fitness have a higher probability of being selected. This process mimics the concept of "survival of the fittest";

4. *reproduction*: selected individuals are combined through genetic operators such as *crossover* and *mutation* to create offspring for the next generation. Crossover involves combining genetic material from two parents to produce new individuals, while mutation introduces random changes in the offspring's genetic information;

5. *replacement*: the offspring, along with some individuals from the current population, form the next generation. The replacement strategy determines which individuals from the current population are replaced by the offspring. This ensures that the population evolves over time and encourages exploration of the search space;

6. *termination*: the algorithm continues iterating through the evaluation, selection, reproduction, and replacement steps until a termination condition is met. This condition could be a maximum number of generations, reaching a satisfactory solution, or a predefined convergence criterion.

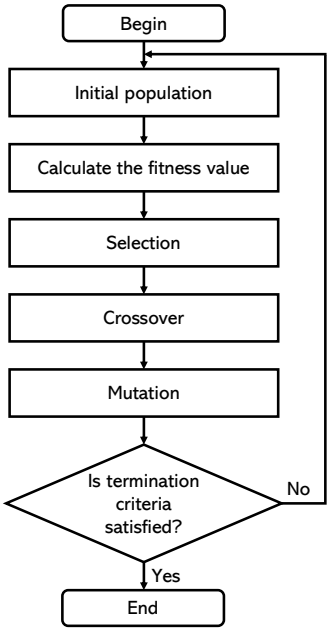

Figure A.1: Genetic algorithm flow chart

By iteratively applying the steps above, the genetic algorithm explores the solution space by evolving and refining the population over multiple generations. Over time, the algorithm tends to converge towards better solutions that satisfy the problem constraints and optimize the fitness function. It's worth noting that the effectiveness of a genetic algorithm depends on various factors such as the choice of genetic operators, population size, termination conditions, and the design of the fitness function. The genetic algorithm can be applied to solve a variety of optimization problems that are not well-suited for standard optimization algorithms. While the effectiveness of an algorithm depends on the problem domain and specific requirements, genetic algorithms offer several advantages compared to other algorithms in certain contexts, as:

1. global optimization: genetic algorithms are known for their ability to find solutions in large and complex search spaces. They are particularly well-suited for problems where the solution space is vast and there may be multiple global optima. Genetic algorithms explore the search space more extensively and have a higher chance of finding good solutions compared to local search algorithms;

2. no requirement of derivatives: genetic algorithms do not rely on gradient information or derivatives of the objective function, which makes them applicable to a wide range of problems, including those that are non-differentiable, discontinuous, or noisy. This is in contrast to techniques like gradient descent, which require derivatives and may struggle in such scenarios;

3. flexibility and adaptability: genetic algorithms can handle optimization problems that involve multiple objectives, constraints, or trade-offs. They can be easily modified to accommodate different problem formulations, fitness functions, and optimization goals. Genetic algorithms can also handle both discrete and continuous variables, allowing for a broader range of applications;

4. parallel processing: genetic algorithms can naturally take advantage of parallel processing and distributed computing environments. The population-based nature of genetic algorithms allows for concurrent evaluation and evolution of multiple candidate solutions, enabling faster convergence and improved scalability on modern computing architectures;

5. exploration and diversity: genetic algorithms emphasize exploration of the solution space by maintaining diversity within the population. By incorporating mechanisms such as crossover and mutation, genetic algorithms introduce new genetic material into the population, allowing for exploration of new regions of the search space. This exploration capability helps to prevent premature convergence to suboptimal solutions;

6. problem independence: genetic algorithms are problem-agnostic in the sense that they do not rely on specific domain knowledge or problem structure. They can be applied to a wide variety of optimization problems without requiring problem-specific modifications or heuristics. This makes genetic algorithms a versatile choice for optimization tasks across different domains;

7. solving complex, non-linear problems: genetic algorithms have been successfully applied to a wide range of complex problems, including function optimization, machine learning, scheduling, robotics, and more. Their ability to handle non-linear, multimodal, and dynamic problems makes them a valuable tool in many fields where traditional optimization methods may struggle.

List of Figures

List of Tables

List of Acronyms